Fig. 6.4 shows that the length of bainite sheaves is, as expected, also affected by the austenitisation temperature, becoming larger as the grain size increases.

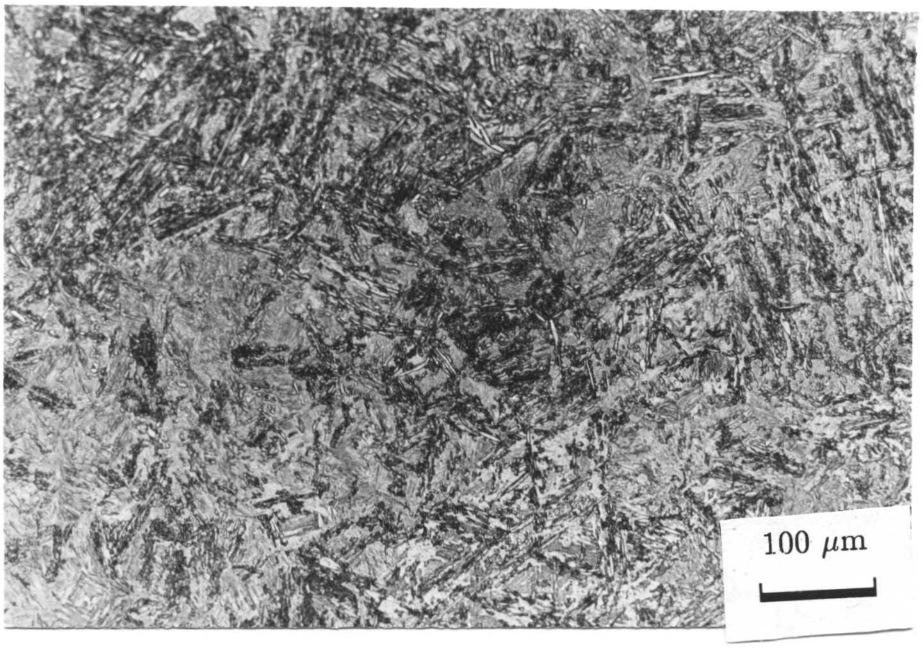

(a)

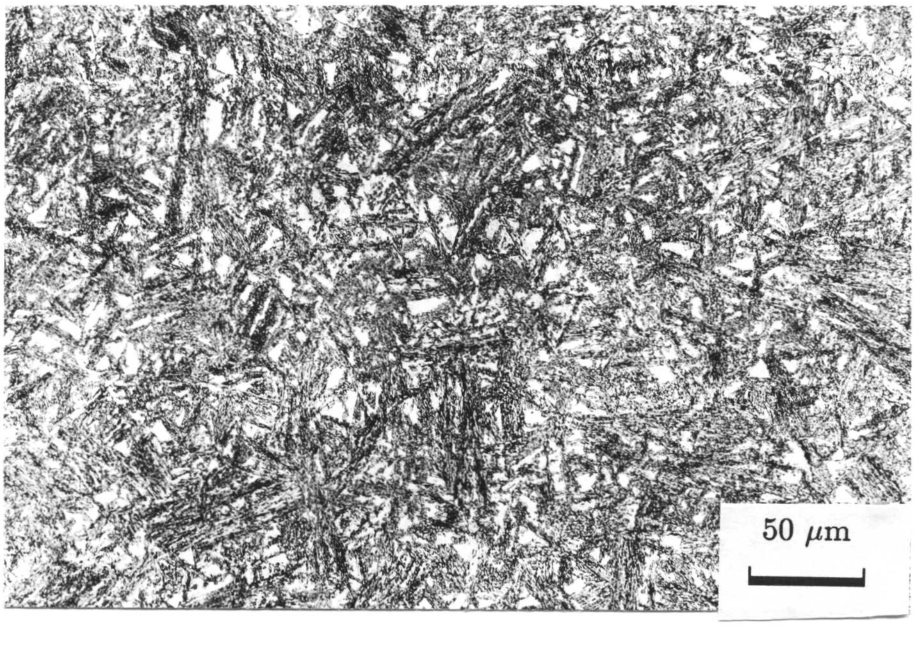

(b)

Fig. 6.4: *Continued.......*

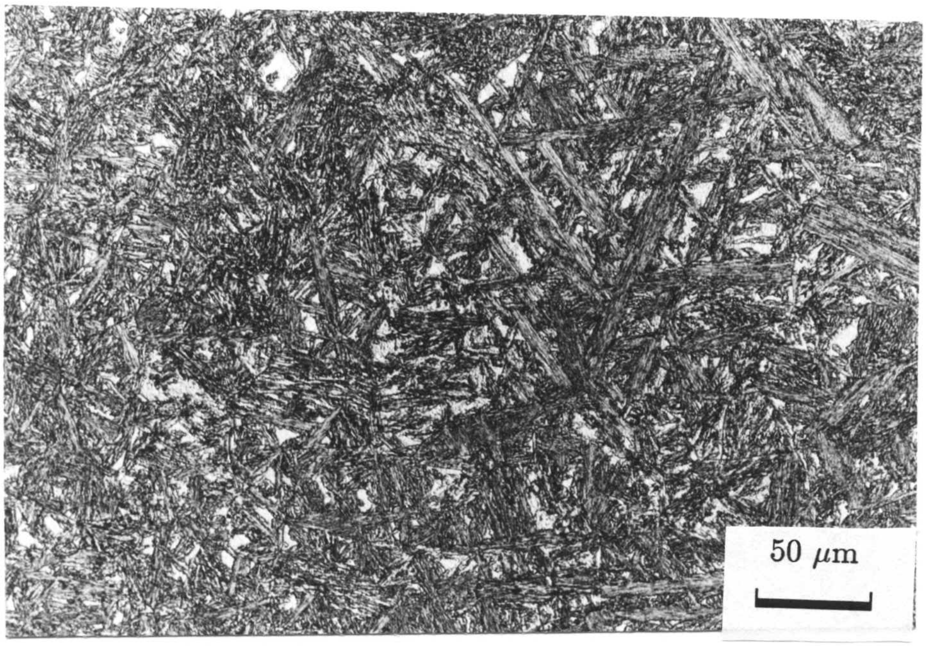

(c)

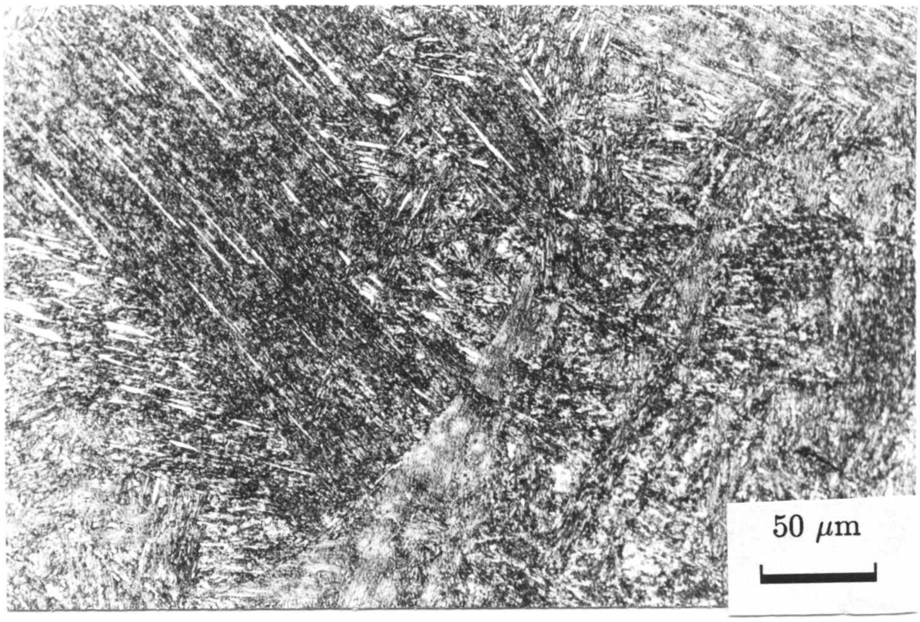

(d)

Fig. 6.4: *Optical micrographs showing the effect of austenitisation temperature on the microstructure obtained in the alloy A2, by isothermal transformation at 400 °C for 2000 °C after austenitisation for 5* min *at (a) 900 °C (b) 1000 °C (c) 1100 °C and (d) 1200 °C.*

In order to check whether there is any transformation during cooling from the austenitisation temperature to the isothermal transformation temperature, changes in length were plotted against temperature (Fig. 6.5). No deviation from linearity could be detected, indicating that there is no transformation during cooling to the bainite transformation temperature.

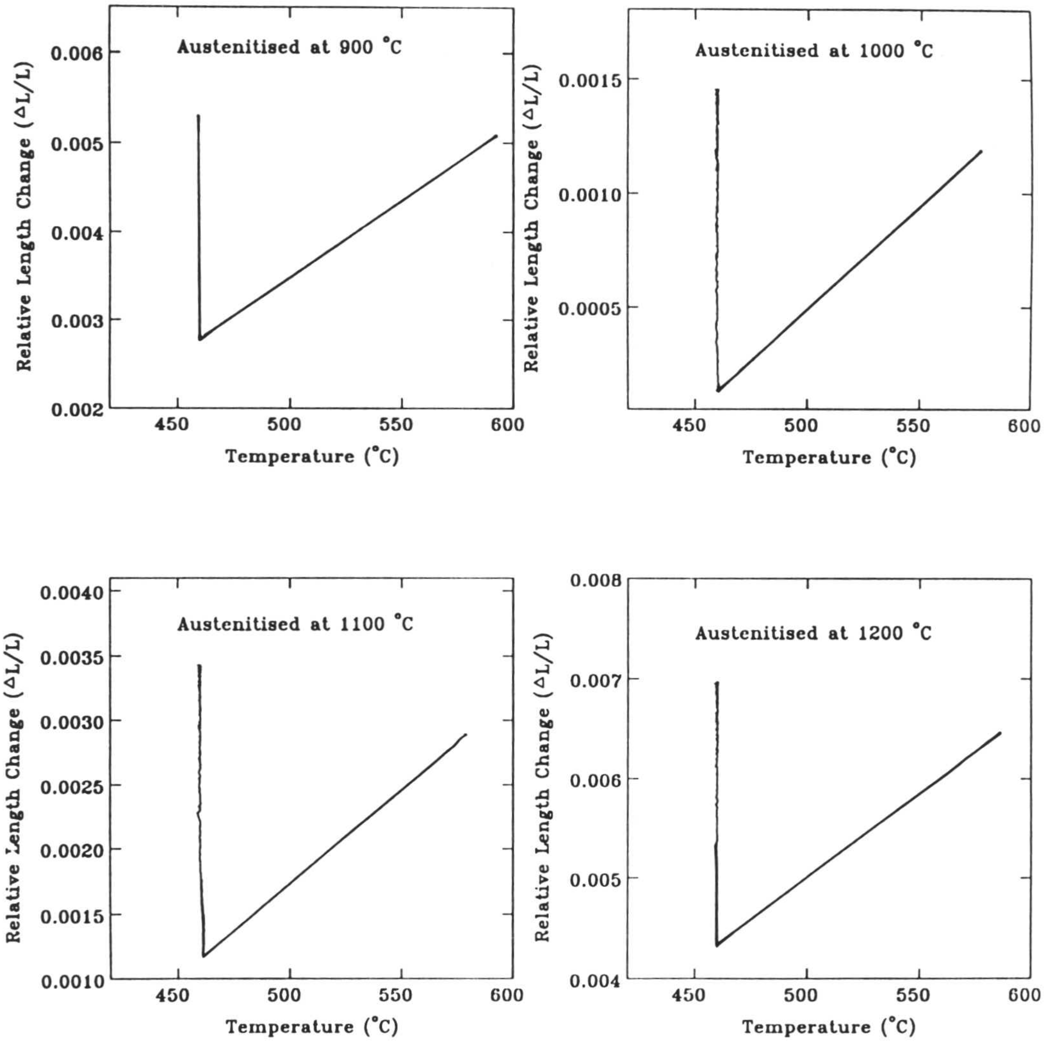

Fig. 6.5: *Relative length versus temperature dilatometric curves showing that there is no transformation during cooling prior to the isothermal bainite transformation in alloy A2.*

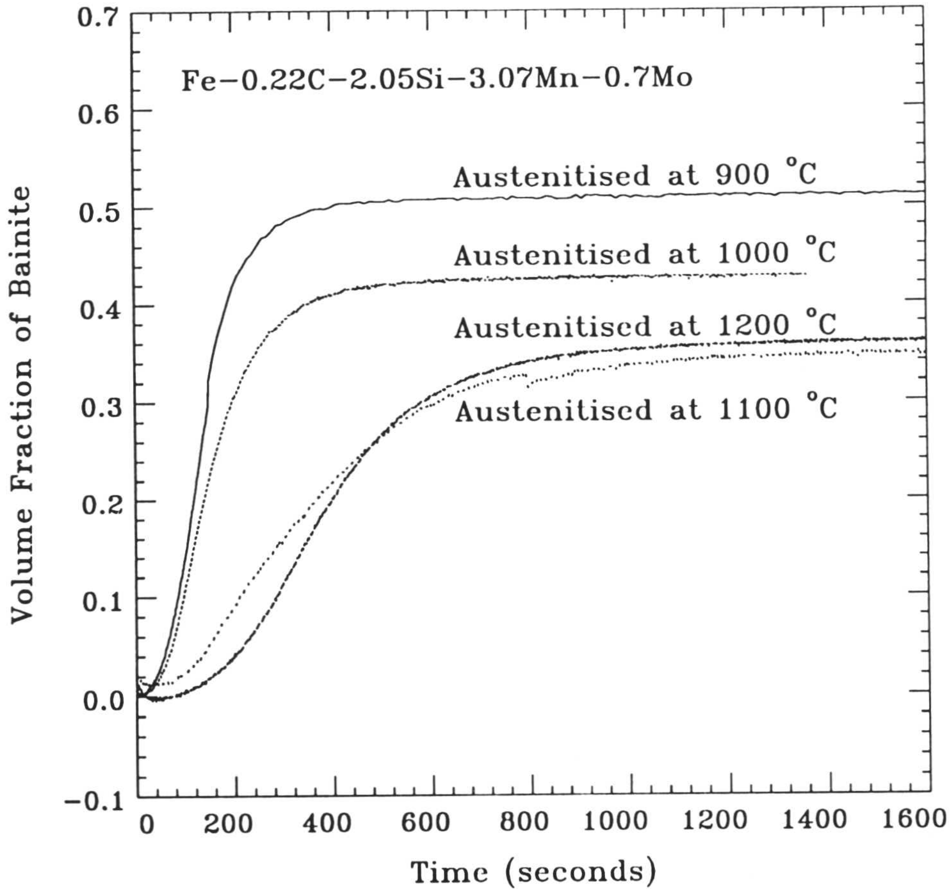

Fig. 6.6: *Effect of austenitisation temperature on the volume fraction of bainite in alloy A2. Note that only about 50 % austenite transformed to bainitic ferrite and other left as residual austenite even after longer time.*

Fig. 6.6 illustrates the data of Fig. 6.4, after converting the length changes into volume fractions using the methods discussed earlier. The times taken to achieve 5, 50 and 95 % (of the maximum extent at any temperature) of bainite transformation as a function of austenitisation temperature are tabulated in Table 6.2 and plotted in Fig. 6.7.

Table 6.2: *Effect of austenitisation temperature on time taken by a fixed amount of bainite transformation in alloy A2.*

Austenitisation Temperature °C	Time s		
	5 %	50 %	95 %
900	45	135	309
1000	50	146	378
1100	84	321	850
1200	149	374	822

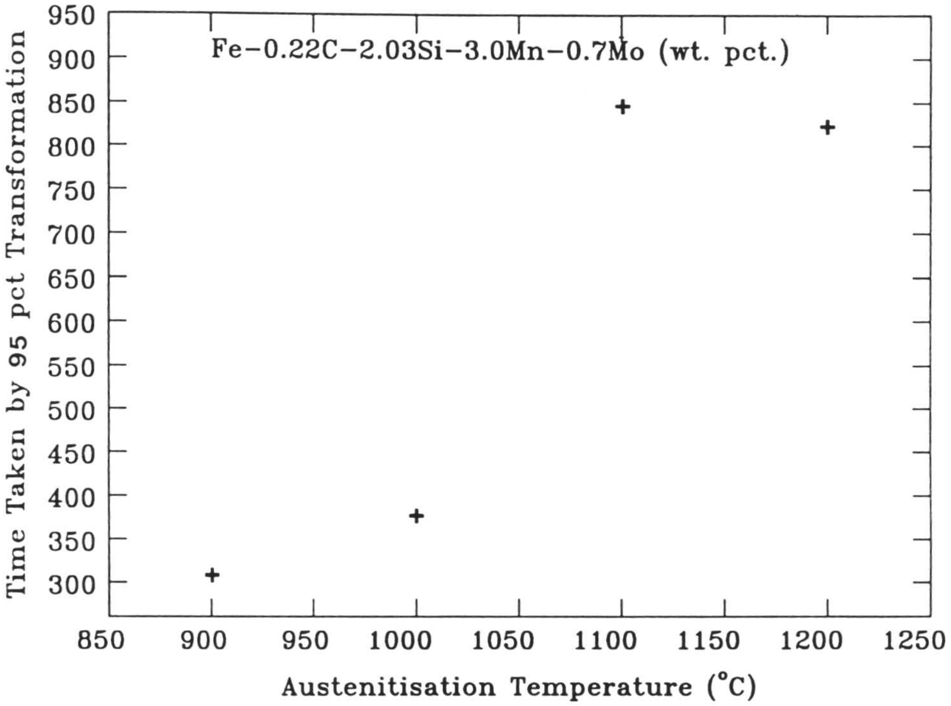

(a)

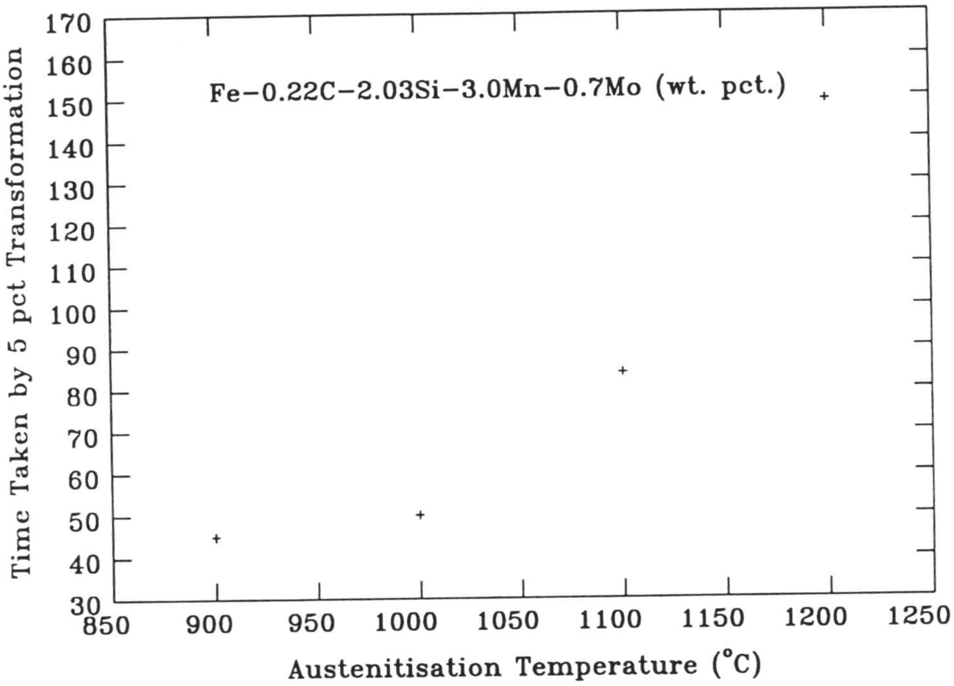

(b)

Fig. 6.7: *The effect of austenitisation temperature on the time taken for (a) 5 %, (b) 95 % transformation.*

6.3.2 *Transformation in Alloy A102*

The formation of bainite is relatively faster in this alloy because of its lower carbon content. The effect of austenitisation temperature on the kinetics of bainite reaction is shown in Fig. 6.8. Again as the austenitisation temperature increased, the kinetics of the reaction become slower.

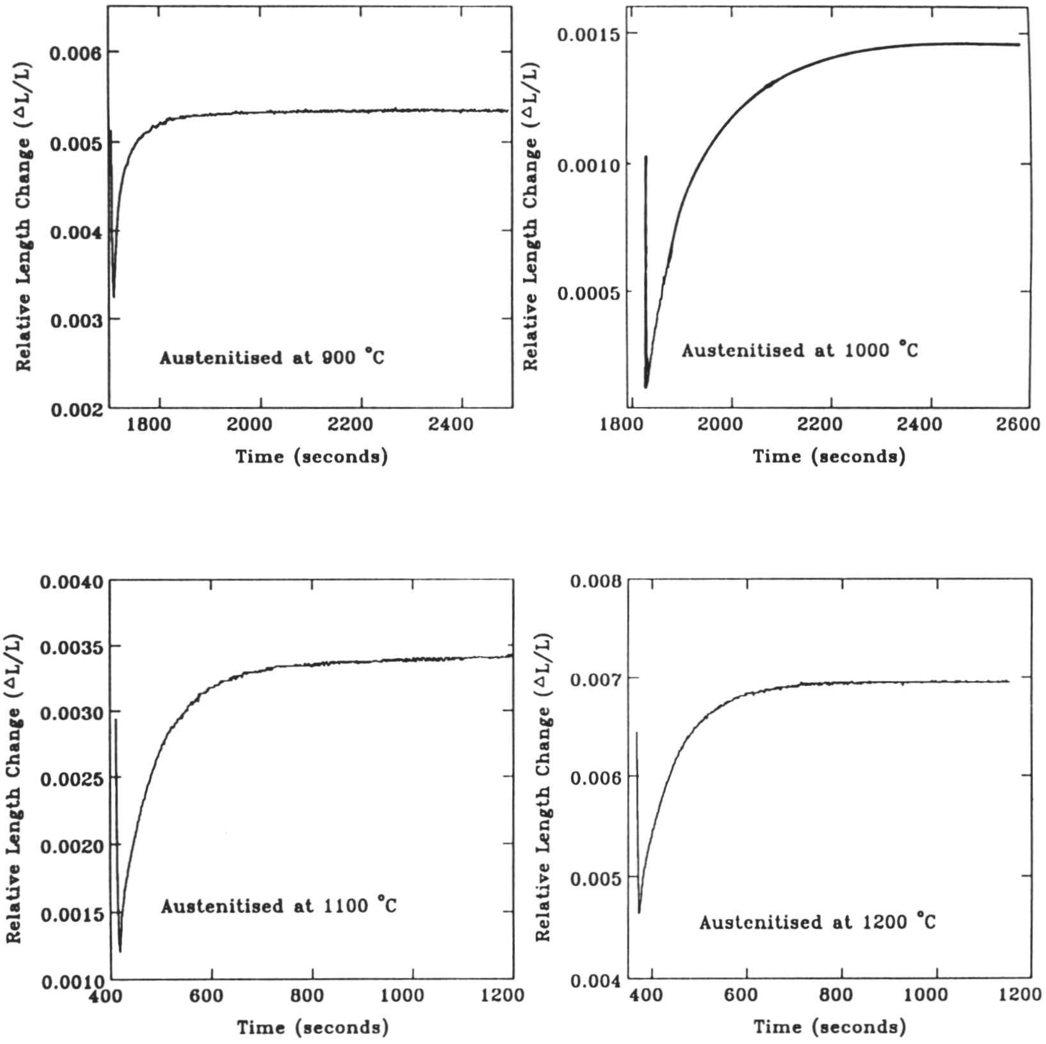

Fig. 6.8: *Dilatometric curves showing the effect of austenitisation temperature on the kinetics of bainite reaction in alloy A102.*

Due to faster bainite reaction kinetics in this alloy, it was necessary to check any transformation happening during cooling. The results shown in Fig. 6.9 and reveal that there is no transformation during cooling except bainite.

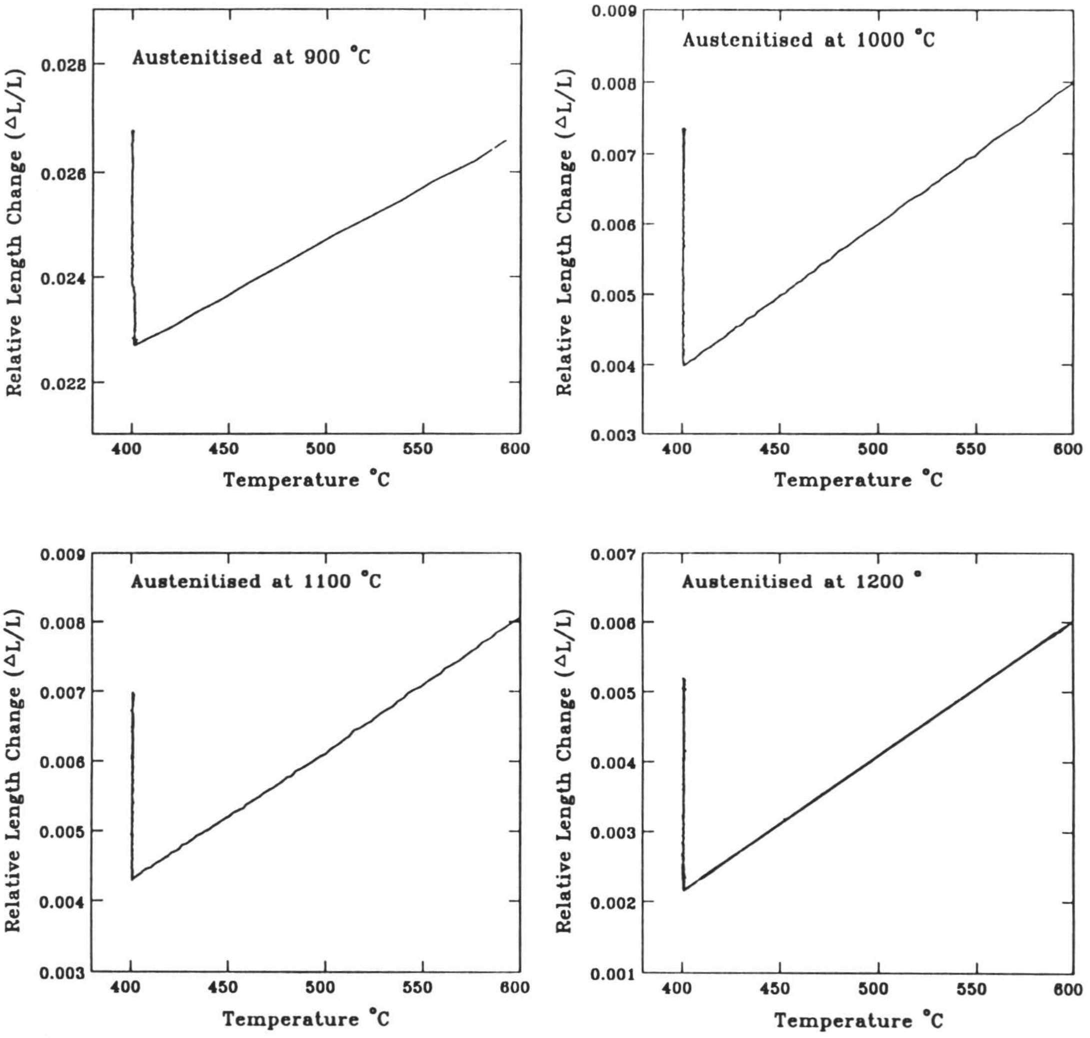

Fig. 6.9: *Relative length versus temperature dilatometric curves showing that there is no transformation during cooling prior to the isothermal bainite transformation in alloy A102.*

The micrographs in Fig. 6.10 show the effect of austenitisation temperature on bainite transformation in alloy A102. Fig. 6.10 again shows, as expected, that the longer sheaves are associated with the higher austenitisation temperatures.

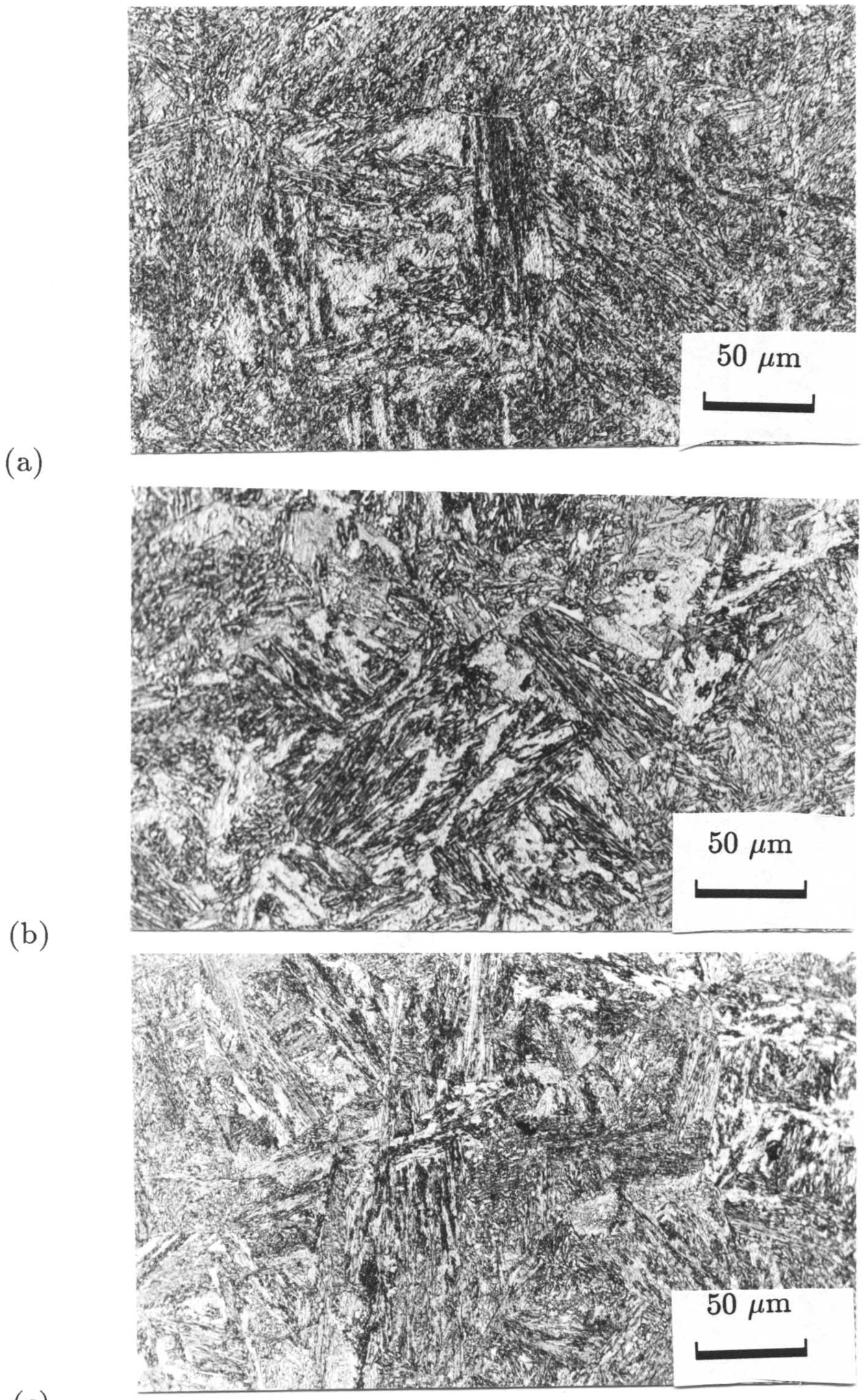

Fig. 6.10: *Optical micrographs showing the effect of austenitisation temperature on bainite microstructure in alloy A102. All specimens isothermally transformed at 480 °C for 1000* s *after austenitisation of 5* min *at (a) 900 °C and (b) 1000 °C and (c) 1200 °C.*

The amount of bainite formed after austenitisation at different austenitisation temperatures is shown in Fig. 6.11. It is depicted from Fig. 6.11 that the amount of bainite formation also affected, and higher austenitisation temperature leads to the lesser amount of bainite transformation.

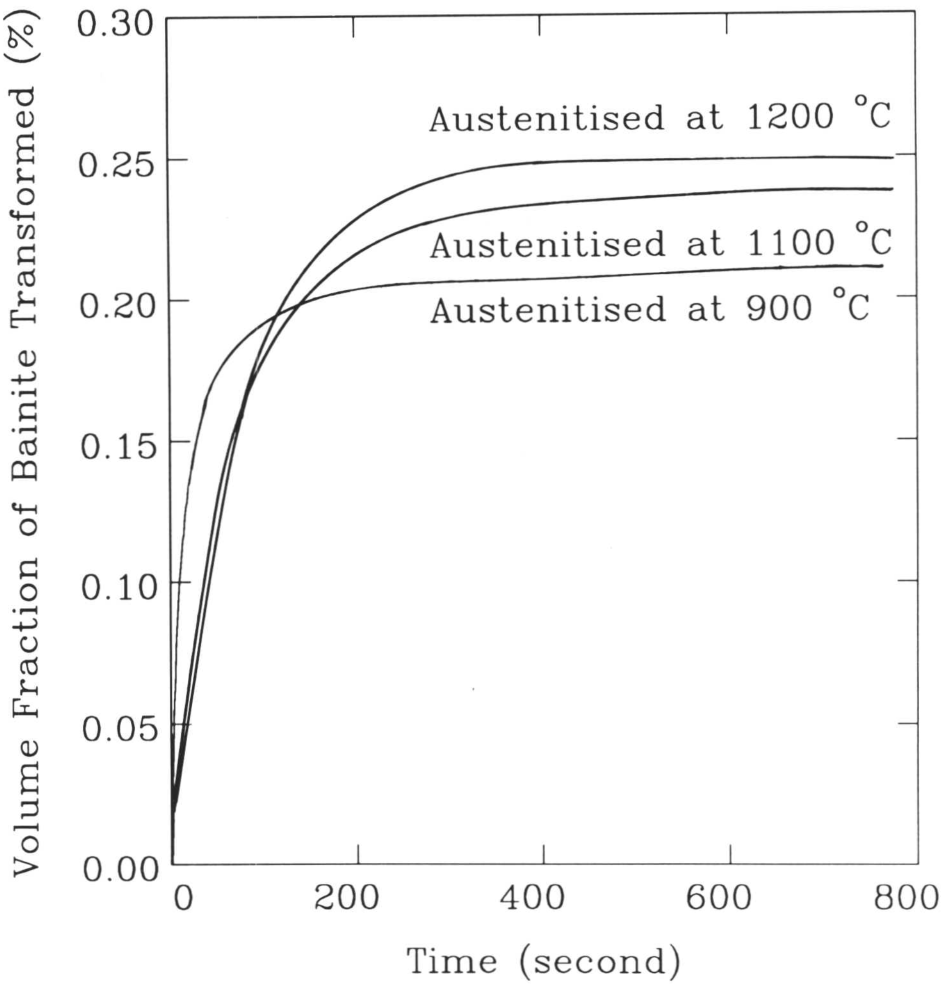

Fig. 6.11: *Effect of austenitisation temperature on the volume fraction of bainite obtained in alloy A102. Note that only about 50 % of austenite at most transformed to bainite before the reaction ceased.*

The time taken to achieve a fixed amount of bainite transformation was also measured after converting of relative length data to the volume fraction of bainite. The results are given in Table 6.3. Fig. 6.12 show that time taken by 5 and 95 % transformation increases with increasing austenitisation temperature.

Table 6.3: *Effect of austenitisation temperature on time taken achieve a fixed amount of bainite transformation in alloy A102.*

Austenitisation Temperature °C	Time s	
	5 %	95 %
900	1	60
1000	4	270
1100	6	300
1200	6.5	320

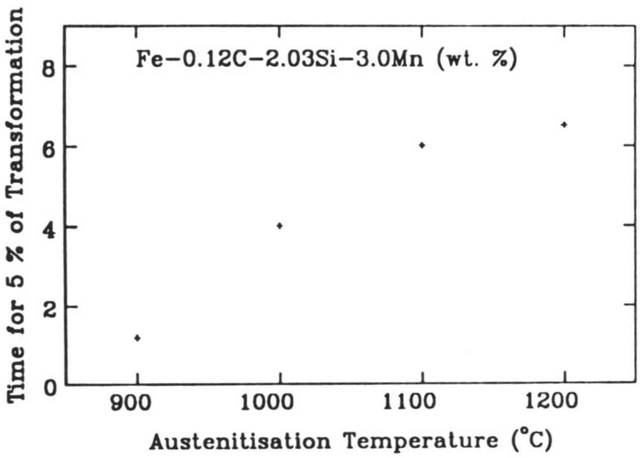

(a)

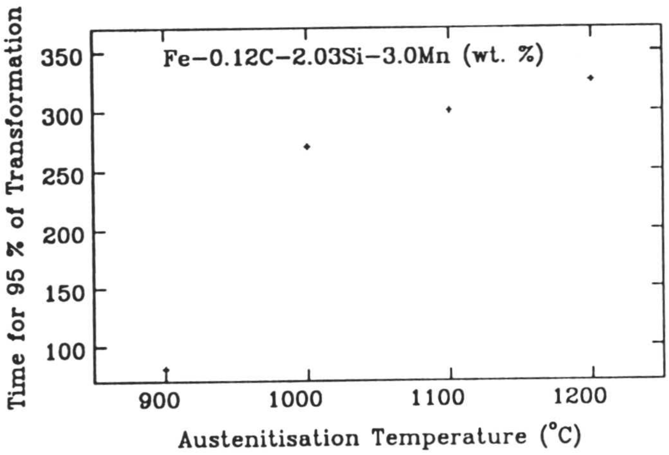

(b)

Fig. 6.12: *The effect of austenitisation temperature on the time taken by (a) 5 % and (b) 95 % of bainite transformation.*

6.3.3 *Transformation in Alloy A103*

This is the fastest transforming alloy of the three studied, making the study of kinetics rather difficult in this alloy. The optical microstructure is illustrated in Fig. 6.13, and appears different from those of alloys A2 and A102, presumably because a lot more of the austenite transform to bainite.

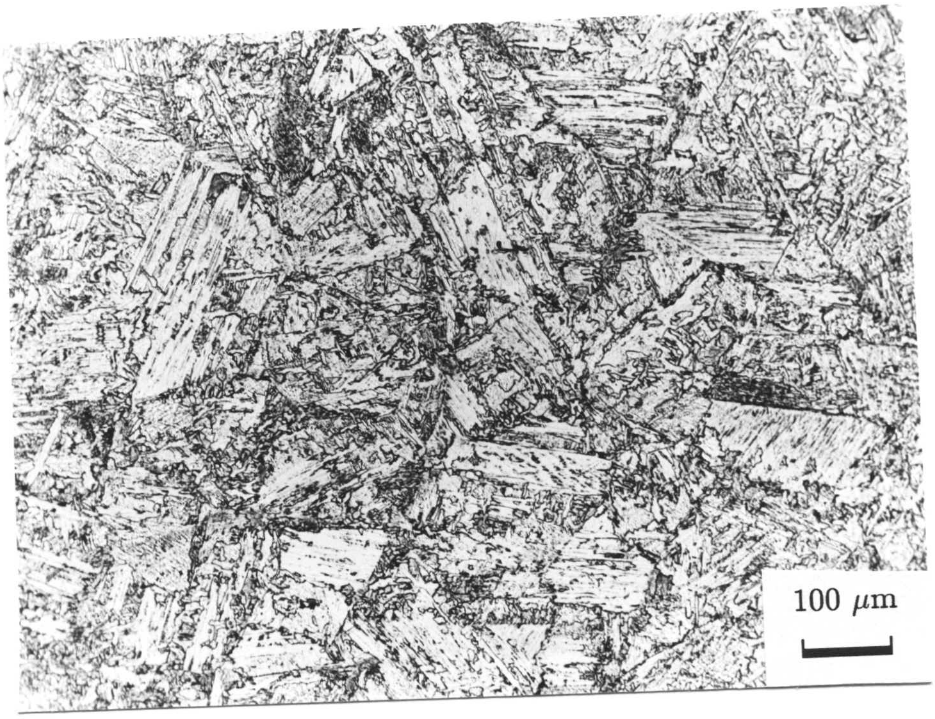

Fig. 6.13: *Optical micrograph showing the morphology of bainite in alloy A103, specimen isothermally transformed to bainite at 530 °C after austenitisation at 1100 °C for 5* min.

The effect of austenitisation temperature on the kinetics of bainite transformation are shown in Fig. 6.14, which shows that there is very little detectable effect of austenitisation temperature on the formation of bainite, simply because the kinetics are so rapid as to mask any grain size effect.

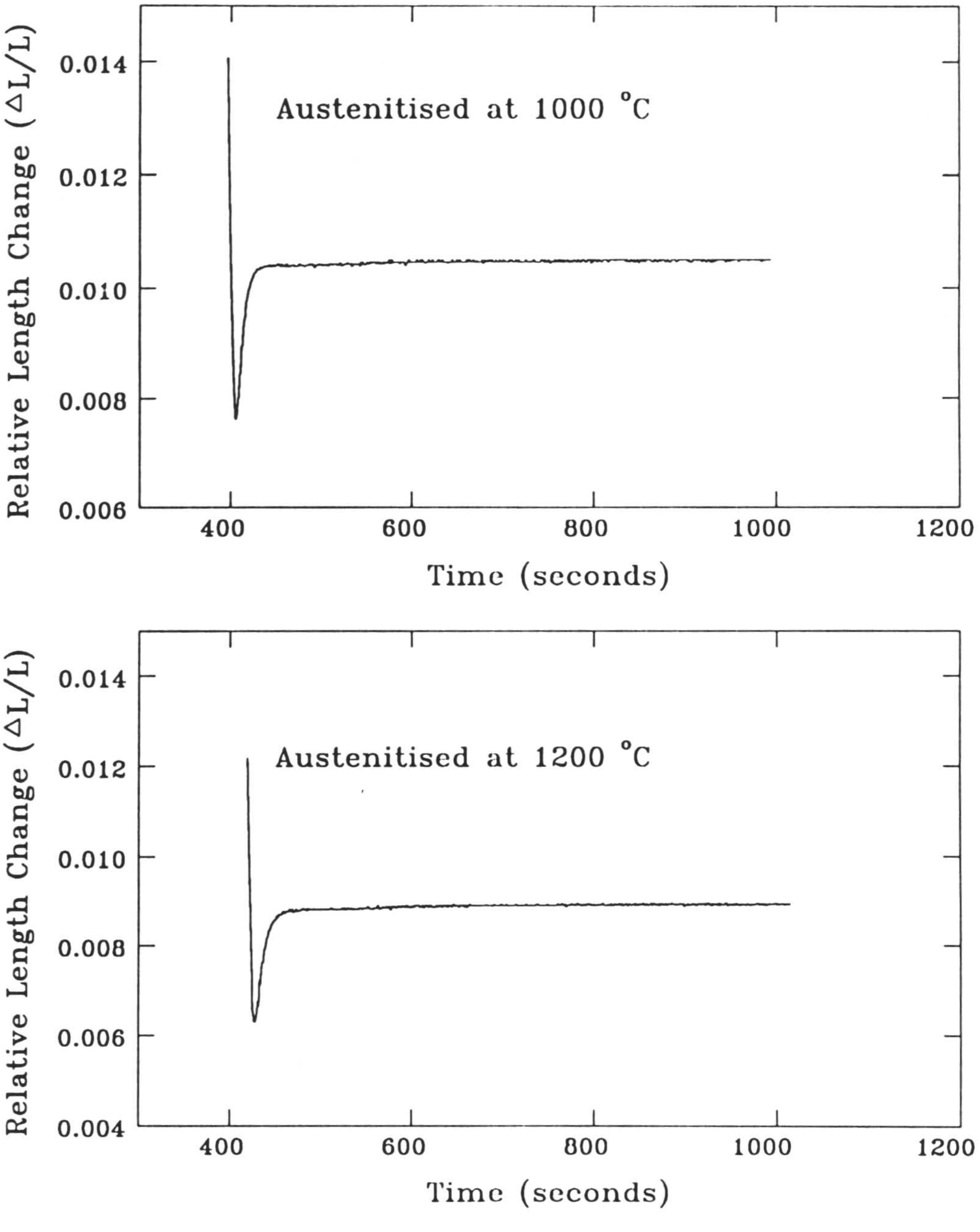

Fig. 6.14: *Dilatometric curves showing the effect of austenitisation temperature on the kinetics of bainitic reaction in alloy A103.*

It was considered extremely important to determine whether any transformation occurred during cooling from the austenitisation temperature. Fig. 6.15 shows that there is no undesired transformation during cooling. bainite.

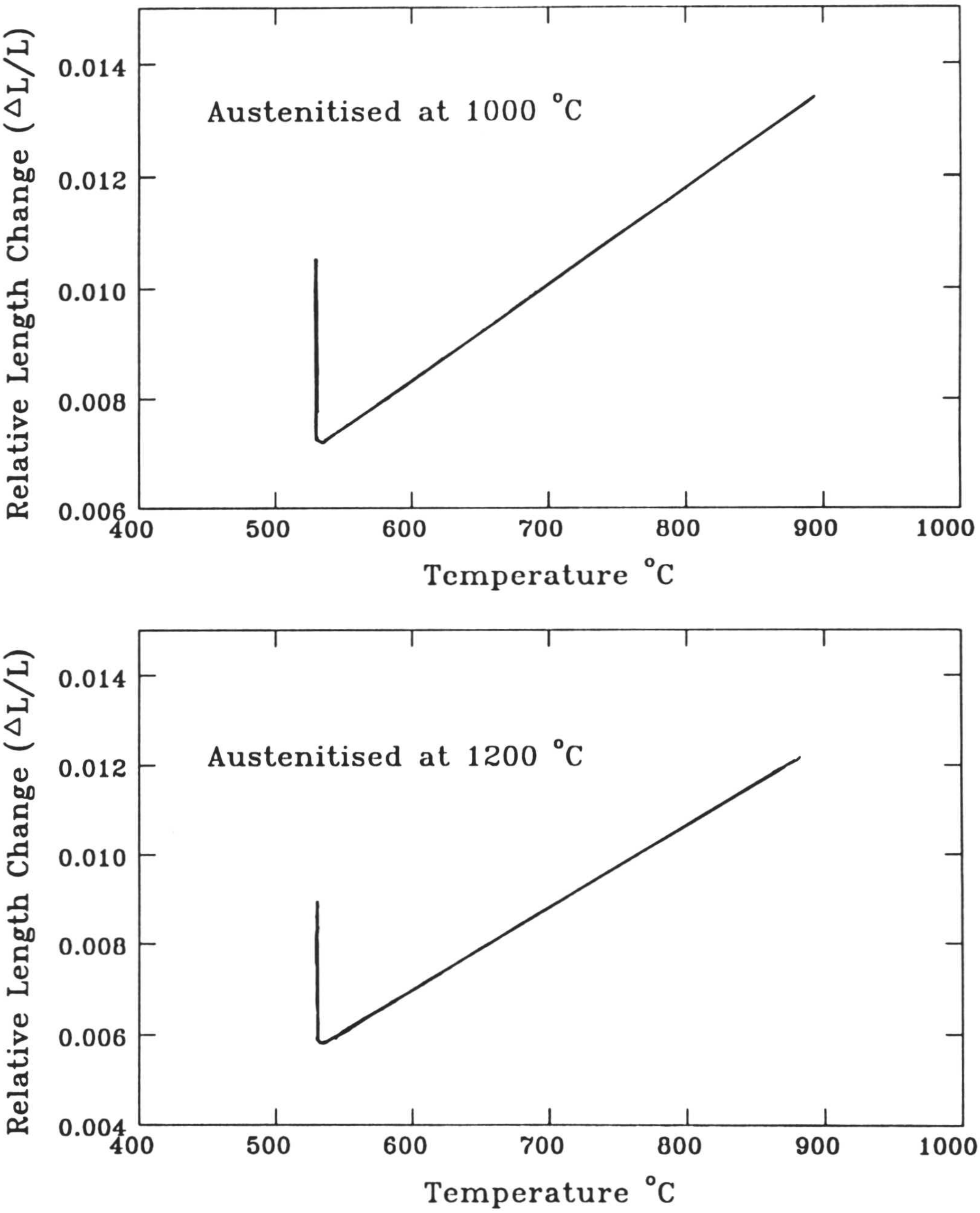

Fig. 6.15: *Relative length versus temperature dilatometric curves showing that there is no transformation during cooling prior to isothermal transformation in alloy A103.*

The micrographs in Fig. 6.16 show the effect of austenitisation temperature in the microstructure, which could be described as "granular" morphology.

(a)

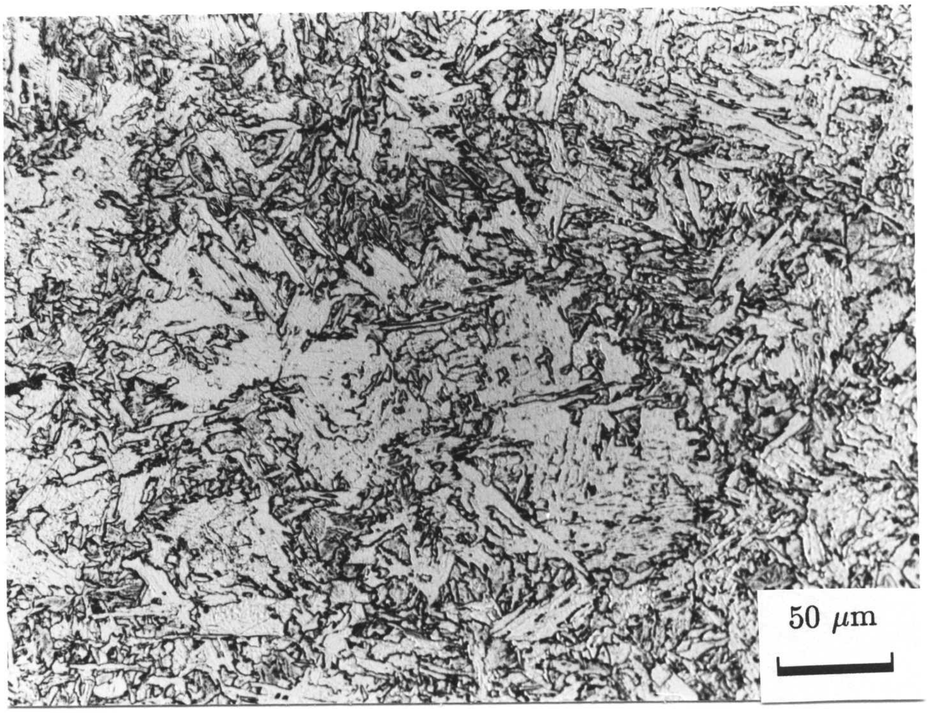

(b)

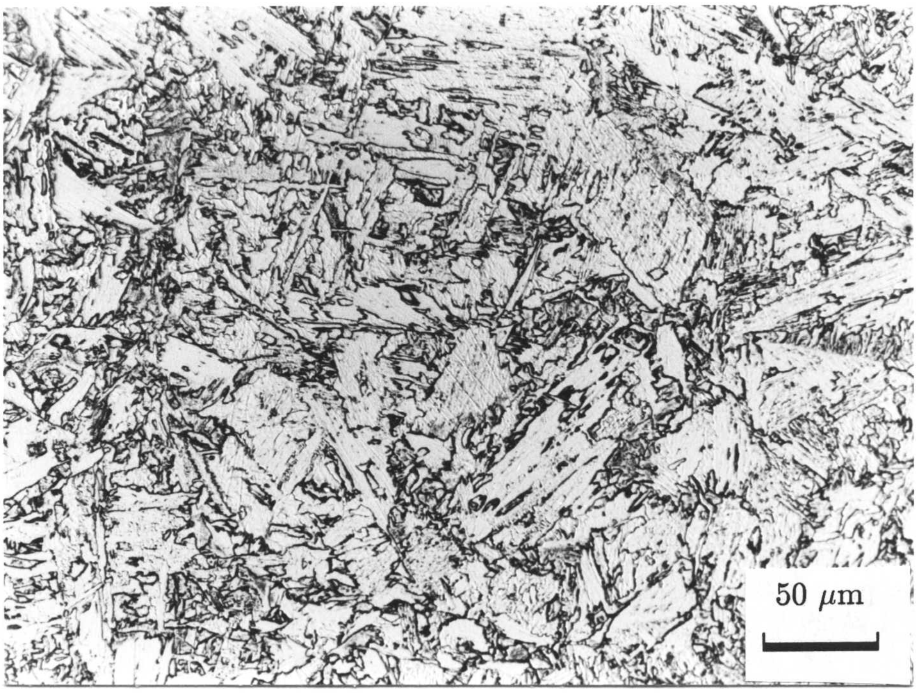

Fig. 6.16: *Optical micrographs showing the effect of austenitisation temperature on bainite microstructure in alloy A103.*

6.3.4 *Austenite Grain Size*

Increasing the austenitisation temperature, resulted in a bigger austenite grain size (Figs. 6.17) as measured by using the thermal grooving technique. The grain sizes were measured using the mean lineal intercept (m.l.i) method (Fig. 6.17).

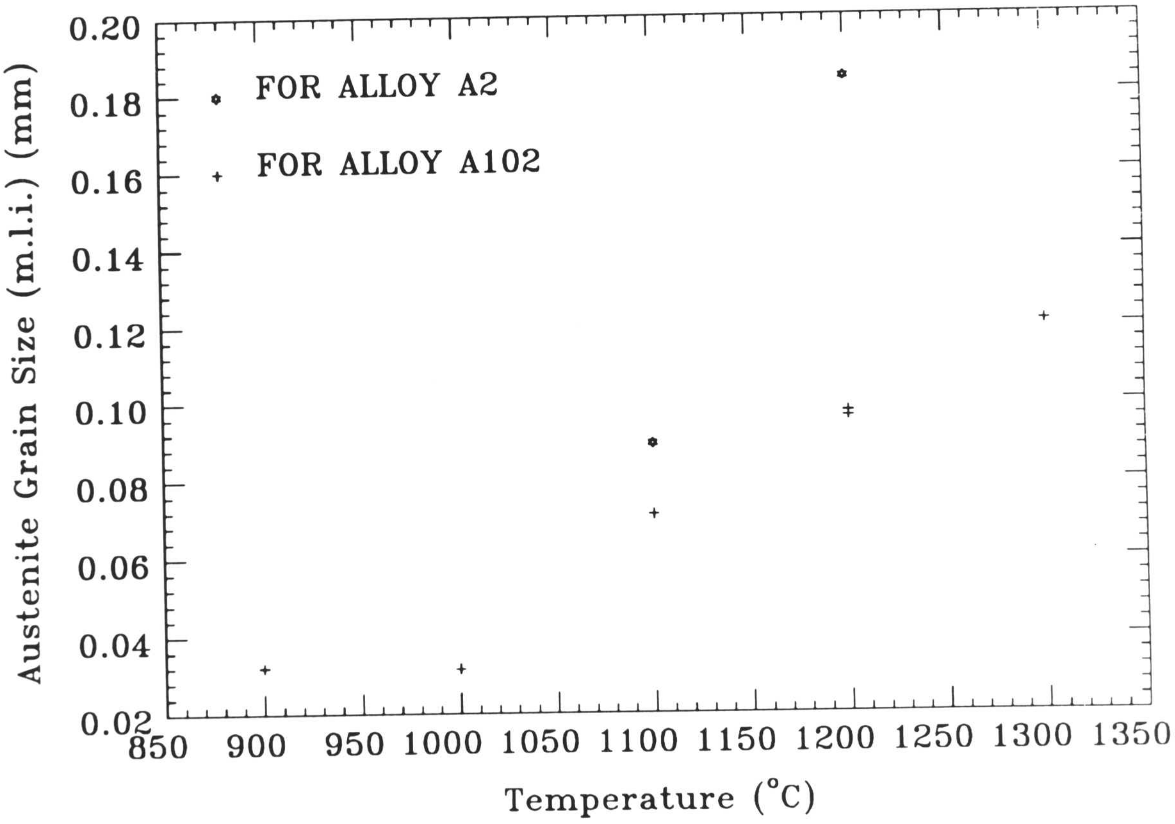

Fig. 6.17: *Effect of austenitisation temperature on austenite grain size measured by mean linear intercept method.*

6.4 Summary

Controlled experiments have been carried out on the influence of austenite grain size on the overall transformation kinetics of the bainite reaction in steels where carbide precipitation (or other reactions) do not accompanying the formation of bainitic ferrite. The primary result is that the reaction rate increases as the austenite grain size is reduced, a result expected in high purity steels where the main site for bainite nucleation is the austenite grain surfaces. The experiments nevertheless needed to be carried out since the published literature conflicting results. A further observation is that the austenite grain size effect might be marked in steels which tend to transform rapidly when compared with the ability of the experimental techniques to resolve the rate of reaction. There are some puzzling observations which need further investigation; Figs. 6.6 and 6.11 indicate that the maximum extent of transformation achieved by prolonged holding at the isothermal reaction temperature, varies with the austenitising temperature. Furthermore, the variation is not systematic, being different for alloy A2 and A102. These results will require further investigation, to confirm the behaviour and to identify the cause. It is speculated that changes in crystallographic texture might tend to make dimensional change a less reliable indicator of the extent of transformation, since a non-random distribution of bainite sheaves could be expected to lead to anisotropic dimensional changes since the invariant plane strain shape change during bainite growth is far from isotropic. In a small grained sample, the anisotropic terms would tend to cancel, bearing just the dilatational components to reflect the extent of reaction.

♣♣♣

Chapter 7

INTRAGRANULAR NUCLEATION OF BAINITE SHEAVES

7.1 Introduction

When austenite decomposes to ferrite, the ferrite is almost always found to nucleate heterogeneously at the austenite grain boundaries, irrespective of the nature of the ferrite transformation products (*i.e.,* allotriomorphic ferrite, Widmanstätten ferrite, pearlite, bainite). Intragranular nucleation is rare indeed in wrought steels. As discussed in the earlier chapter on intragranularly nucleated Widmanstätten ferrite, there are distinct advantages from mechanical properties point of view in industry that intragranular nucleation of ferrite, especially of ferrite plates which otherwise tend to form in packets of parallel plates in identical orientation, packets which do not effectively deflect cleavage cracks.

The purpose of the work presented here was to induce the intragranular nucleation of bainite sheaves by rendering the austenite grains surfaces ineffective by decorating them with thin layer of allotriomorphic ferrite prior to bainite transformation.

7.2 Experimental Procedures

A high-purity high-hardenability Fe-0.12C-2.03Si-2.96Mn (wt. %) alloy was selected, the high silicon in order to retard formation of pearlite, the high manganese contributing towards hardenability, providing an effective means of controlling the thickness of the grain boundary allotriomorphic ferrite.

The material was received in the form of 10 mm diameter bars from which 3 mm diameter cylindrical specimens were prepared by swagging and machining§. All heat treatments, except those for surface relief experiments, were carried out using a Theta Industries high speed dilatometer; the heat treatment cycles used are shown in Fig. 7.1. The samples were nickel plated to approximately 0.08 mm thickness to avoid surface nucleation surface degradation during the heat treatment.

Surface relief experiments were carried out using electrical resistance heating furnaces. After metallographic preparation, the specimens were sealed in silica tubes after flushing several times with high purity argon gas, then evacuating to 10^{-6} torr before finally sealing off with a partial pressure of argon gas§.

---

§ The details of swagging treatments, specimen preparation and other experimental procedures are described in Chapter 3.

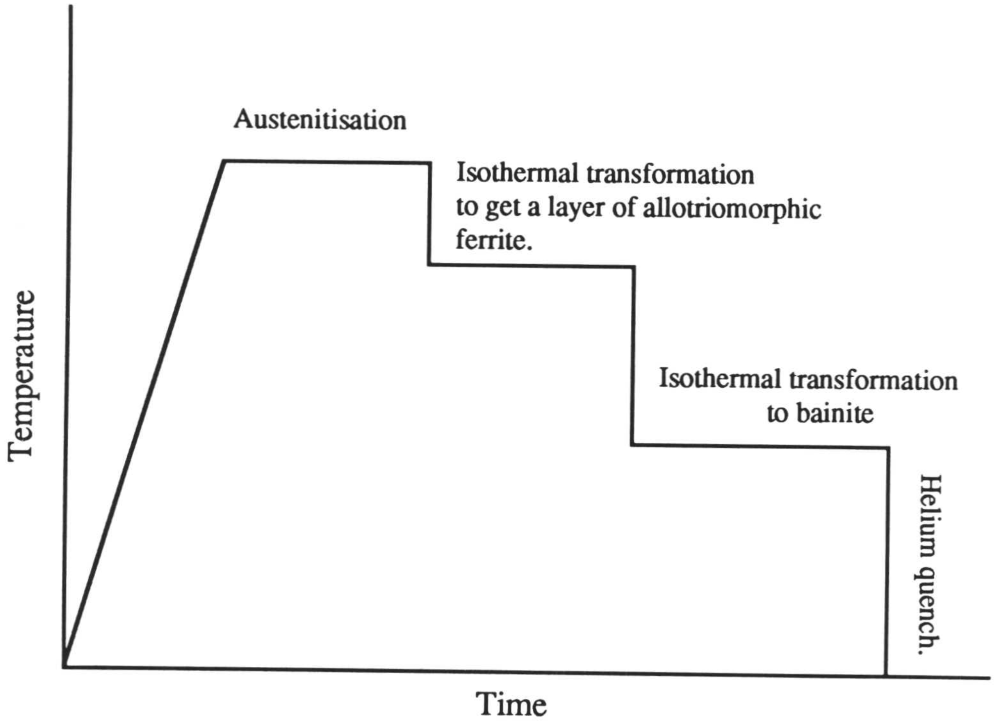
Austenitisation
Isothermal transformation to get a layer of allotriomorphic ferrite.
Isothermal transformation to bainite
Helium quench.
Temperature
Time

Fig. 7.1: *Schematic representation of heat treatment cycles used in the present study.*

Any surface relief effects were imaged using the Nomarski differential interference technique on a Zeiss optical microscope.

7.3 Results and Discussion

The time-temperature-transformation diagrams calculated using the method of Bhadeshia [1982] is presented in Fig. 7.2, and the transformation temperatures in Table 7.1.

Table 7.1: *Calculated Ae_3, Ae'_3, W_S, B_S, and M_S temperatures for the steel used.*

	Ae_3	Ae'_3	W_S	B_S	M_S
Temperature °C	812	776	740	520	390

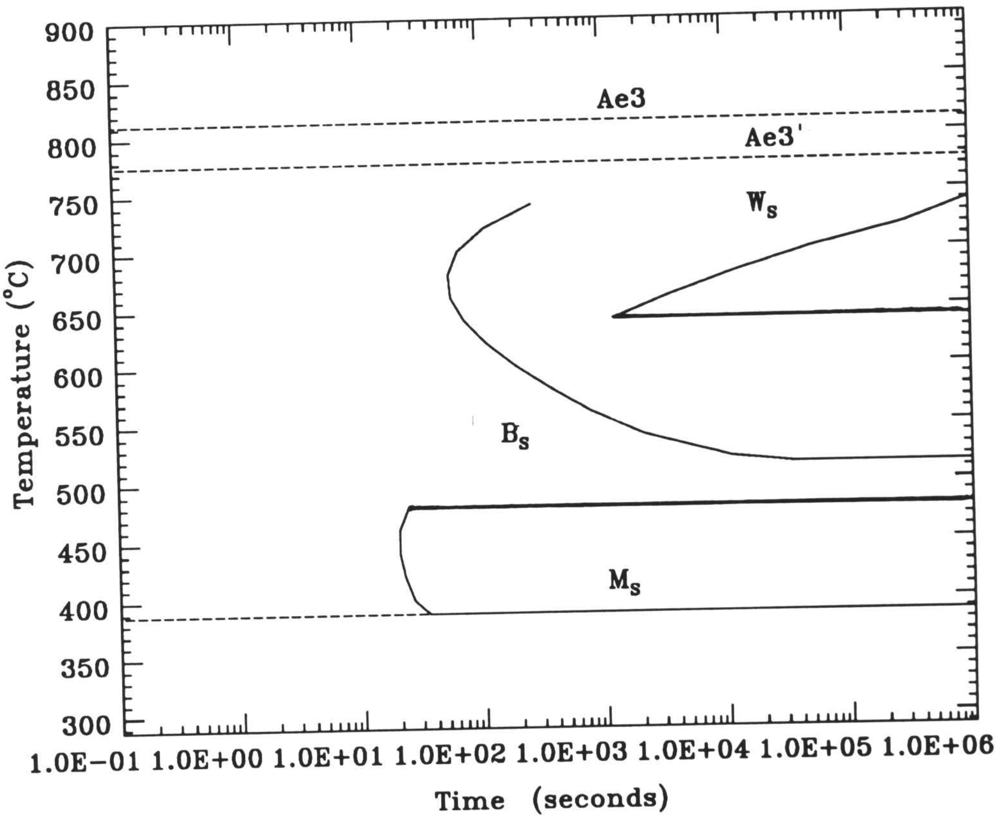

Fig. 7.2: *Time-temperature-transformation diagram for the steel used.*

In order to eliminate the austenite grain boundary nucleation sites; layers of allotriomorphic ferrite were introduced by isothermal transformation before cooling rapidly into the bainite transformation temperature range. The formation of a uniform layer of the grain boundary allotriomorphic ferrite was a problem due to the relatively fast reaction kinetics and therefore, a series of specimens were isothermally transformed at variety of temperatures for different time periods. Fig. 7.3 shows the results of some of the successful heat-treatments. Austenitisation at 1100 °C for 5 min followed by isothermal transformation at 720 °C for 30 min resulted in fairly uniform and thin layers of grain boundary allotriomorphic ferrite, so that this heat-treatment was selected for further experiments, and that temperature 720 °C is henceforth T_1.

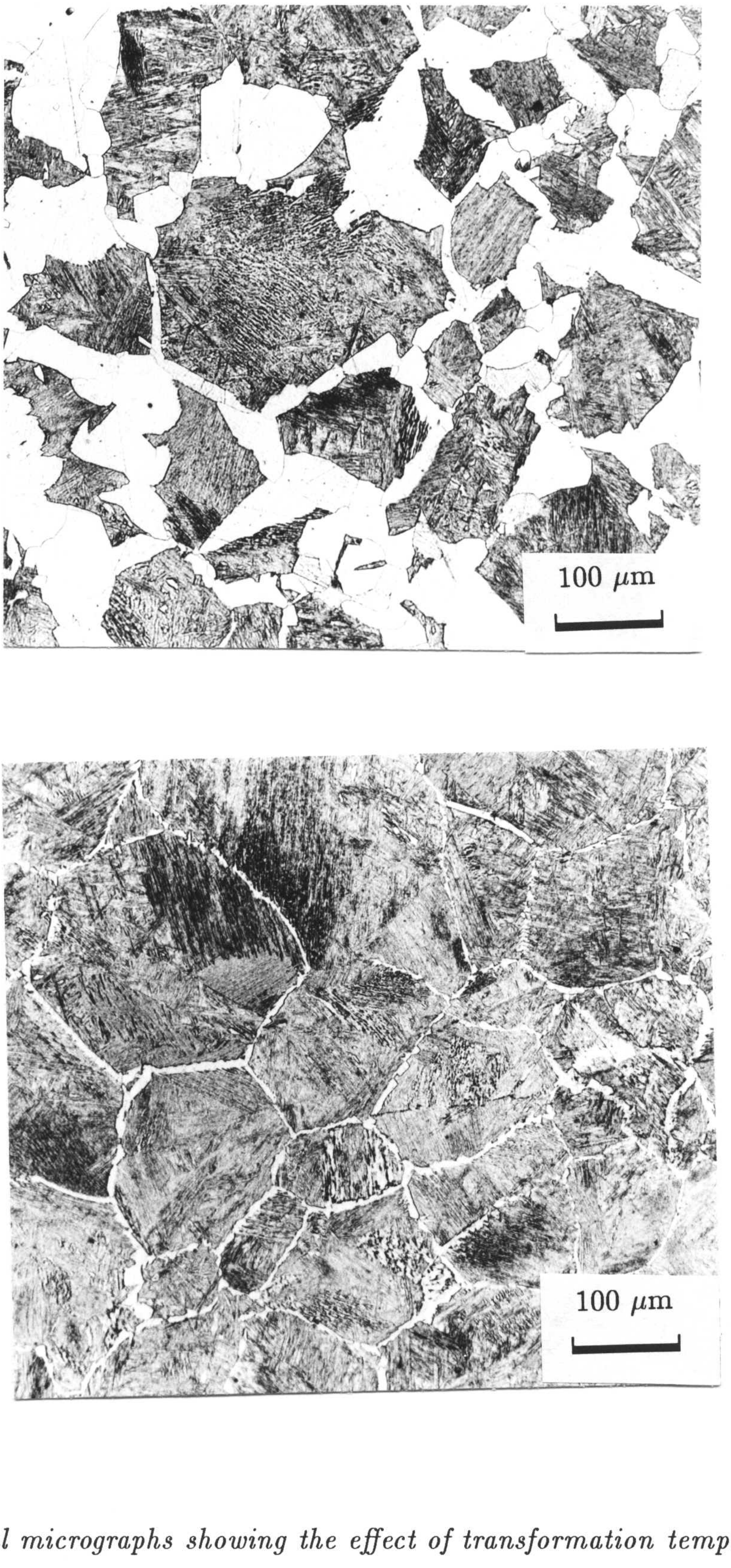

Fig. 7.3: *Optical micrographs showing the effect of transformation temperature and time on the formation of grain boundary allotriomorphic ferrite. (a) 1100 °C @ 10* min → *740 °C @ 3* hr. *(b) 1100 °C @ 10* min → *720 °C @ 2000* s.

The thickness of grain boundary allotriomorphic ferrite layers as measured on a randomly polished and etched metallographic specimen was around 4-6 μm . This left plenty of untransformed austenite available for further intragranularly nucleated bainite transformation at a lower temperature T_2. The schedule of heat-treatments is presented in Table 7.2

Table 7.2: *Heat treatment schedule.*

Specimen No.	Heat Treatment
A102AW01	1100 ^{o}C @ 10 min → 720 ^{o}C @ 2000 s
A102AW02	1100 ^{o}C @ 10 min → 740 ^{o}C @ 3 hr
A102AW03	1100 ^{o}C @ 10 min → 720 ^{o}C @ 1000 s → 500 ^{o}C @ 1000 s
A102AW04	1100 ^{o}C @ 10 min → 720 ^{o}C @ 1000 s → 450 ^{o}C @ 1000 s
A102AW05	900 ^{o}C @ 10 min → 720 ^{o}C @ 1000 s → 450 ^{o}C @ 1000 s
A102AW06	1200 ^{o}C @ 10 min → 720 ^{o}C @ 1000 s → 450 ^{o}C @ 1000 s
A102AW07	1100 ^{o}C @ 10 min → 720 ^{o}C @ 1000 s → 450 ^{o}C @ 60 s
A102AW08	1100 ^{o}C @ 10 min → 720 ^{o}C @ 800 s → 500 ^{o}C @ 60 s
A102AW09	1100 ^{o}C @ 10 min → 720 ^{o}C @ 1000 s → 540 ^{o}C @ 60 s
A102AW10	1100 ^{o}C @ 10 min → 720 ^{o}C @ 400 s → 500 ^{o}C @ 60 s
A102AW11	1100 ^{o}C @ 10 min → 720 ^{o}C @ 30 min → 450 ^{o}C @ 1000 s

Fig 7.4 shows the typical microstructure resulting from the two-stage heat treatment. It consists of sheaves of bainite nucleated within the body of the austenite grains and what appears to be thin laths of ferrite nucleated from allotriomorphic ferrite layers. The ferrite laths were in fact found to have a sub-unit type structure on examinations at higher magnifications Fig. 7.5.

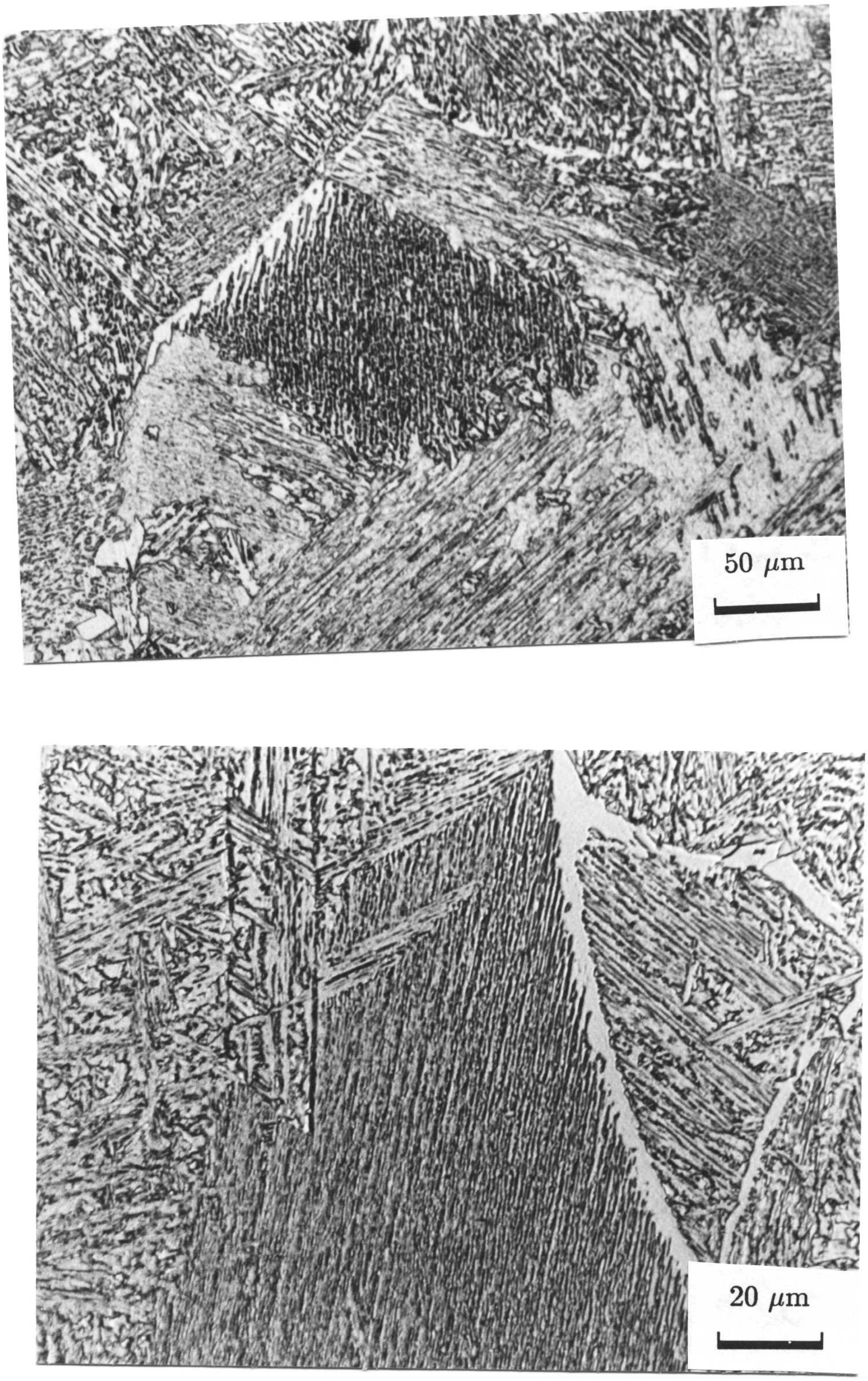

Fig. 7.4: *Optical micrographs showing the microstructure of the specimen which was isothermally transformed below the* B_S *temperature after the formation of grain boundary allotriomorphic ferrite (1100* ^oC *@ 10* min → *720* ^oC *@ 30* min → *450* ^oC *@ 1000* s*).*

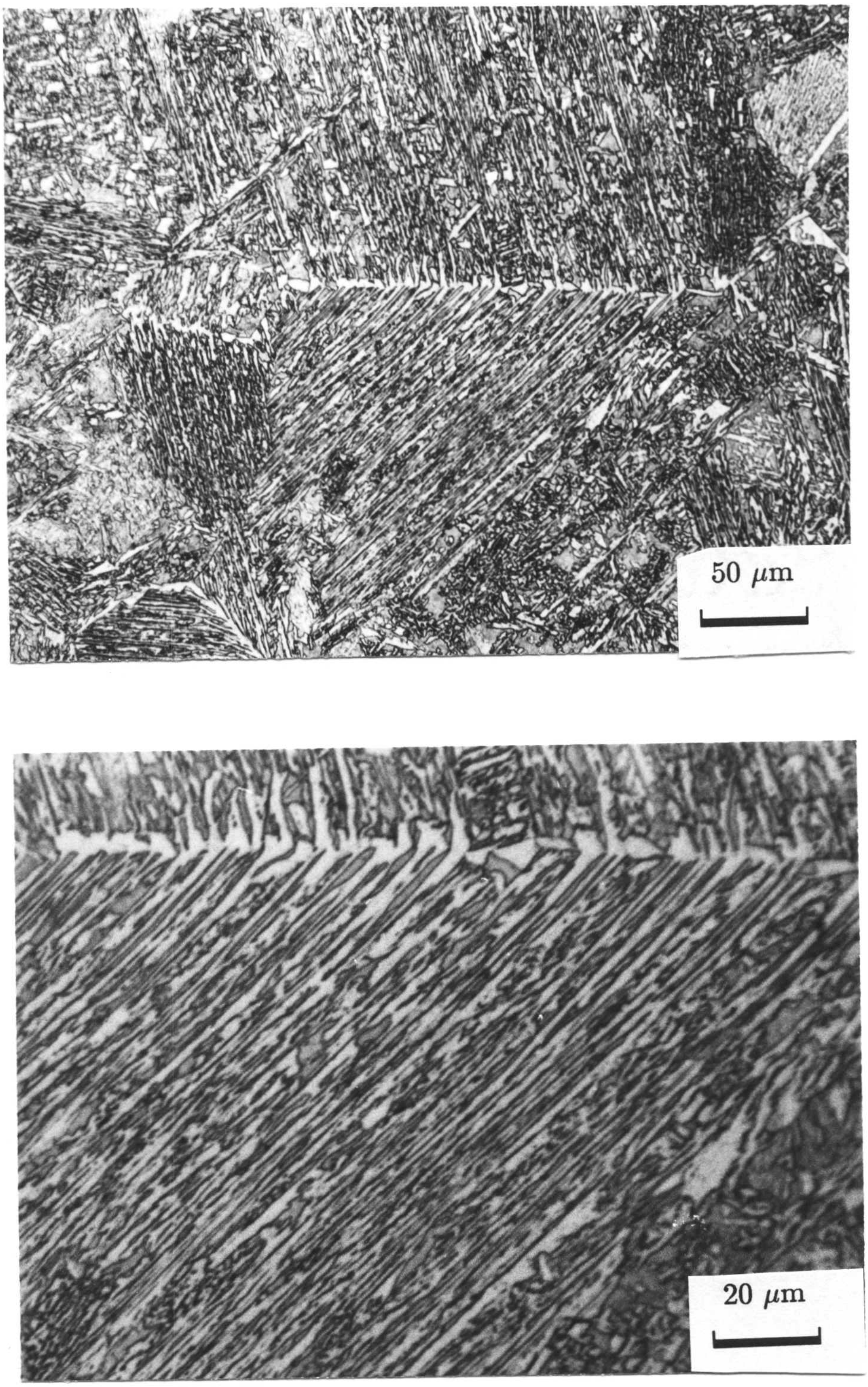

Fig. 7.5: *Optical micrographs showing the sub-unit type microstructure of the ferrite laths nucleated from grain boundary allotriomorphic (GBA) ferrite. Specimen isothermally transformed at 500 °C for 1000* s *after austenitisation at 1100 °C for 10* min *and after the formation of GBA layer at 720 °C.*

The observation of intragranular nucleation was not completely convincing, so a higher austenitisation temperature (1200 °C) was used to decrease the number density of grain boundary nucleation sites. This resulted in the microstructure shown in Fig. 7.6, where intragranular nucleation has produced a different microstructure in the austenite grain centres composed with that in the vicinity of the grain boundaries.

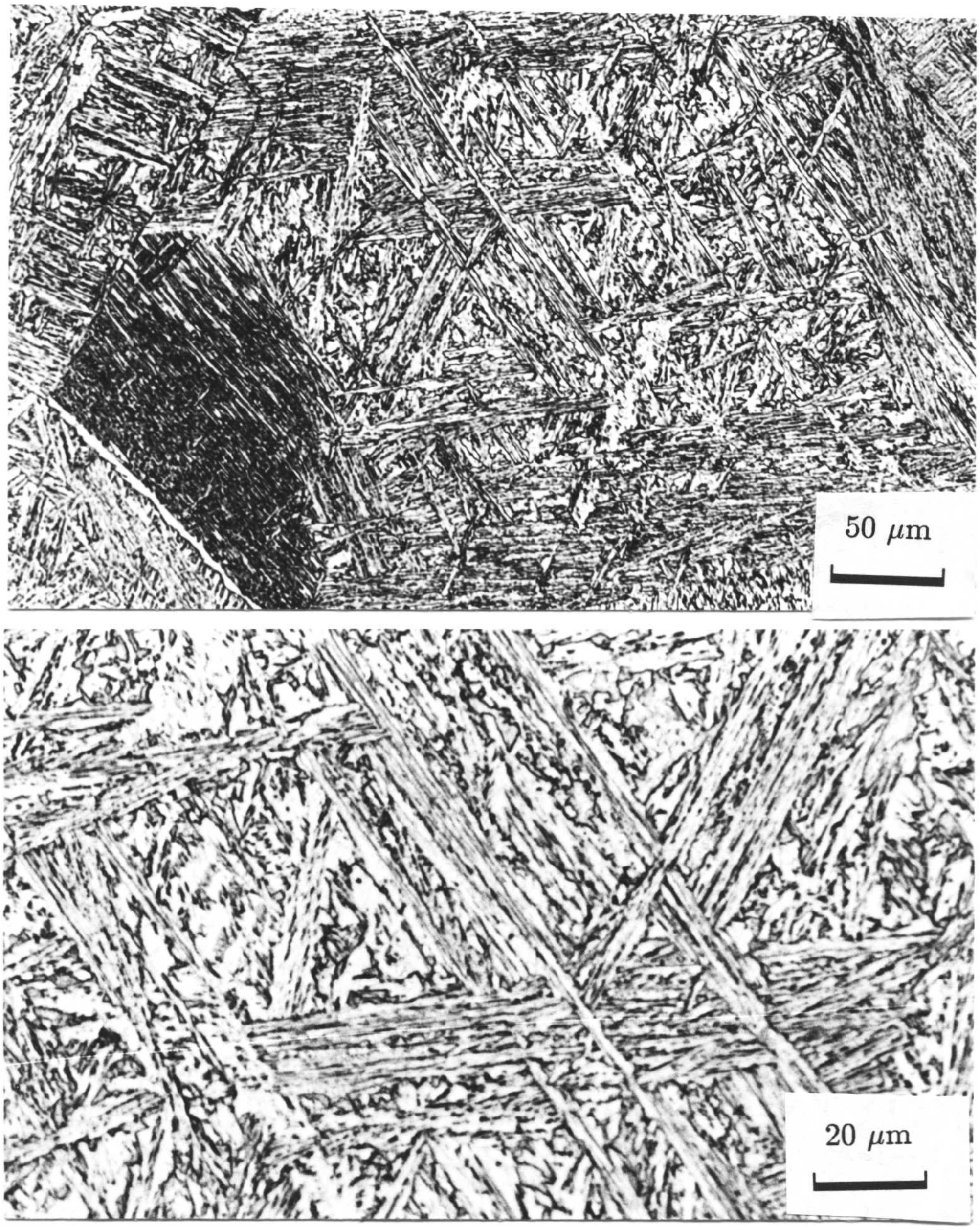

Fig. 7.6: *Optical micrographs showing the microstructure of the specimen which was isothermally transformed below the* B_S *temperature after the formation of grain boundary allotriomorphic ferrite. Note the nucleation of bainite sheaves within the body of the prior austenite grain (1200 °C @ 10* min → *720 °C @ 1000* s → *450 °C @ 1000* s*).*

The scanning electron micrograph in Figs. 7.7 and 7.8, show more detail from both of the regions. Transmission electron microscopy confirmed that the two kinds of bainite are essentially identical in structure, except for the much larger tendency for the grain boundary nucleated sheaves to ferrite plates (Fig. 7.9).

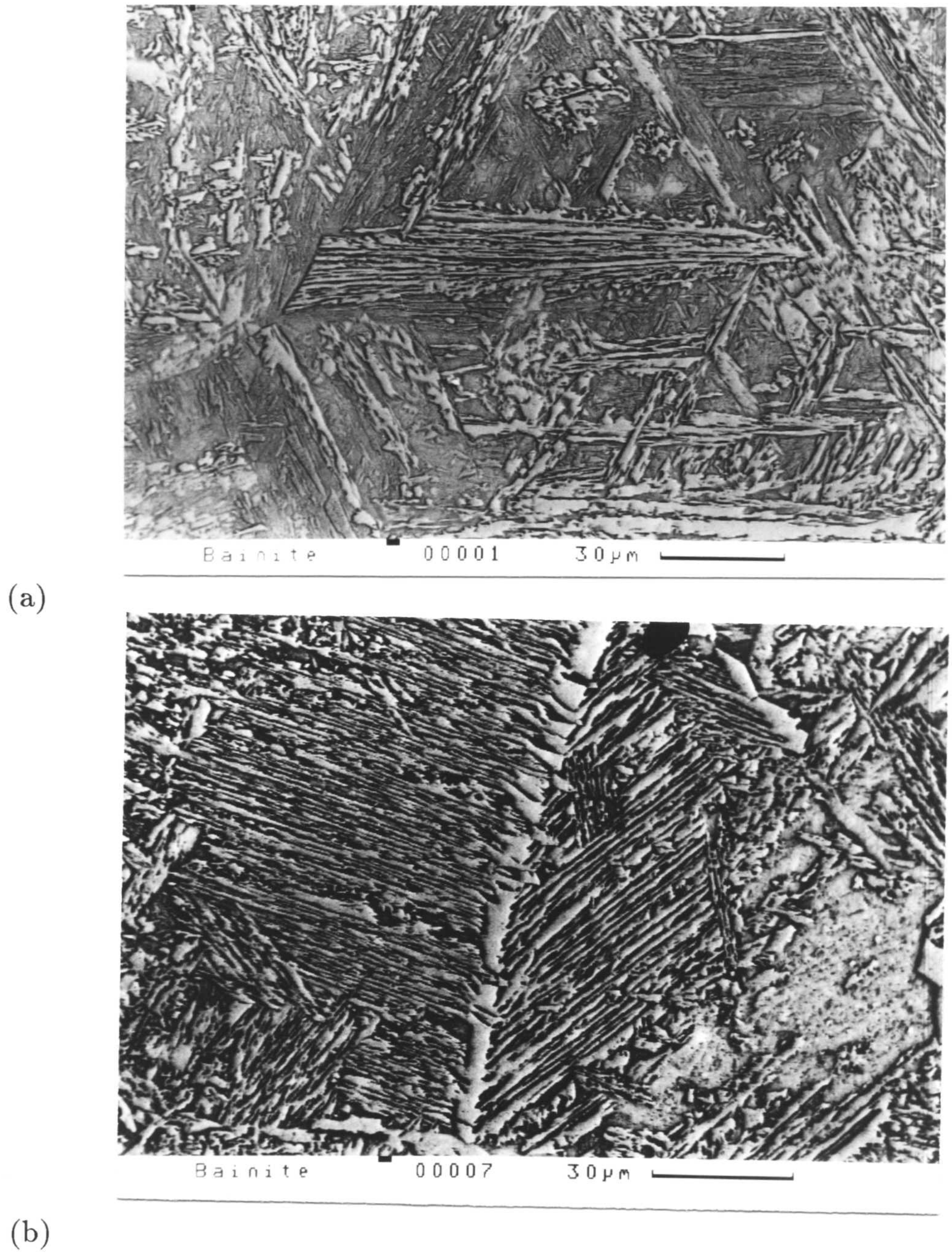

Fig. 7.7: *SEM micrographs showing the microstructure of the specimen which was isothermally transformed below the* B_S *temperature after the formation of grain boundary allotriomorphic ferrite. Note the nucleation of bainite sheaves within the body of the prior austenite grain. (a) 1200 °C @ 10* min → *720 °C @ 1000* s → *450 °C @ 1000* s. *(b) 1100 °C @ 10* min → *720 °C @ 1000* s → *500 °C @ 1000* s*).*

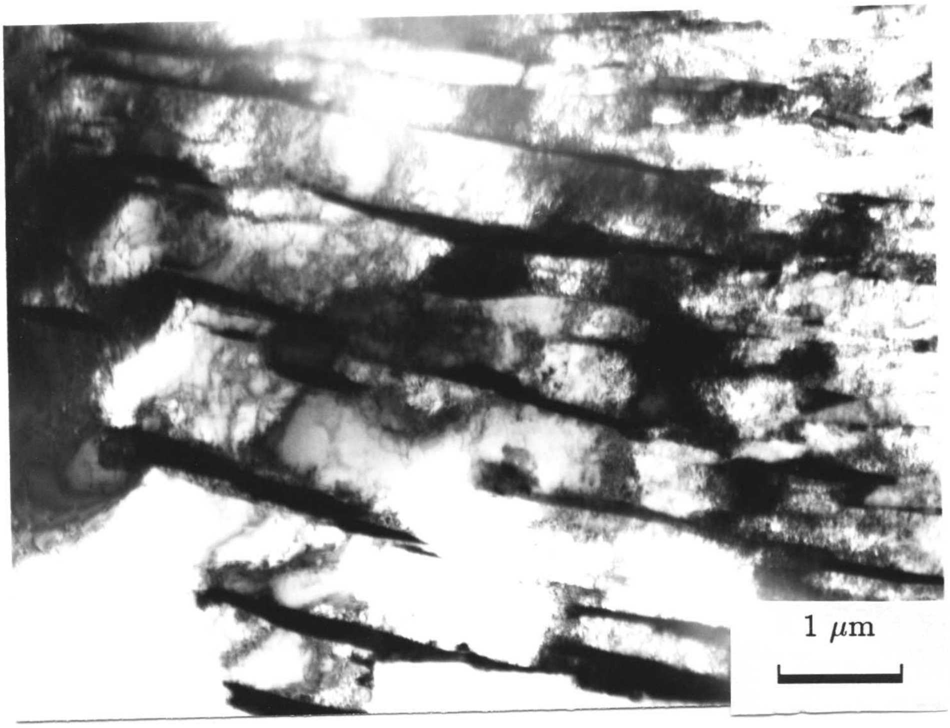

(a)

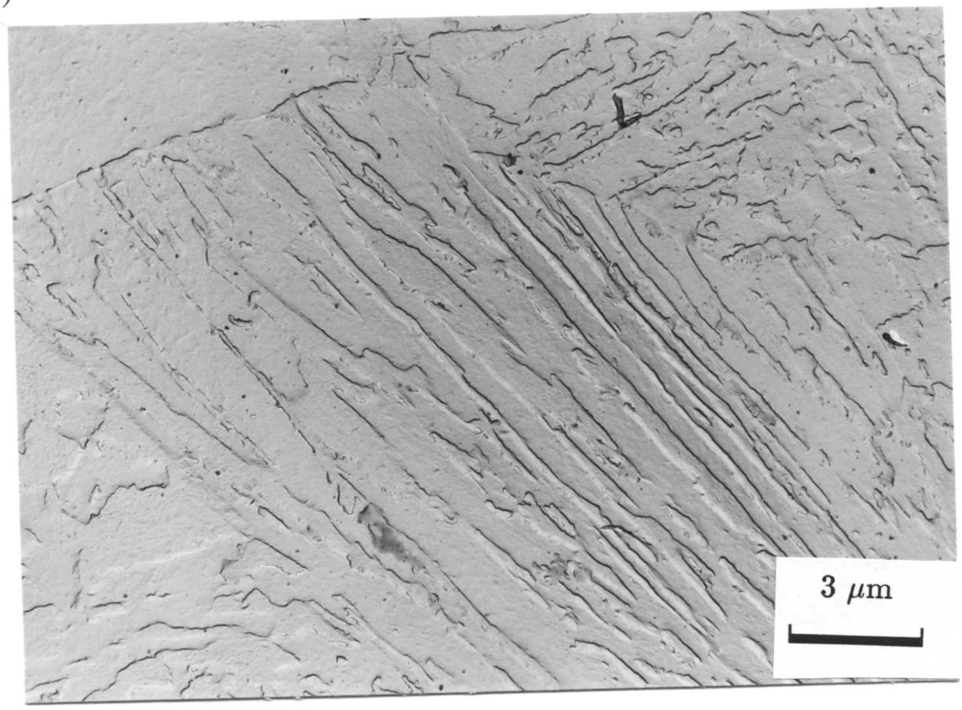

(b)

Fig. 7.8: *Micrographs showing the nucleation of bainite sheaves from the grain boundary allotriomorphic ferrite. Note the sub-units structure of bainitic ferrite within the sheaves (1100 °C @ 10* min → *720 °C @ 1000* s → *450 °C @ 60* s). *(a) TEM. (b) Carbon extraction replica.*

It was possible using extraction replica (Fig. 7.9) to indentify some of the inclusions which could have served as the required intragranular nucleation sites.

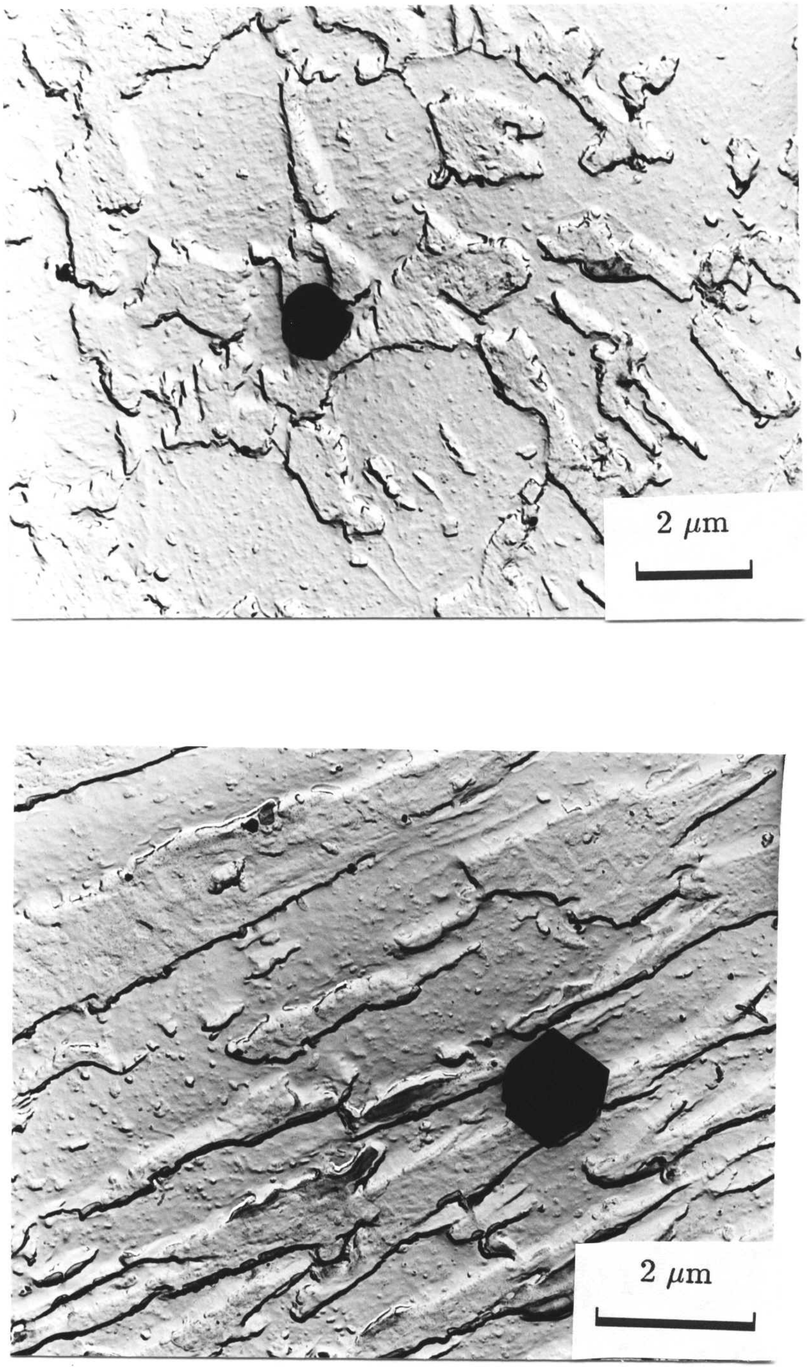

Fig. 7.9: *Replica electron micrographs showing the inclusion assisted nucleation of bainite sheaves (1100 °C @ 10* min → *720 °C @ 30* min → *450 °C @ 1000* s*).*

7.4 Dilatometry

Dilatometric experiments were carried out to check whether there is any unintended transformation during cooling to the B_S temperature, which might interfere with the formation of bainite. Fig. 7.10, is a plot of the relative length change versus temperature, the linearity of which demonstrates the absence of any reaction during cooling to the desired isothermal transformation temperatures.

The dilatometric data were converted to volume fractions and Table 7.3 shows the extent of reaction at the isothermal reaction temperatures together with the calculated carbon enrichment in the residual austenite at each stage.

Table 7.3: *Measured volume fraction of ferrite and bainite and calculated carbon content of the residual austenite.*

Temperature ^oC	Total volume fraction of ferrite	Carbon in residual austenite wt. %
720	0.117 ± 0.012	0.134 ± 0.002
450	0.354 ± 0.016	0.178 ± 0.004

7.5 Surface Relief Study

It is well known that displacive reactions cause an invariant-plane strain shape change in the transformed regions. Fig 7.11 shows the surface relief produced on a specimen given the two-stage heat-treatment. It is clear, as expected, that there is no shape change associated with allotriomorphic ferrite growth, whereas there is pronounced relief associated with bainite.

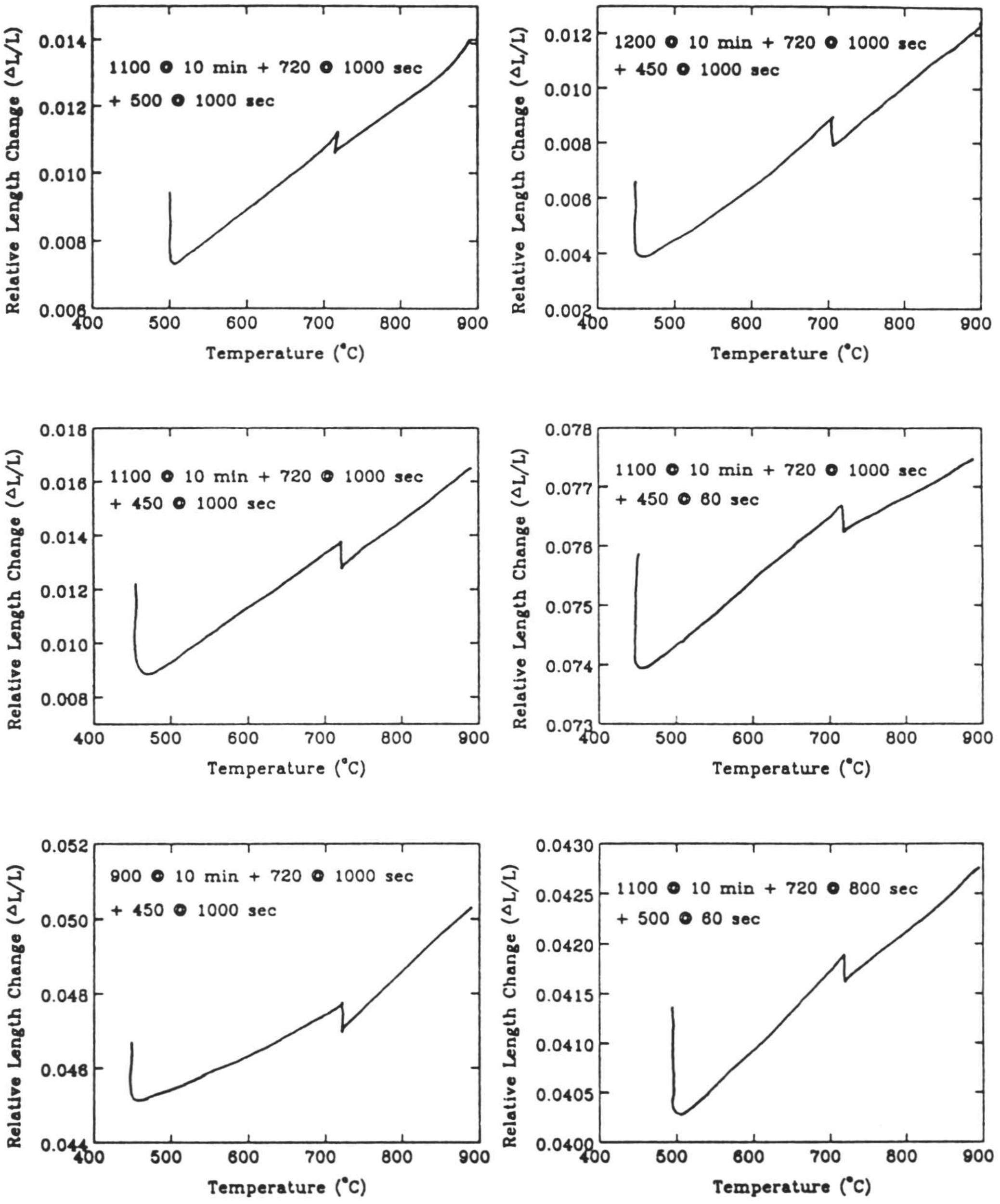

Fig. 7.10: *Continued.....*

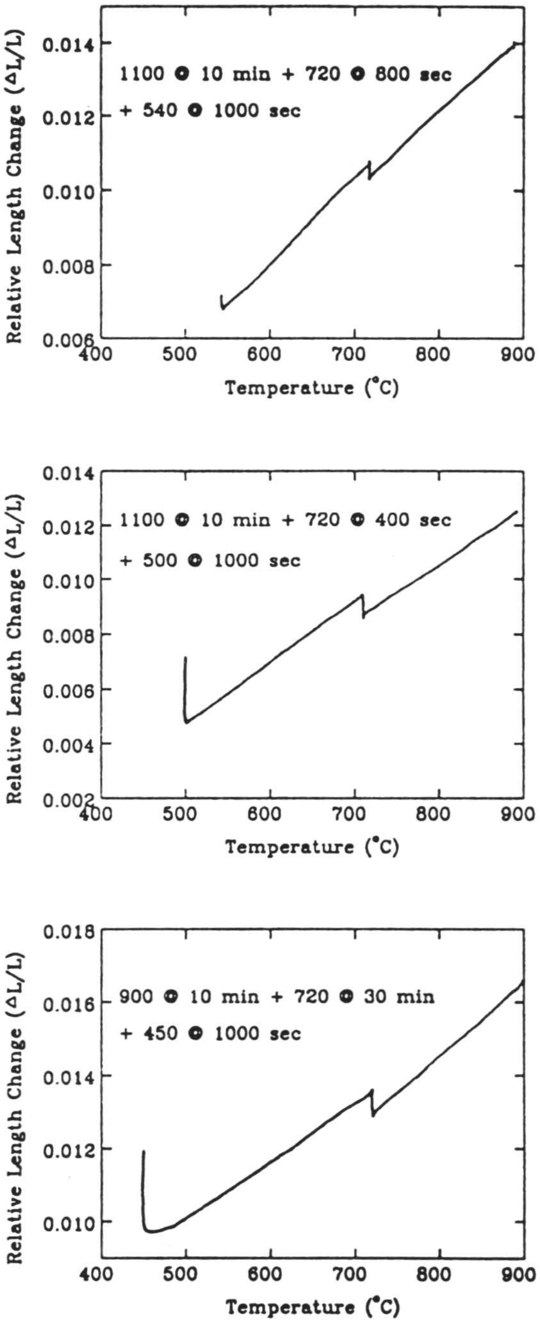

Fig. 7.10: *Dilatometric graphs between the relative length change and temperature showing that there is no transformation above the* B_S *temperature.*

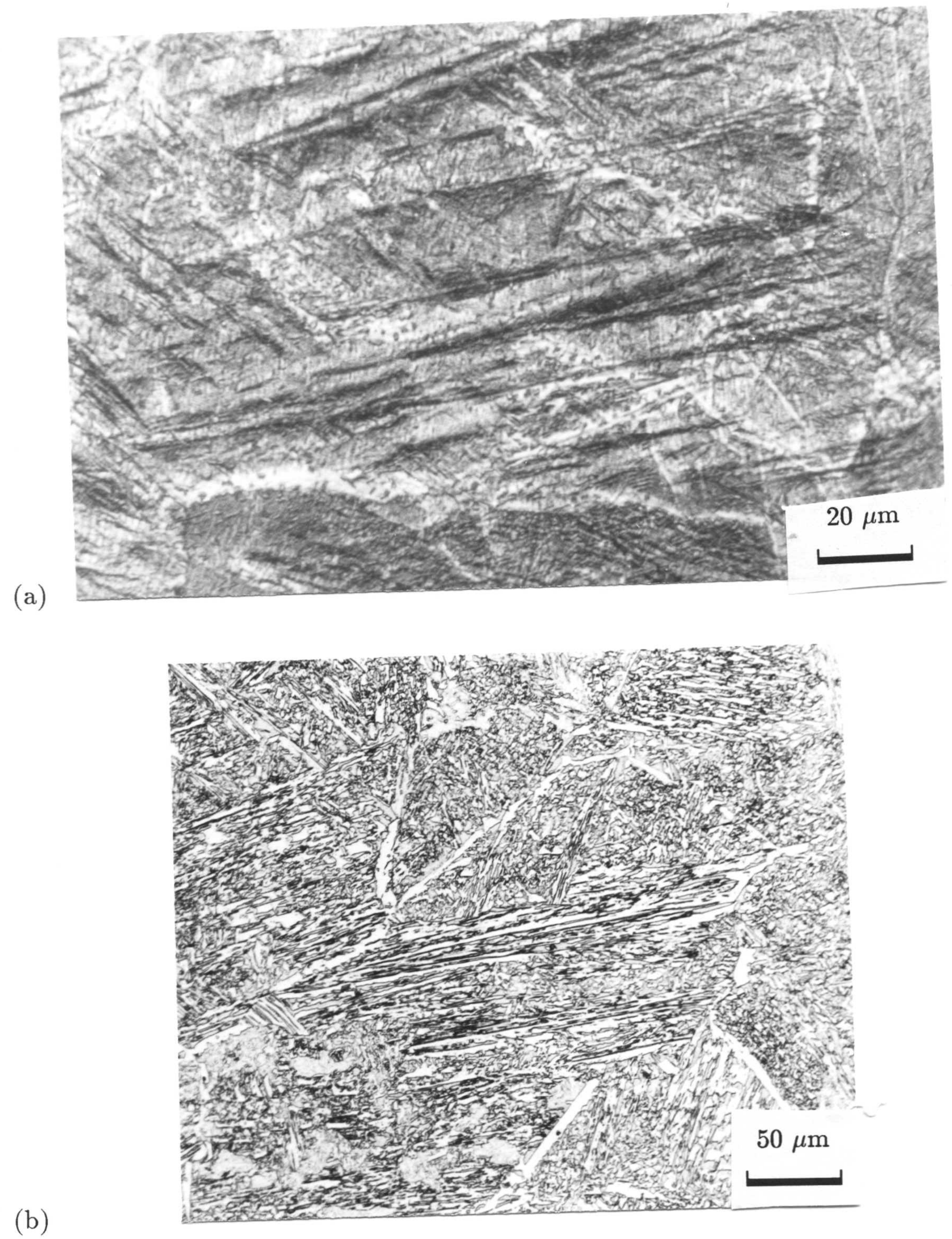

Fig. 7.11: *(a) Optical micrographs showing the surface relief produced by bainite sheaves. Note that diffusionally formed allotriomorphic ferrite did not show any surface relief. (b) Optical micrographs of the same specimen in (a) after slight polishing on 6* μm *diamond paste and etched in 2 % nital solution, showing the underlying microstructure. (1100 °C @ 10* min → *720 °C @ 30* min → *450 °C @ 1000* s*).*

7.6 Summary

A clear change in microstructure has been observed when the austenite grains boundaries are prevented from nucleating bainite, by covering them with thin layers of allotriomorphic ferrite. When specimens partially transformed to allotriomorphic ferrite are then held at a temperature below B_S, bainite sheaves nucleate intragranularly, probably on non-metallic inclusions present in steel, although the details required further investigation. However, it is found that some of the allotriomorphs, presumably those which have a favoured orientation relationship (*i.e.,* K-S or N-W type) with the austenite, do develop into packets of parallel sheaves of bainite. This is unlike the behaviour noted when Widmanstätten ferrite is induced to form in samples partially transformed to allotriomorphic ferrite, presumably because the larger undercooling needed to produce bainite allows the barriers (to transformation) presented in the carbon-enriched region near the allotriomorphic ferrite layers can be overcome by the accompanying larger driving force. The effects of bainite nucleation on allotriomorphs can be mitigated by increasing the austenite grain size, but the microstructural changes associated with intragranularly nucleated bainite are nevertheless rather less spectaculated when compared with the intragranularly nucleated Widmanstätten ferrite.

♣♣♣

Chapter 8

ASPECTS OF THE NUCLEATION OF WIDMANSTÄTTEN FERRITE

8.1 Significance of Widmanstätten Ferrite

The requirement for ever increasing toughness in steels has placed restrictions on the use of carbon and other alloying additions, thereby resulting in the development of the "high-strength low-alloy" steels. These steels, used in applications where weld ability and formability are of paramount importance, invariably have a very low carbon content (< 0.1 wt %). The total alloy concentration is usually less than 3.0 wt. %. One of the major problems with their development is the steel used for the weld deposits themselves, which sometimes contain undesirable quantities of Widmanstätten ferrite.

Widmanstätten ferrite is an undesirable constituent and its presence leads to poor toughness in low-alloy steels [Savage and Aaronson, 1966; Garland and Kirkwood, 1975; Rodrigues and Rogerson, 1977]. The long plate-like morphology so characteristic of Widmanstätten ferrite offers little resistance to cleavage crack propagation when present in packets of parallel plates (Fig. 8.1); it has been suggested that this is because the packets offer a larger effective grain size, although the details are not clear [Widgrey, 1975; Fick and Rogerson, 1977; Billy *et al.* 1980]. The plates in individual packets are in identical orientation in space.

The problem of the unwanted Widmanstätten ferrite is particularly acute in steel weld deposits, where it is impractical to modify the microstructure which evolves during solidification and during subsequent cooling to ambient temperature, by the sort of thermomechanical processing normally used to refine the microstructure in wrought alloys. Consequently, the main avenue available for the minimisation of the quantity of Widmanstätten ferrite is alloy design, and this in turn requires a good knowledge of the factors controlling its nucleation and growth.

8.1.1 *Scope and the Problem*

The growth of Widmanstätten ferrite is reasonably well understood and the lengthening rate of an individual Widmanstätten ferrite plate can be predicted with a fair accuracy, as a function of alloy chemistry and temperature by using currently available carbon diffusion-controlled growth rate models for Widmanstätten ferrite [Bhadeshia, 1982; 1985; 1985b]. However, less attention has been given to the nucleation of Widmanstätten ferrite. The following chapter is devoted to the study of some aspects the nucleation of behaviour of Widmanstätten ferrite. The problem is examined theoretically in the context of a displacive transformation mechanism and is assessed against both previously available and new experimental data obtained in the present study.

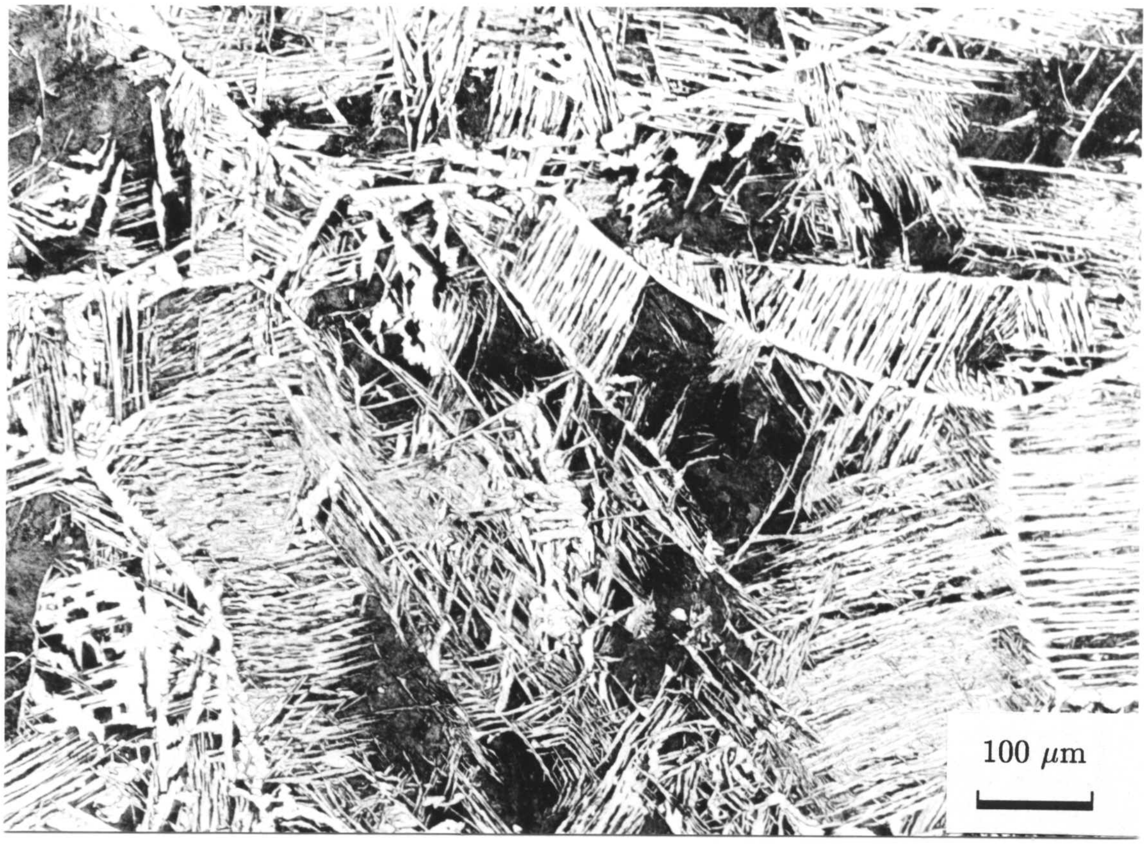

Fig. 8.1: *Micrograph showing Widmanstätten ferrite formed in a Fe-0.4C-2.04Si (wt.%) alloy isothermally transformed at 680 °C for 5* min *after austenitisation at 1300 °C for 30* min. *Note that the parallel formation of Widmanstätten ferrite plates from the grain boundary allotriomorph of ferrite.*

8.2 Nucleation

Nucleation, classically arises because of the net increase in free energy caused by the formation of a small amount of product phase, since the new particle has during the early stages of transformation, a large surface/volume ratio. During the growth stage on the other hand, a negligible amount of the available free energy is dissipated in the creation of new surface.

8.2.1 *Classical Nucleation Theory*

The basis of the classical theory of nucleation originated by Volmer and Weber [1926] and Becker and Döring [1935] is to assume that embryos are internally uniform and have the same structure, composition and properties as the final product phase in bulk form. These assumptions leave the shape and size of the embryo as the only variable parameter. The shape is that which minimizes the free energy of formation. The free energy change during the formation of a nucleus consists of: a) the energy of the interface, b) elastic strain energy due to any volume change, and c) strain energy associated with the lattice distortion produced by partial or complete coherency between two lattices. On the basis of the assumption of isotropy and the absence of strain, the nucleus may be taken to grow from a spherical embryo. Thus the Gibbs free energy for the formation of a spherical embryo of radius r is given by:

$$\Delta G = (\frac{4}{3})\pi r^3 \Delta G^{chem} + 4\pi r^2 \sigma \tag{8.1}$$

and the relationship between ΔG^{chem} and r will have the form shown in Fig. 8.2a. The growth of embryos smaller than the critical radius r^* leads to an increase in the free energy and thus there is a greater tendency for such embryos to shrink rather than grow. Embryos larger than r^* are stable because their growth is accompanied by a decrease in ΔG^{chem}, embryos of radius r^* are unstable having an equal chance of shrinking or growing. Therefore, the condition for the continued growth of an embryo is that the radius should exceed r^*, where $\mathrm{d}\Delta G/dr = 0$ i.e.

$$r^* = \frac{2\sigma}{(-\Delta G^{chem})} \tag{8.2}$$

and the critical free energy, or activation energy barrier for nucleation, is given by

$$\Delta G^* = \frac{16\sigma^3}{3(\Delta G^{chem})^2} \tag{8.3}$$

ΔG^{chem} is strongly temperature-dependent as shown in Fig. 8.2b, so the temperature dependence of r^* and ΔG^* may be assessed in terms of the temperature dependence of ΔG^{chem}. A steady-state nucleation rate N may be defined as the number of stable nuclei produced in a unit time in a unit volume of untransformed solid, and N is proportional to $exp(-\frac{\Delta G^*}{RT})$. The rate at which individual nuclei grow will also be dependent on the frequency with which atoms adjacent to the nucleus can join it and this will be proportional to $exp(-\frac{\Delta G_d^*}{RT})$, where ΔG_d^* is the free energy of activation for diffusion. One may therefore write a simplified representation of the rate of nucleation of a precipitate as:

$$N \propto exp[-(\frac{k\sigma^3}{|\Delta G^{chem}|^2} + \Delta G_d^*)/RT] \tag{8.4}$$

where k is a geometrical constant. It follows that

$$N \propto \nu \ exp(-\frac{\Delta G^*}{RT}) \tag{8.5}$$

where ν is pre-exponential attempt frequency factor and ΔG^* is an effective activation energy.

8.2.2 *Isothermal Nucleation of Martensite*

Theories of martensitic nucleation designed to account for the observed transformation kinetics, are largely concerned with initial growth of an existing martensitic embryo, which nucleated by faulting, from a group of existing dislocations [Olson and Cohen, 1976]. The fault energy γ per unit area associated with such embryo, n atomic planes in thickness, can be expressed as:

$$\gamma = n\rho_A(\Delta G^{chem} + E^{str}) + 2\sigma n \tag{8.6}$$

Where ρ_A is the density of atoms in a close-packed plane, in moles per unit area, ΔG^{chem} and E^{str} are parent/product chemical free energy difference and coherency strain energy respectively, expressed as molar quantities, and σ_n is the particle/matrix interfacial energy (per unit area). If a stress τ is required to move an array of n dislocations of Burgers vector **b**, then the work done in creating a fault of energy γ is given by:

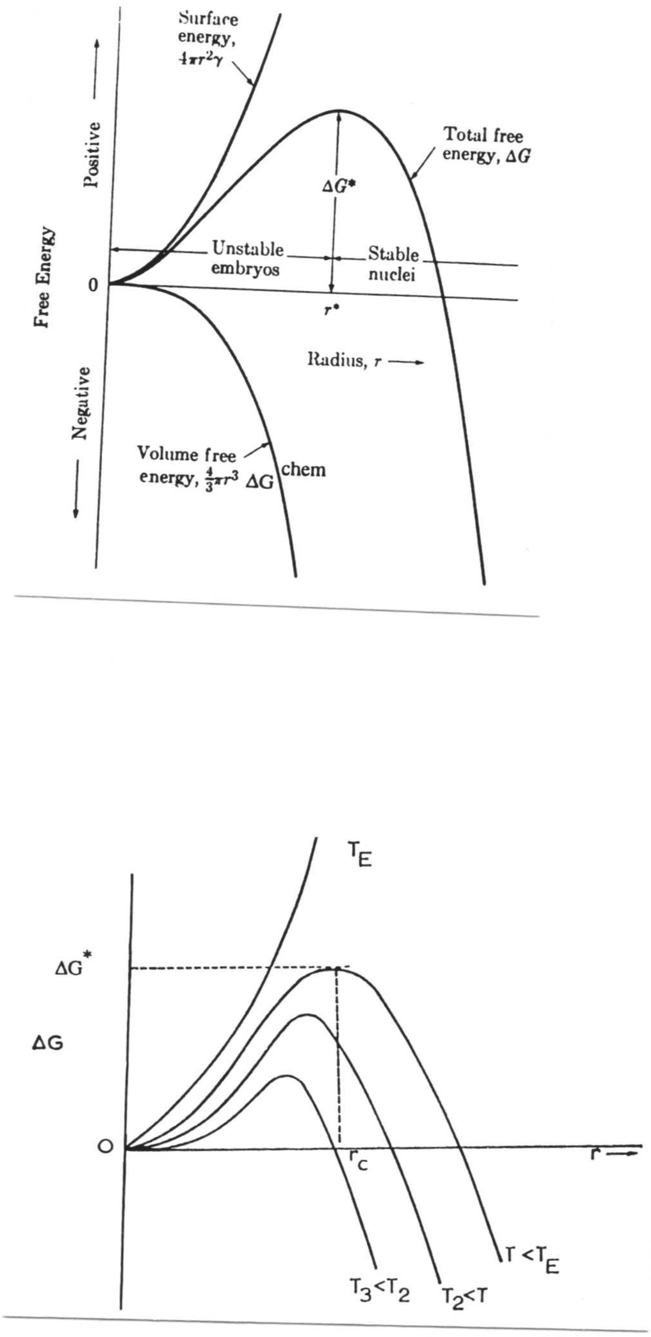
Surface energy, $4\pi r^2\gamma$
Total free energy, ΔG
ΔG^*
Free Energy
Positive
Negative
0
Unstable embryos
Stable nuclei
r^*
Radius, r
Volume free energy, $\frac{4}{3}\pi r^3 \Delta G_{chem}$
(a)
T_E
ΔG^*
ΔG
O
r_c
r
$T < T_E$
$T_3 < T_2$
$T_2 < T$
(b)

Fig. 8.2: (a) Schematic illustration of the relationship between free energy and radius of embryo r. (b) Schematic representation of the temperature dependence of Gibbs free energy [Bruke, 1965].

$$\gamma = -n\tau\mathbf{b} \tag{8.7}$$

In the theory of thermally activated deformation, the activation energy ΔG^* for dislocation motion under an applied stress τ is expressed as [Conrad, 1964; Dorn, 1968]:

$$\Delta G^* = \Delta G^*_o - (\tau - \tau_\mu)V^* \tag{8.8}$$

Where ΔG^*_o is the activation energy in the absence of applied stress, τ_μ is the athermal resistance to dislocation motion, and V^* is the activation volume, as measured from deformation experiments. The expression for isothermal martensitic nucleation can be obtained by substitution of Eqs. 8.6 and 8.7 into Eq. 8.8:

$$\Delta G^* = \Delta G^*_o + [\tau_\mu + (\frac{\rho_A}{\mathbf{b}})E^{str} + \frac{2\sigma}{n\mathbf{b}}]V^* + [(\frac{\rho_A}{\mathbf{b}})V^*]\Delta G^{chem} \tag{8.9}$$

According to Eq. 8.9, the activation energy for isothermal martensitic nucleation should therefore vary linearly with the chemical driving force if V^* remains constant. As demonstrated by Fig. 8.3, a straight line relationship is found between the activation energy and the driving force for the Fe-Ni-Mn systems [Pati and Cohen, 1971].

8.3 Variation of Driving Force with Temperature

The driving force for the nucleation of a phase varies with temperature. If the driving force is calculated assuming that it gives a certain constant detectable nucleation rate N, irrespective of the steel used, then through the classical nucleation theory (Eq. 8.5):

$$N = \nu\ exp[\frac{-\Delta G^*}{RT}] \tag{8.10}$$

so that

$$\Delta G^* = RTln[\frac{N}{\nu}] \tag{8.11}$$

or

$$-\Delta G^* = \beta T \tag{8.12}$$

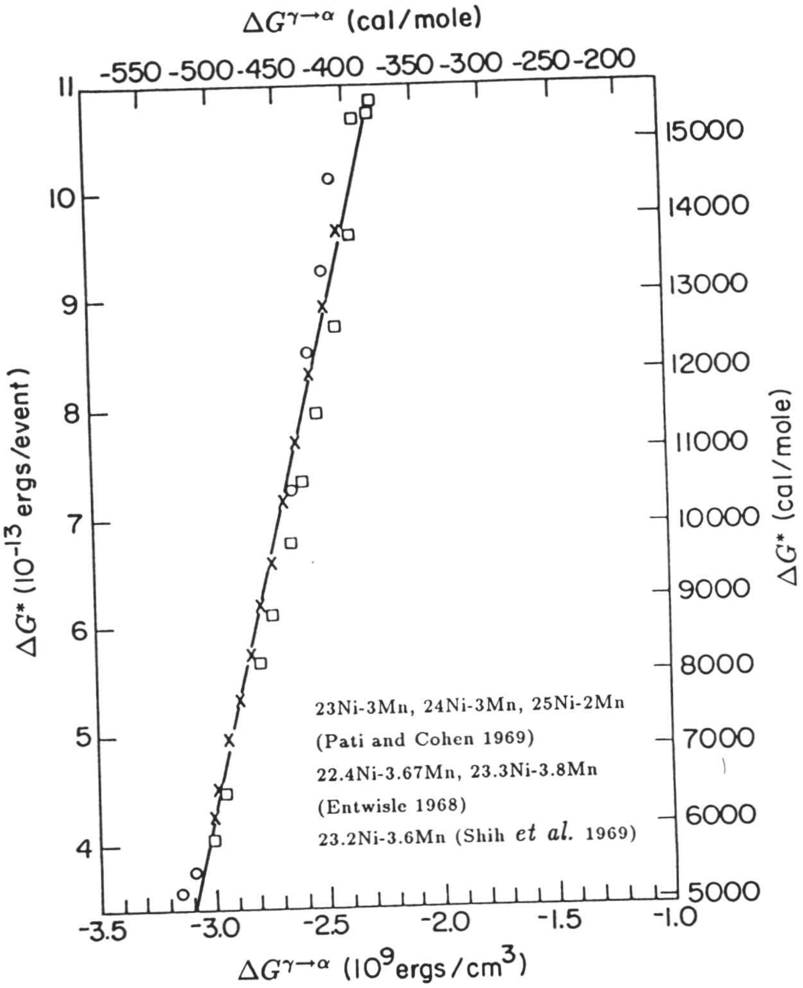

Fig. 8.3: *Variation of activation free energy with the driving force in Fe-Ni-Mn systems [after Pati and Cohen, 1971].*

where ν is pre-exponential attempt frequency factor, R is the gas constant and $\beta = Rln[\frac{N}{\nu}]$.

It follows that β is a constant, since N is a constant irrespective of the steels used. β is expected to be negative, since the nucleation rate should always be less than the attempt frequency.

Now according to the theory of isothermal nucleation of martensite, a linear dependence of activation energy on the chemical driving force [Magee, 1970, Raghavan and Cohen, 1971, Olson and Cohen, 1976]:

$$\Delta G^* = \lambda_1 \Delta G_{Bs}^{\gamma \rightarrow \gamma' + \alpha} + \lambda_1 E^{str} + \lambda_2 \sigma + \lambda_3 \tag{8.13}$$

where
$\lambda_1 = (\rho_A/\mathbf{b})V^*$; $\lambda_2 = (2V^*/(n\mathbf{b})$; $\lambda_3 = \Delta G_o^* + \tau\mu V^*$, and $\Delta G_{Bs}^{\gamma \rightarrow \gamma' + \alpha} = \Delta G^{chem}$.
where $\lambda_1 \rightarrow \lambda_3$ are constants characteristic of the lattice and of the nucleus, E^{str} is the strain energy per unit volume of the nucleus and σ is the interfacial energy per unit area. According to Eq. 8.13 a linear dependence of activation free energy on temperature *i.e.*, $-|\Delta G_{Bs}^{\gamma \rightarrow \gamma' + \alpha}| \propto T$ is expected if the reaction followed the isothermal martensitic nucleation kinetics.

8.4 Nucleation of Widmanstätten Ferrite and Bainite

It is unlikely that the nucleation of Widmanstätten ferrite and bainite can be described in terms of classical nucleation theory, since it appears that the activation energy for its nucleation is a linear function of the transformation temperature [Bhadeshia, 1981]. This behaviour can be explained using the theory of isothermal martensitic nucleation. The thermodynamics of bainite nucleation are not established beyond doubt, but evidence suggests that the formation of a nucleus involves the diffusion of carbon, so that the nucleus that forms has the composition giving the maximum free energy change on formation from austenite. This was established by an analysis of time-temperature-transformation (TTT) diagrams of low alloy steels [Bhadeshia, 1982].

8.4.1 *The Driving Force for the Nucleation*

The change in free energy during the austenite/ferrite (γ /α) phase transformation is shown schematically in Fig. 8.5. The free energy required for the nucleation of ferrite can be obtained by constructing parallel tangents. The parallel tangent construction is consistent with the formation of a nucleus whose composition is such that the maximum value of G_{max} is obtained [Hillert, 1953], hence this probably represents the most likely composition of the nucleus, although such a criterion does not exclude the formation of nucleus of other compositions. The use of the nucleus composition corresponding to the maximum G_{max} should be a good approximation for steels, since the solubility of carbon in ferrite is so limited that any carbon concentration upto the equilibrium level makes negligible difference to the magnitude of G_{max} . Numerical values of G_{max} can be obtained by solving the following equations simultaneously [Bhadeshia, 1982]:

$$G_{Fe}^{\gamma\rightarrow\alpha} + RTln[\frac{a_{Fe}^{\alpha}(1-x_{\alpha}^{\alpha\gamma})}{a_{Fe}^{\gamma}(1-x_{\gamma}^{\gamma\alpha})}] - RTln[\frac{a_{c}^{\alpha}(x_{\alpha}^{\alpha\gamma})}{a_{c}^{\gamma}(x_{\gamma}^{\gamma\alpha})}] = 0 \tag{8.14}$$

$$G_{max} = RTln[\frac{a_{c}^{\alpha}(x_{max})}{a_{c}^{\gamma}(\overline{x})}] = 0 \tag{8.15}$$

where $a_{Fe}^{\alpha}(1-x)$ refers to the activity of iron in ferrite evaluated at the concentration $(1-x)$, and a similar rationale applies to the other activity terms. The term $G_{Fe}^{\gamma\rightarrow\alpha}$ refers to the free energy change accompanying the $\gamma \rightarrow \alpha$ transformation in pure iron and R is the gas constant. The term $\overline{x}$ is the average carbon concentration of the steel concerned and x_{max} represents the composition of ferrite which satisfies equation 8.14.

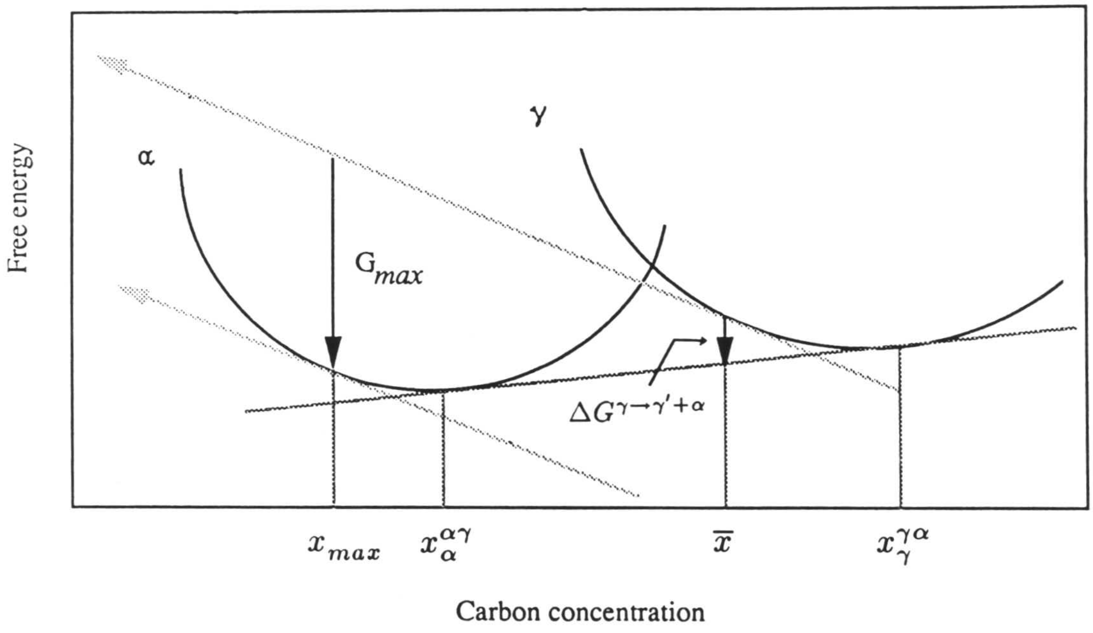
Free energy
α
γ
G_{max}
$\Delta G^{\gamma\rightarrow\gamma'+\alpha}$
x_{max}
$x_{\alpha}^{\alpha\gamma}$
$\overline{x}$
$x_{\gamma}^{\gamma\alpha}$
Carbon concentration

Fig. 8.4: Schematic diagram illustrating the driving forces required for the nucleation (G_{max}) and growth ($\Delta G^{\gamma\rightarrow\gamma'+\alpha}$) of Widmanstätten ferrite from austenite.

8.5 Determination of the Energy Function

Bhadeshia [1981] has demonstrated that the nucleus for Widmanstätten ferrite and bainite is identical, even though the respective growth mechanisms differ. The activation energy for nucleation varies directly with the driving force, consistent with a displacive nucleation mechanism. The redistribution of carbon is a thermodynamic necessity during the nucleation process for Widmanstätten ferrite of bainite. Using this assumption, a method has been developed which gives an indication of the amount of free energy necessary in order to ensure a detectable nucleation rate for the Widmanstätten ferrite and bainite transformations.

It is well known that in low-alloy steels a pronounced bay appears in the time-temperature-transformation (TTT) diagram. This bay is taken to correspond with the interpretation of two 'C'-curves, used for reconstructive and other displacive reactions. The top of the lower C curve is usually identified with the bainite-start (B_S) temperature, although it could correspond to the onset of Widmanstätten ferrite transformation. Hence, the upper part of the displacive C curve temperature is that at which ferrite first forms with an IPS shape change. This is confirmed by detailed studies of Fe-Mn-Si-C steels [Bhadeshia and Edmonds, 1979].

The experimental data of BISRA [1956a] were chosen for analysis because this is one of the more meticulously determined sets of TTT curves. The list of steels utilized in this investigation is given in Table 8.1. These data were used to calculate the free energies available during nucleation under two circumstances:

a) under the assumption that the ferrite nucleates with the parent austenite carbon content.

b) that there is partitioning of carbon during nucleation.

Since the existence of two separable C curves is the basis of the analysis, only those TTT diagrams [BISRA, 1956b] whose component curves could be readily distinguished were used initially although the results were subsequently applied indiscriminately.

8.5.1 *Details of the Thermodynamic Calculations*

The thermodynamic methods used are based on the Lacher [1973] and Fowler and Guggenheim [1939] formalisms, as first applied to steels by Aaronson *et al.* [1966a, b] This work was later corrected and reassesed by Shiflet *et al.* [1973], whose derivations are used throughout the present work but with following modifications:

- *To* equations modified by Bhadeshia [1981b] in order to allow for the high level of carbon in the supersaturated ferrite, and to take account for Zener ordering.

- Partial molar enthalpies $\Delta\overline{H}_\gamma$ and excess partial molar entropy $\Delta\overline{S}_\gamma$ of solution of carbon in austenite are taken to be functions of carbon content. The temperature dependence [Lobo and Geiger, 1976a; 1976b] of $\Delta\overline{H}_\alpha$ and $\Delta\overline{S}_\alpha$ is also taken into account.

Other thermodynamic data needed for the calculations are listed in references. [Bhadeshia, 1981b, Bhadeshia, 1980, Kaufman and Clougherly, 1963]. The Zener ordering energies were calculated as in references. [Fisher, 1949, Zener, 1946]. A FORTRAN IV computer program due to Bhadeshia [1981], capable of doing all the necessary calculations (with the input of steel composition) was utilised in the present analysis.

8.6 Results and Discussion

8.6.1 *Energy Functions*

The results of the analysis of experimental data of BISRA [1956b] are plotted in Fig. 8.5 and Fig. 8.6, from which it seems that the formation of a nucleus with the equilibrium carbon content is the true circumstance; the alternative hypothesis would lead to nucleation against a positive driving force for a few of the steels examined. Intuitively, the formation of a nucleus with an equilibrium carbon content seems more reasonable (irrespective of the carbon content of the ferrite at the growth stage) if it is considered that the thermally activated development of an embryo to the critical nucleus size occurs through a large number of small scale fluctuations, rather than a sudden large fluctuation. Under these circumstances the rejection of few carbon atoms that would be expected within the critical nucleus volume should be readily feasible.

8.6.2 *Further Analysis of the Thermodynamic Data*

In order to check the hypothesis that the nucleation of Widmanstätten ferrite and bainite is similar, it was decided to carry out a further analysis of the published experimental data [BISRA, 1956b], following the same method as described in the preceding section except now taking into account of the stored energy of Widmanstätten ferrite or bainite.

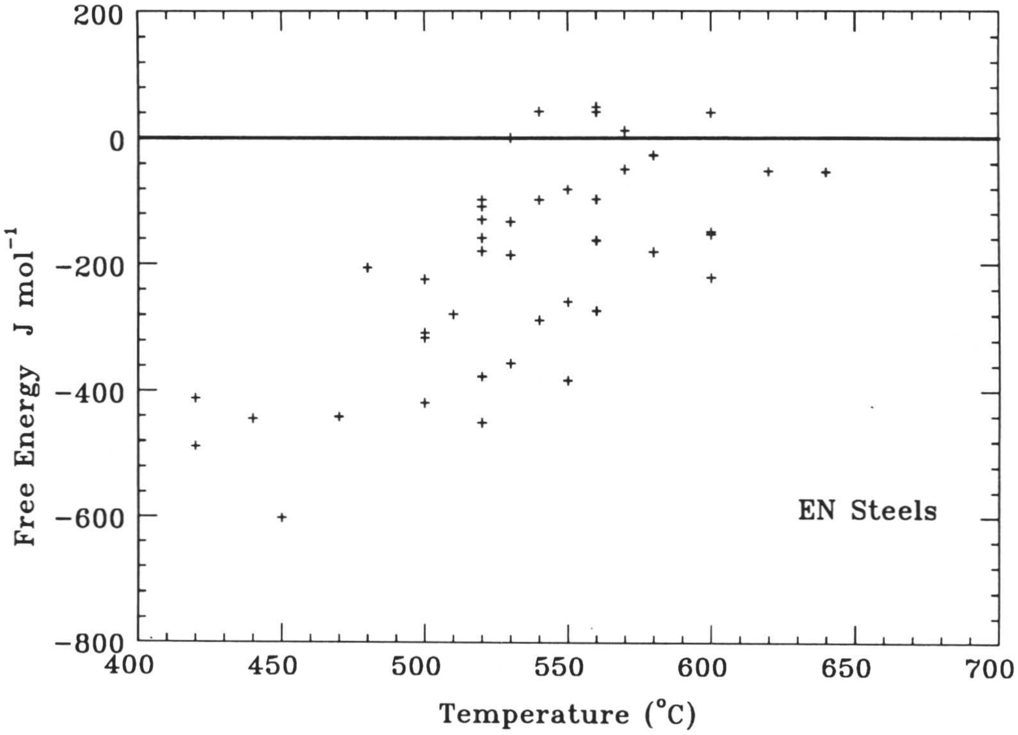

(a)

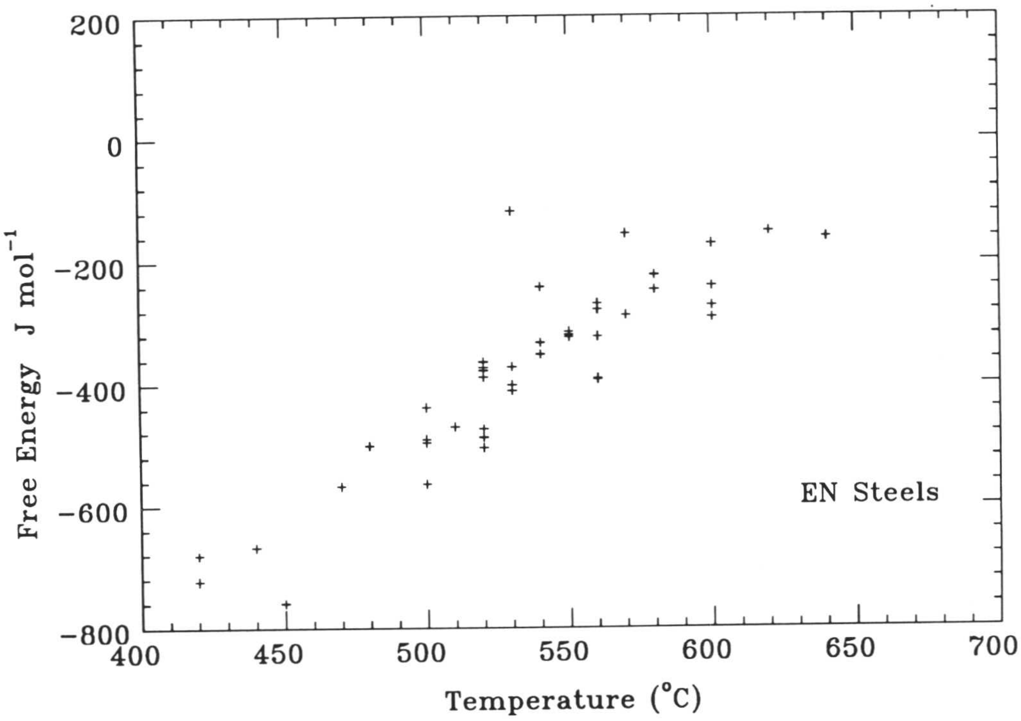

(b)

Fig. 8.5: *Curves representing the free energy change necessary in order to obtain a detectable growth rate of ferrite. (a) The case when the free energy change is calculated on the basis that ferrite inherits the parent austenite carbon content. (b) When the ferrite forms with the equilibrium or para-equilibrium carbon content.*

Table 8.1: *List of chemical compositions of steels, and calculated free energy data.*

No	Steels	B_S	G_{max}	$G^{\gamma\rightarrow\alpha_s}$	Chemical Composition (wt.%)								
		°C	J mol^{-1}	J mol^{-1}									
					C	Si	Mn	Ni	Mo	Cr	others	Ac3	Ac3'
1	En-13	600	-348	-128	0.19	0.14	1.37	0.56	0.39	0.21	-	793	774
2	En-16	580	-421	-27	0.33	0.18	1.48	0.26	0.27	0.16	-	770	749
3	En-17	550	-562	-18.	0.38	0.25	1.49	0.24	0.41	0.14	-	764	740
4	En-18	560	-548	41	0.48	0.25	0.86	0.18	0.04	0.98	-	753	734
5	En-18	560	-581	-97	0.39	0.16	0.89	0.25	0.00	0.88	-	764	747
6	En-19	540	-626	-98	0.41	0.31	0.64	0.81	0.30	1.24	-	760	740
7	En-19	570	-546	-49	0.41	0.23	0.67	0.21	0.23	1.01	-	768	753
8	En-22	540	-471	42	0.40	0.26	0.62	3.45	0.10	0.28	-	720	700
9	En-23	500	-687	-224	0.33	0.23	0.57	3.26	0.09	0.85	-		
10	En-23	520	-596	-154	0.32	0.28	0.61	3.22	0.22	0.63	-		
11	En-24	530	-634	-133	0.38	0.20	0.69	1.58	0.26	0.95	-	749	725
12	En-24	530	-662	-186	0.36	0.22	0.52	1.52	0.27	1.17	-		
13	En-25	510	-726	-279	0.32	0.27	0.56	2.37	0.51	0.74	-		
14	En-25	500	-754	-308	0.31	0.20	0.62	2.63	0.58	0.64	-		
15	En-26	520	-642	-130	0.38	0.15	0.56	2.42	0.46	0.74	-	737	710
16	En-26	480	-823	-206	0.42	0.31	0.67	2.53	0.48	0.72	-	732	700
17	En-28	440	-946	-444	0.32	0.19	0.51	3.02	0.48	1.37	0.18V		
18	En-28	470	-818	-441	0.25	0.15	0.52	3.33	0.65	1.14	0.16V		
19	En-30A	420	-979	-412	0.35	0.14	0.44	4.23	0.13	1.43	-		
20	En-30B	420	-1007	-488	0.32	0.29	0.47	4.13	0.30	1.21	-		

Table 8.1: *Continued ....*

No	Steels	B_S	G_{max}	$G^{\gamma\rightarrow\alpha_s}$	Chemical Composition (wt.%)								
		°C	J mol^{-1}	J mol^{-1}	C	Si	Mn	Ni	Mo	Cr	others		
21	En-40B	450	-1007	-602	0.26	0.21	0.55	0.25	0.54	3.34	-	785	770
22	En-47	560	-575	49	0.51	0.27	0.72	0.15	0.05	0.94	-	752.4	734
23	En-100	520	-640	-109	0.40	0.21	1.32	1.03	0.22	0.53	-	745	715
24	En-110	520	-704	-180	0.39	0.23	0.26	1.44	0.18	1.11	-	757	741
25	En-110	520	-686	-98	0.44	0.23	0.58	1.40	0.11	1.26	-	743	720
26	En-35	640	-308	-53	0.24	0.17	0.42	1.84	0.20	0.18	-	779	762
27	En-36	550	-444	-259	0.14	0.19	0.46	3.55	0.12	1.11	-	760	724
28	En-36	580-	-362	-181	0.15	0.25	0.41	3.02	0.15	0.90	-		
29	En-38	550	-425	-383	0.11	0.21	0.31	5.04	0.30	0.13	-		
30	En-38B	500	-633	-419	0.15	0.21	0.38	4.33	0.17	1.16	-		
31	En-320	520	-644	-450	0.14	0.22	0.50	2.13	0.18	2.00	-	779	756
32	En-354	530	-620	-356	0.19	0.21	0.90	1.87	0.81	1.08	-	776	749
33	En-31	530	-466	000	1.08	0.25	0.53	0.33	0.06	1.46	-		
34	En-39A	540	-435	-288	0.11	0.09	0.38	4.15	0.07	1.33	-		
35	En-355	520	-655	-377	0.20	0.23	0.61	2.00	0.19	1.65	-		
36	En-14	560	-525	-163	0.29	0.26	1.27	0.21	0.04	0.12	-		
37	En-21	570	-320	11	0.33	0.23	0.74	3.47	0.00	0.07	-		
38	En-111	600	-360	40	0.35	0.13	0.65	1.27	0.00	0.55	-		
39	En-325	620	-237	-52	0.20	0.11	0.53	1.75	0.25	0.50	-		
40	En-352	600	-384	-153	0.20	0.15	0.71	1.13	0.05	0.80	-		
41	En-353	560	-500	-273	0.18	0.26	0.73	1.34	0.11	1.11	-		
42	En-20	600	-461	-149	0.27	0.13	0.60	0.19	0.55	0.74	-		
43	En-20	500	-891	-316	0.41	0.23	0.58	0.15	0.74	1.39	-		

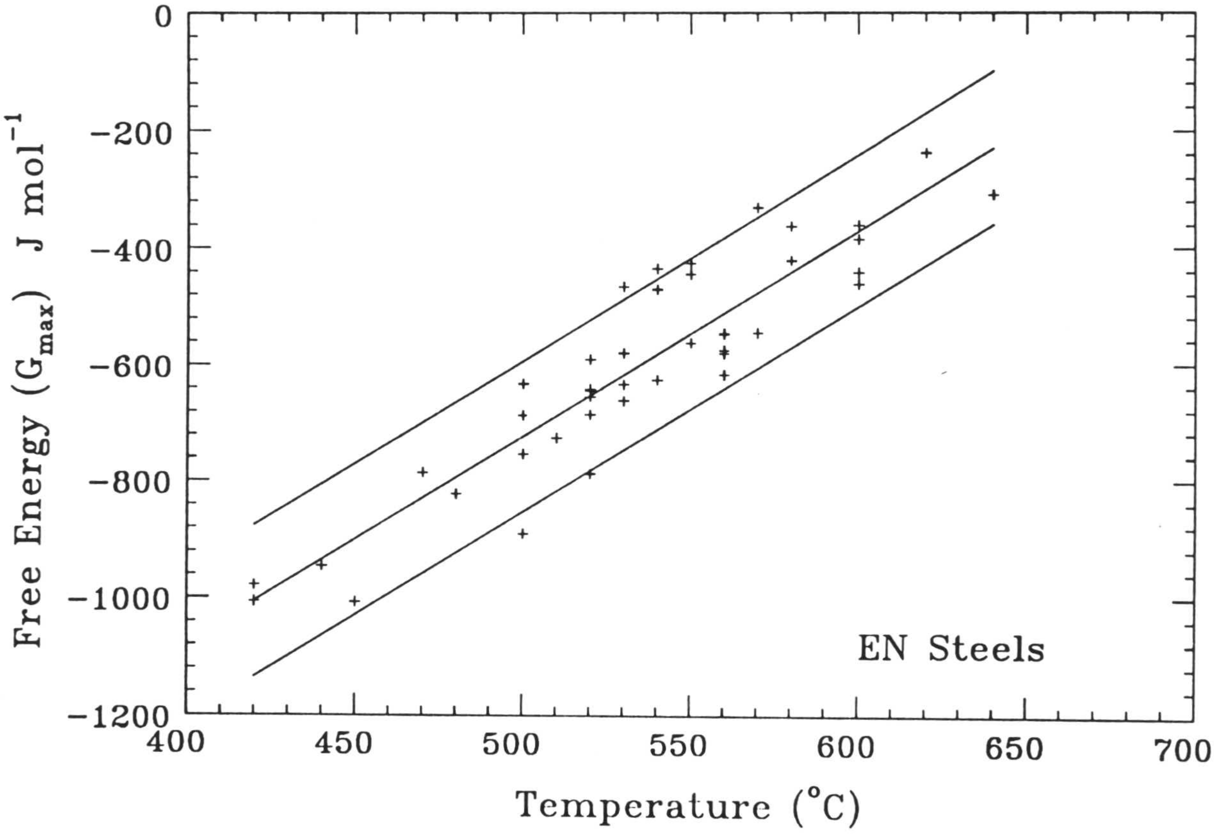

Fig. 8.6: The change in maximum free energy (G_{max}) required for a detectable nucleation rate of ferrite.

If the driving force is sufficient to allow diffusionless transformation and to accommodate some 400 J mol^{-1} of stored energy then the nucleus grows into bainite otherwise Widmanstätten ferrite forms.

Here our purpose is to test whether it is the same nucleus that develops into α_W or α_b, depending on the available driving force. The Steven and Haynes data have been classified, by calculation of available free energy at the highest temperature of the displacive C curve, into steels where top part of the C curve corresponds to α_W and those where it corresponds to α_b. Table 8.2 shows this classification respectively. Fig. 8.7 is a plot of driving force G_{max} vs temperature for both types of steels. These two figures almost having straight line configuration. The slope for Fig. 8.7a was calculated as 2.56 ± 0.77 J mol^{-1} °C and for Fig. 8.7b was 2.78 ± 0.44 J mol^{-1} °C. The slope of both the curves is within experimental error, the same. These results confirm the previous conclusion that bainite and Widmanstätten ferrite grow from the same nucleus, which has an equilibrium carbon content [Bhadeshia, 1981]. It is possible for the nucleus, can develop into either α_W or bainite, depending on the driving force available for growth. The free energy available for growth is expected to be enhanced beyond the critical size due to the decreasing contribution of interfacial energy per unit volume, with increasing size.

8.6.3 *Applications of G_N Curves*

Prediction of microstructure is of importance to industry and G_N curves can be used for example (a) to determine the transition from Widmanstätten ferrite to bainite and (b) to determine the temperature at which Widmanstätten ferrite first formed in a detectable quantity or (c) to predict whether in the steel concerned Widmanstätten ferrite will form or not.

8.6.3.1 Transition from Widmanstätten Ferrite to Bainite

The concepts developed earlier may thermodynamically be expressed as follows, supposing

G_1 = Stored energy per mole of Widmanstätten ferrite (α_W)
G_2 = Stored energy per mole of bainite (α_b)

Table 8.2: *Classification of calculated data as Widmanstätten ferrite and bainitic steels (see text).*

(a) *Widmanstätten ferrite steels.*

No.	Steels	B_S ^{o}C	G_{max} J mol^{-1}
1	En-13	600	-348
2	En-16	580	-421
3	En-17	550	-562
4	En-18	560	-548
5	En-18	560	-581
6	En-19	540	-626
7	En-19	570	-546
8	En-22	540	-471
9	En-23	500	-687
10	En-23	520	-596
11	En-24	530	-634
12	En-24	530	-662
13	En-25	510	-726
14	En-25	500	-754
15	En-26	520	-642
16	En-26	480	-823
17	En-47	560	-575
18	En-100	520	-640
19	En-110	520	-704
20	En-110	520	-686
21	En-35	640	-308
22	En-36	550	-444
23	En-36	580	-362
24	En-38	550	-425

Table 8.2: *Continued ....*

No.	Steels	B_S ^{o}C	G_{max} J mol^{-1}
25	En-354	530	-620
26	En-31	530	-466
27	En-355	520	-655
28	En-14	560	-525
29	En-21	570	-320
30	En-111	600	-360
31	En-325	620	-237
32	En-352	600	-384
33	En-353	560	-500
34	En-20	600	-461
35	En-20	500	-891

(b) *Bainitic steels.*

No.	Steels	B_S ^{o}C	G_{max} J mol^{-1}
1	En-28	440	-946
2	En-28	470	-818
3	En-30A	420	-979
4	En-30B	420	-1007
5	En-40B	450	-1007
6	En-38B	500	-633
7	En-320	520	-644

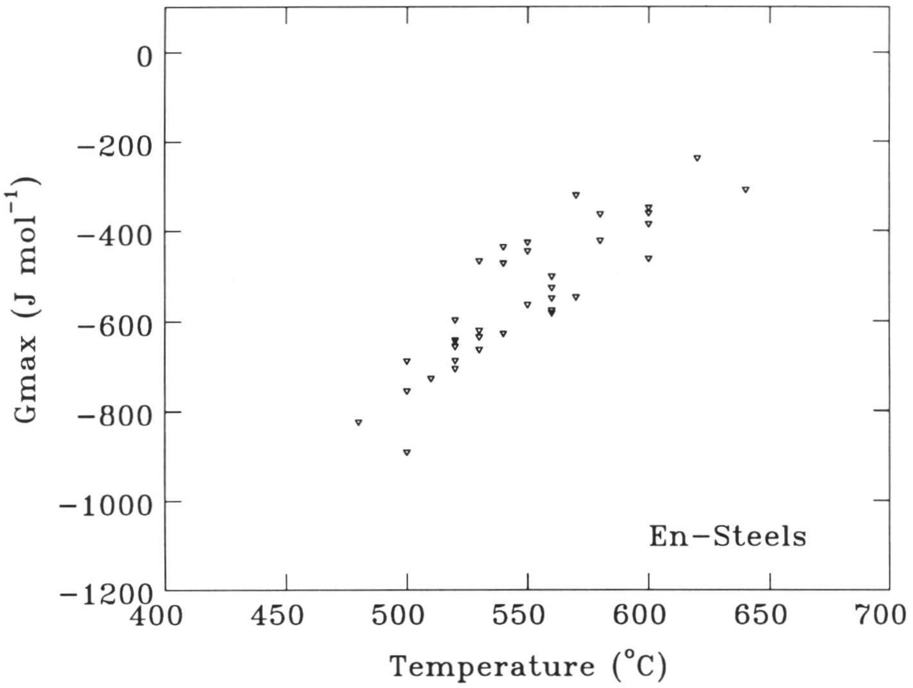

(a)

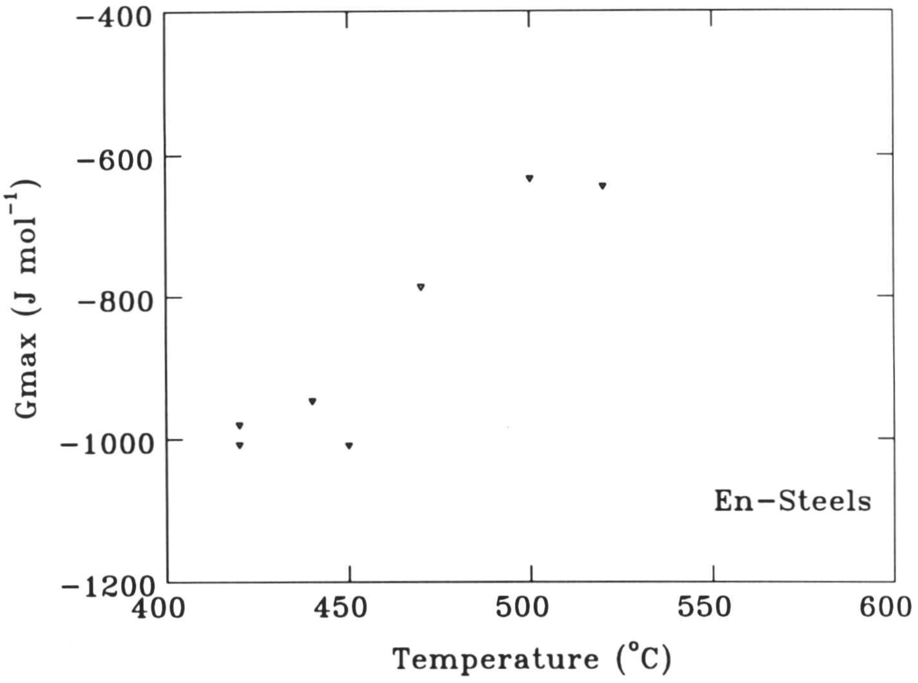

(b)

Fig. 8.7: *Classification of En-Steels [BISRA, 1956b], (a) Widmanstätten ferrite and (b) bainite, on the basis of stored energy (as discussed in section 8.7).*

Widmanstätten ferrite will then form below the Ae_3 temperature when

$$G_{max} > G_1 \tag{8.16}$$

$$G_{max} > G_N \tag{8.17}$$

However, since the driving force necessary for detectable amount of nucleation (i.e. G_N) should always be greater then that necessary to sustain growth, G_N will always exceed G_1 and condition of Eq. 8.16 become redundant.
Bainite will form below the T_o temperature when

$$G_{max} > G_2 \tag{8.18}$$

and

$$G_{max} > G_N \tag{8.19}$$

However, in any steel where the Widmanstätten ferrite transformation precedes bainite formation, condition of Eq. 8.19 will probably be redundant. This is because G_{max} varies approximately linearly and monotonically with temperature, so that once Eq. 8.16, has been satisfied, the further lowering of temperature will not in general lead to violation of Eq. 8.19.

8.6.3.2 Widmanstätten Ferrite Formation

In the study of phase transformations, it is useful to know whether in the steel concerned, the nucleation of Widmanstätten ferrite is possible or not. By using the G_N curve it becomes possible to predict the W_S temperature in any particular steel.

Fig. 8.8 illustrates the two cases, the free energy G_{max} is plotted for a particular steel along with the G_N curve superimposed on it. As just discussed, G_N is the minimum amount of free energy required for the detectable nucleation of Widmanstätten ferrite irrespective of the chemical composition or carbon concentration of any particular steel. This implies that if the G_N curve lies above G_{max} curve than the nucleation of Widmanstätten ferrite is possible in that particular steel at any temperature (Fig. 8.8a). If the G_N curve lies below then there is not enough driving force for the nucleation of Widmanstätten ferrite. This situation is shown schematically in Fig. 8.8b, and the nucleation of Widmanstätten ferrite is only possible at above "A" and below "B" (Fig. 8.8b), but is not possible in between A and B, because there is not enough driving force available for the nucleation.

We have seen in Fig. 8.6 that the maximum free energy term *i.e.,* G_{max} is over a large temperature range linearly proportional to the temperature and this is also justified from the theory of isothermal martensitic nucleation. A detectable nucleation rate should only be possible in any particular steel if the free energy G_{max} for that steel exceeds G_N at the temperature concerned. Therefore, G_N curve of Fig. 8.6 will be assumed to be a universal curve expressing G_N as a function of temperature. This seems justified in view of the nature of the analysis and the wide range of steels accounted for in the calculation.

8.7 Widmanstätten Ferrite Nucleation Kinetics

The results obtained in the preceding sections can be rationalised if it is assumed that the nucleation of Widmanstätten ferrite is similar to that of martensite, *i.e.,* the activation energy ΔG^* for nucleation varies directly with the magnitude of the chemical driving force ΔG, rather than the inverse square relationship implied by classical nucleation theory where $G^* \propto (\Delta G)^{-2}$. In martensite nucleation theory [Magee, 1970], this dependence is interpreted to imply the pre-existence of embryos, which simply need to grow rapidly to give what is in effect operational nucleation, controlled by the mobility of the embryo/matrix interface [Raghavan and Cohen, 1971, Olson and Cohen, 1976]. It is the activation energy for interface motion which is detected experimentally as that for nucleation. The analysis of kinetic data in sections 8.4-8.6, for a large number of steels indicated that due to the lower driving force available at the higher temperatures where Widmanstätten ferrite forms, it is necessary for its nucleation to occur by a paraequilibrium mechanism involving the partitioning of carbon, whereas that of martensite is diffusionless.

The implication of all this is that it becomes more difficult (*i.e.,* requires a larger driving force) to obtain a detectable degree of nucleation as transformation is suppressed to lower temperatures by solute additions, so that the W_S temperature decreases more rapidly than the Ae_3 temperature with change in alloy chemistry. Further more, the free energy G_N necessary to obtain a detectable degree of transformation approximately a linear function of temperature:

$$G_N = A + B(T - 273.18) \tag{8.20}$$

and this is a universal function which can be applied to any low–alloy steel. The values of the constants A and B obtained by multiple regression analysis are given in Table 8.3.

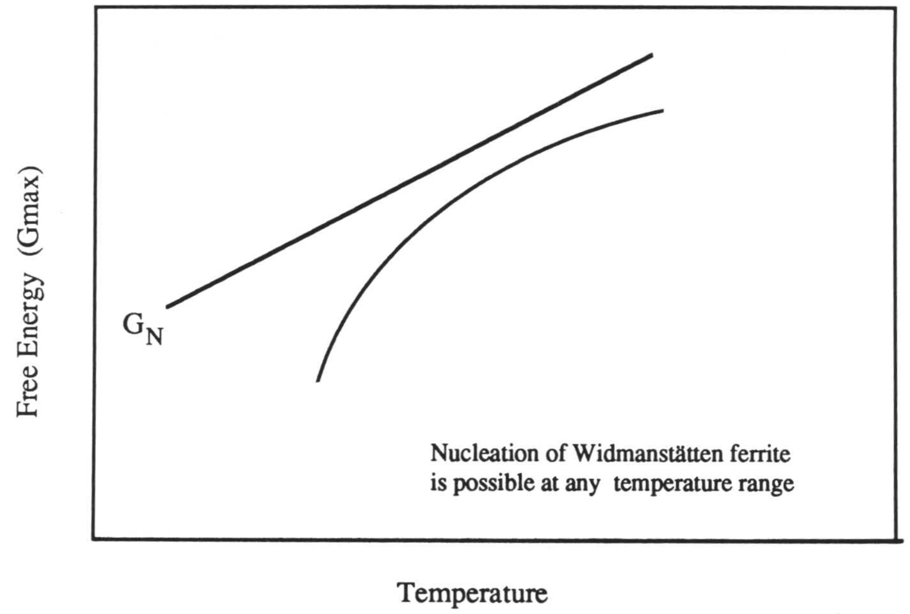
Free Energy (Gmax)
G_N
Nucleation of Widmanstätten ferrite
is possible at any temperature range
Temperature

(a)

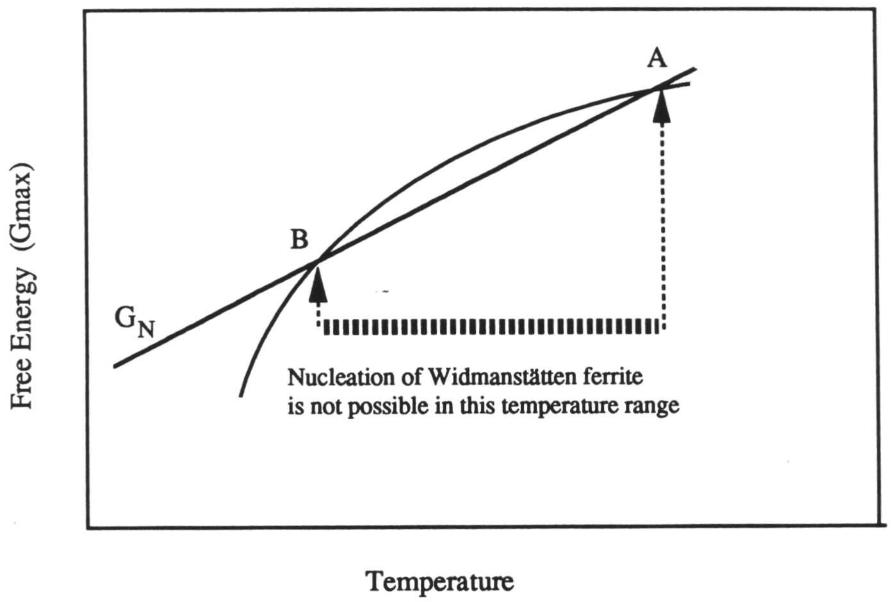
A
B
G_N
Free Energy (Gmax)
Nucleation of Widmanstätten ferrite
is not possible in this temperature range
Temperature

(b)

Fig. 8.8: *Schematic illustration of the significance of G_N curve in determining a detectable nucleation rate of Widmanstätten ferrite. (a) Nucleation is possible at any temperature. (b) Nucleation is not possible at temperatures between A and B.*

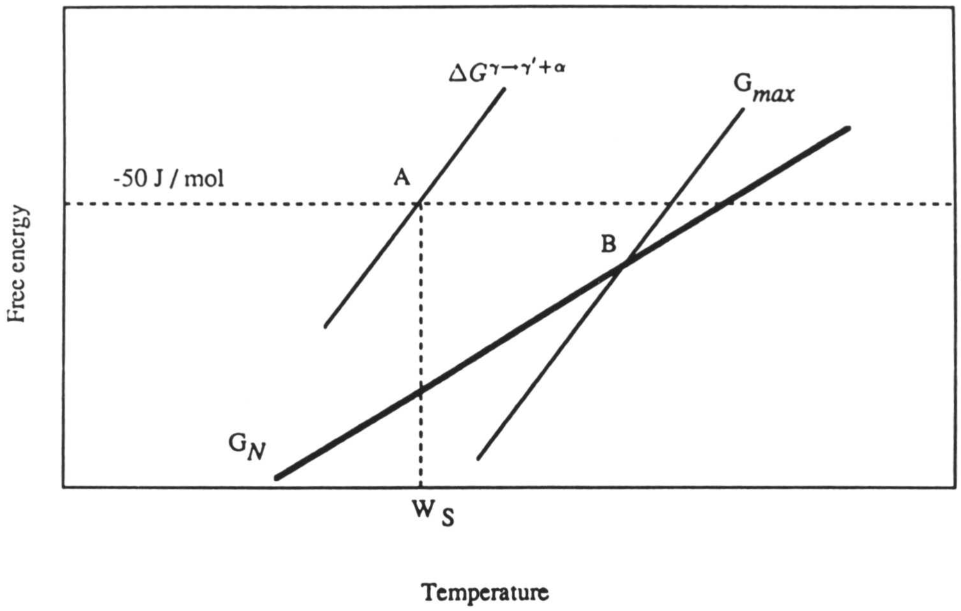

Fig. 8.9: *Schematic illustration of the conditions determining the Widmanstätten-start temperature (W_S). The intersections at A and B determine the temperatures where the growth and nucleation conditions are satisfied. In the example illustrated, it is the growth which limits the W_S temperature.*

The driving force G_{max} that is available for nucleation in any given steel, has to exceed G_N, giving the condition

$$G_{max} \leq G_N. \tag{8.21}$$

where G_{max} as usual represents the maximum free energy change possible during nucleation, assuming that the nucleus adopts the chemical composition consistent with the maximum change in free energy, Fig. 8.5. The second condition that also has to be satisfied is that growth should be thermodynamically possible, so that the free energy change for growth (Fig. 8.4) should exceed the stored energy of Widmanstätten ferrite.

$$\Delta G^{\gamma\rightarrow\gamma'+\alpha} < -50 \text{ Jmol}^{-1} \tag{8.22}$$

It is the simultaneous satisfaction of these two conditions which gives the highest temperature at which a detectable degree of reaction occurs. These concepts are illustrated schematically in Fig. 8.9.

8.8 Analysis of Experimental Data on Widmanstätten Ferrite

The results obtained from the analysis of sections 8.4-8.6, are first applied to the experimental data of the present study and then in the following section to the data found in the published literature.

8.8.1 *Nucleation of Widmanstätten Ferrite in Alloys A3 and W1*

The calculated driving force versus temperature curves are shown in Fig. 8.10, for both alloys. It is evident from Fig. 8.10, that the G_N curve lies above the free energy-temperature curves (G_{max}) of all the alloys and the case is similar to the situation illustrated in Fig. 8.8a. It means that the nucleation of Widmanstätten ferrite over the whole range of temperature, is in principle possible in these alloys. Consistent with this, Fig. 8.11, shows a series of micrographs illustrating the formation of Widmanstätten ferrite in both alloys.

Table 8.3: *The values of the constants A and B in equation* 8.20.

Constants	Values
A	-2489 J mol^{-1}
B	3.531 J mol^{-1} ^{o}C

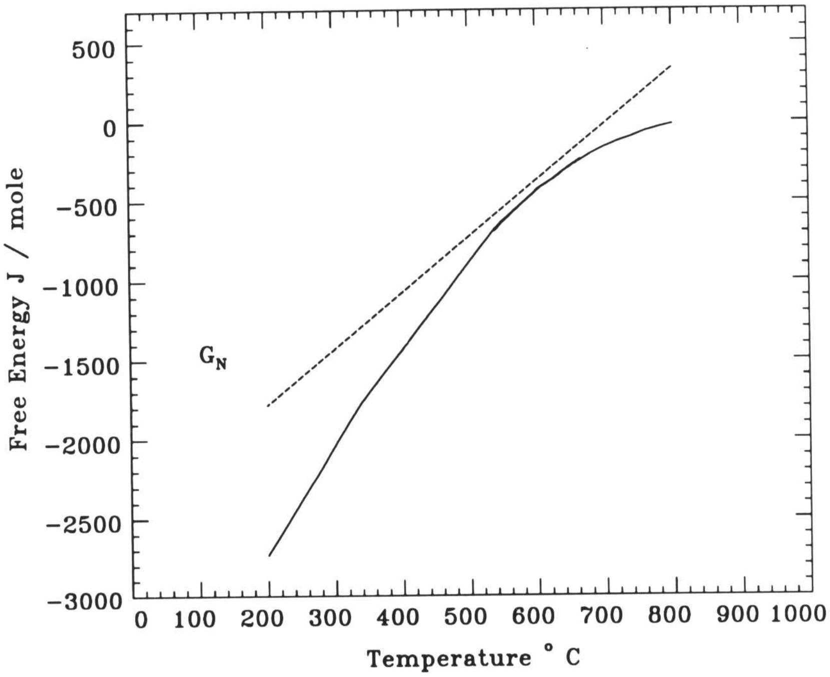

(a)

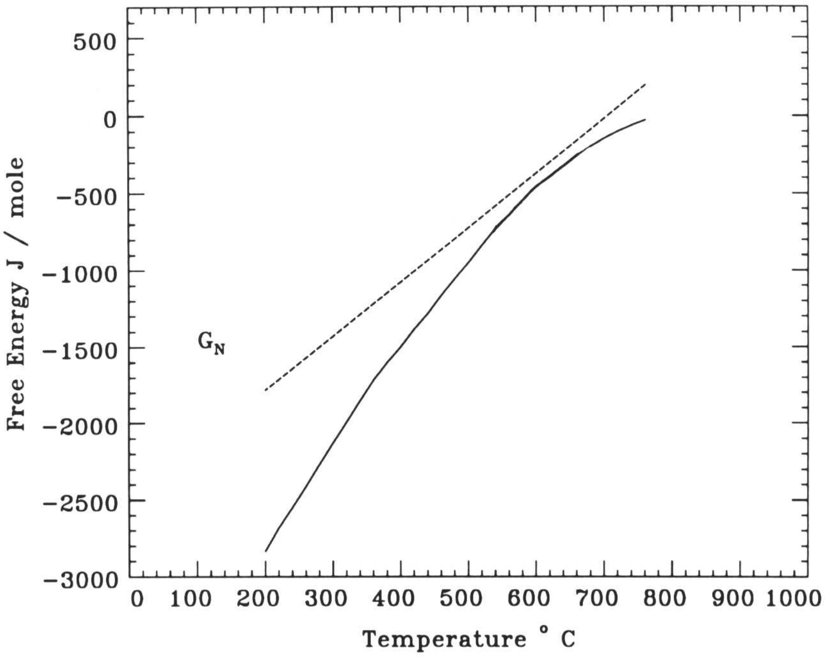

(b)

Fig. 8.10: *Prediction of a detectable nucleation rate possible in (a) A3 and (b) W1 alloys, in these alloys the nucleation of Widmanstätten ferrite is possible at any temperature but Widmanstätten ferrite can only form at the temperature where enough driving force will be available for the growth.*

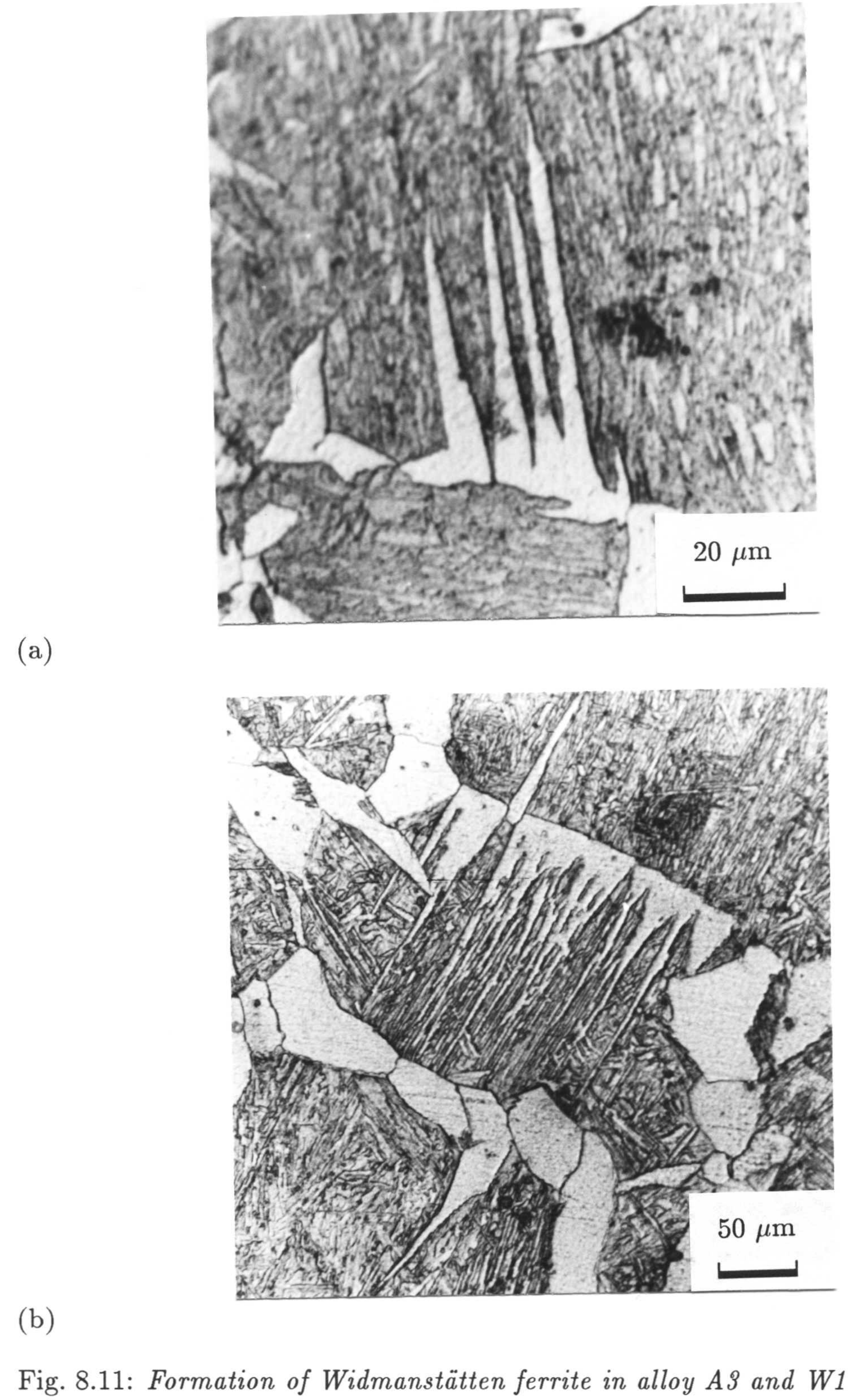

Fig. 8.11: *Formation of Widmanstätten ferrite in alloy A3 and W1 after austenitisation at 1100 °C for 10* min. *(a) Alloy A3, isothermally transformed at 740 °C for 200* s *showing blocky ferrite along with Widmanstätten ferrite plates at the austenite boundaries. (b) Weld deposit W1, ferrite allotriomorphs and Widmanstätten ferrite, the specimen having been transformed for 100* s *at 670 °C.*

8.8.2 *Nucleation of Widmanstätten Ferrite in Alloys A1 And A2*

The driving force versus temperature curves are shown in Fig. 8.12, for these alloys. By inspection of Fig. 8.12, this situation is very similar to that of Fig. 8.8b, it is obvious that there is insufficient driving force for the nucleation of Widmanstätten ferrite in the temperature range 420 to 680 °C. However, there is enough driving force available in the temperature range beyond 680 °C and below 420 °C. Nucleation of Widmanstätten ferrite in those regions should therefore be possible.

The formation of Widmanstätten ferrite in alloys A1 and A2 is shown in Fig. 8.13. In alloy A2 formation of Widmanstätten ferrite was observed at 700 °C, while the predicted lower limit was 680 °C. However, in alloy A1 Widmanstätten ferrite also formed below 675 °C, *i.e.,* in the region where there is apparently insufficient free energy available for the Widmanstätten ferrite nucleation. A close inspection of the microstructure (Fig. 8.13) revealed that a lot of carbide particles has precipitated within the allotriomorphic ferrite, matrix and Widmanstätten ferrite plates. Since carbide precipitation removes carbon from the system during transformation, it causes an increase in the free energy available for nucleation of Widmanstätten ferrite at lower temperatures. This might shift the G_{max} curve further below the G_N curve, making nucleation feasible. The other factor to be considered here is that if we consider the scatter in the data presented for the G_N curve in Fig. 8.6, the difference between calculated and experimentally determined temperature range can easily be reconciled. Hence, the nucleation of Widmanstätten ferrite in alloy A1 at this temperature is approximately consistent with the calculated data. The formation of Widmanstätten ferrite below the 420 °C is possible but due to the higher available driving force at such a low temperature, the bainite transformation takes precedence and replaces the formation of Widmanstätten ferrite.

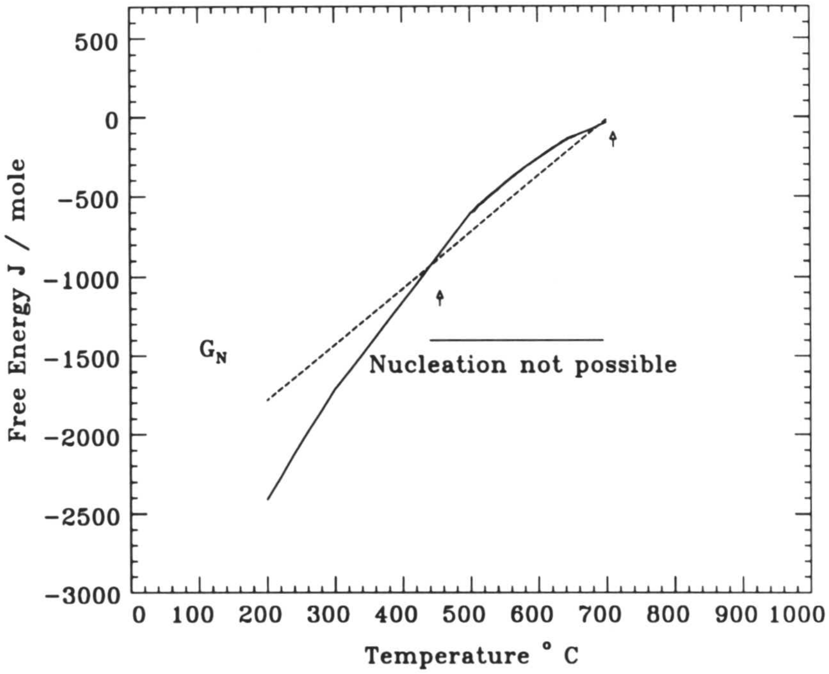

(a)

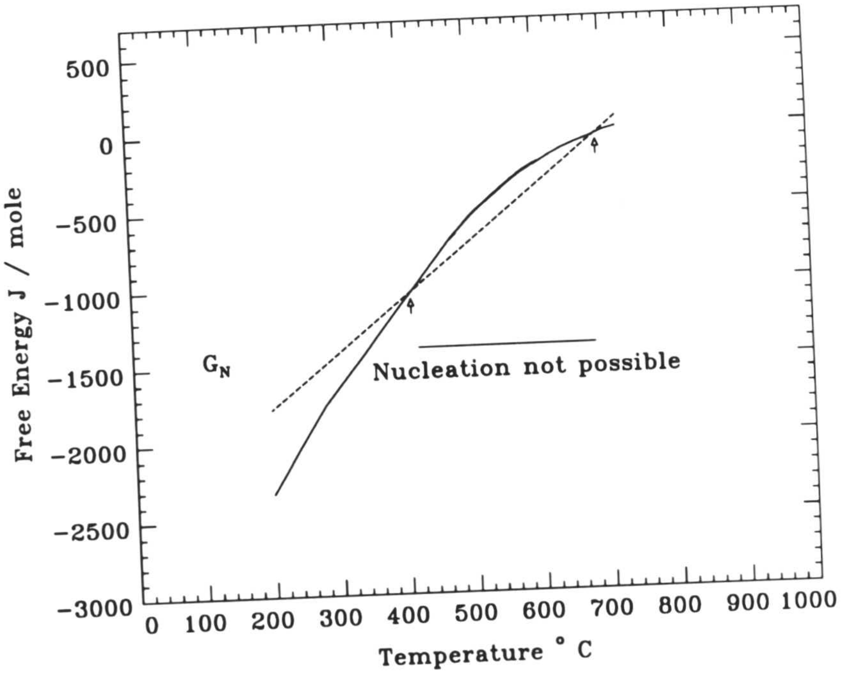

(b)

Fig. 8.12: *Prediction of the temperature range over which Widmanstätten ferrite can form at a detectable rate in alloys (a) A1 and (b) A2.*

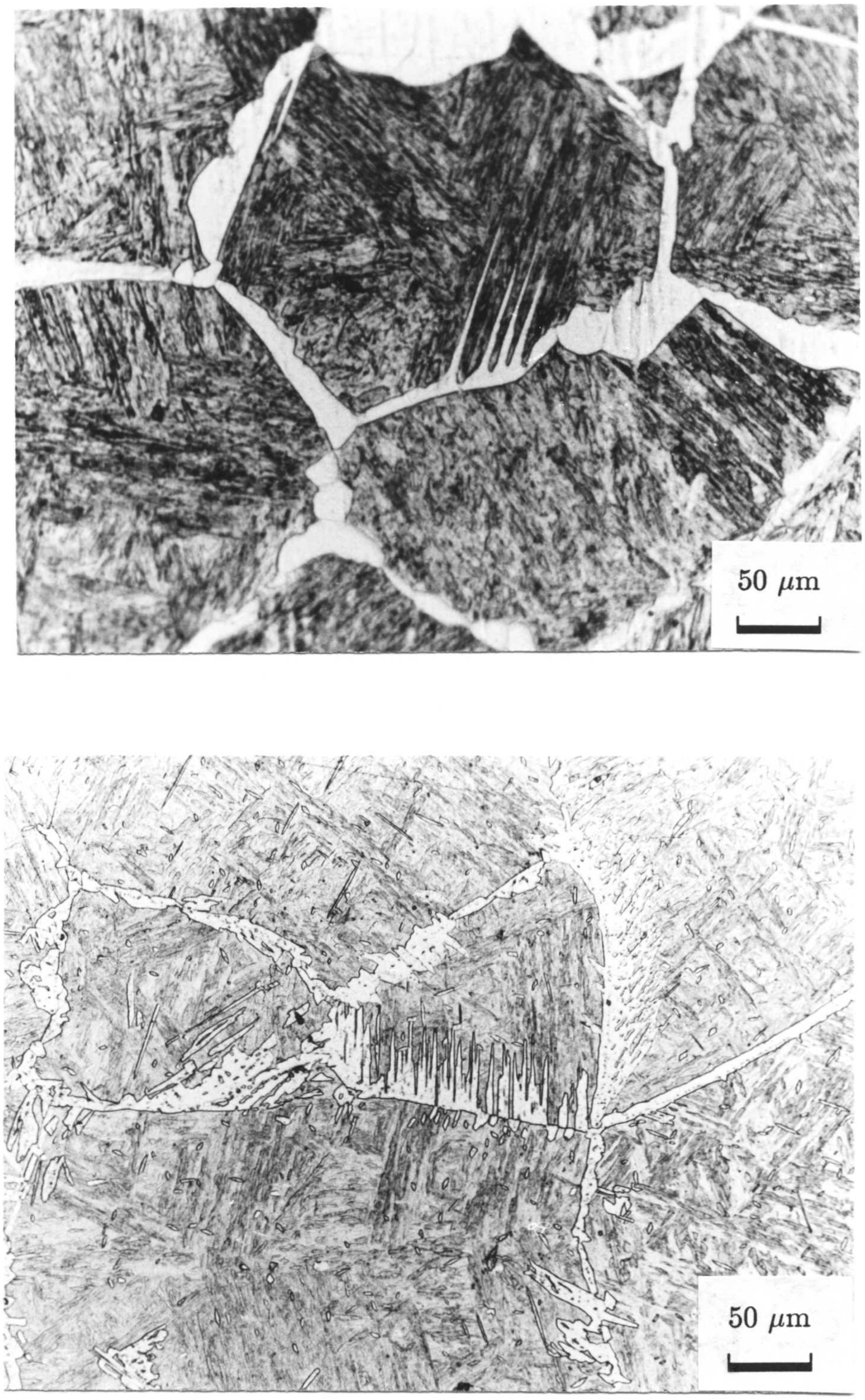

Fig. 8.13: *Optical micrographs showing Widmanstätten ferrite formation in alloys A1 and A2. Both alloys were austenitised at 1100 °C for 10* min. *(a) Alloy A1 after 12 days at 675 °C. b) Alloy A2 after isothermal transformation at 700 °C for 100 hr.*

8.9 Analysis of Published Experimental Data on Widmanstätten Ferrite

The recently published data [Aaronson *et al.* 1986] on the Widmanstätten–start temperature as a function of alloy chemistry, were analysed theoretically. Aaronson *et al.* were originally interpreted the data by considering the transition from allotriomorphic to plate–like ferrite to be determined by changes in the relative proportions of "partially coherent" and "disordered" regions of interface surrounding the ferrite particles. Whatever the details of the model [Aaronson *et al.* 1986], that theory is indeterminate since the proportion was found not to be constant, and could not be predicted as a function of alloy chemistry.

The calculations for majority of the steels studied by Aaronson *et al.* [1986] are presented in Figs. 8.15-8.16. A few of the steels they studied contained substantial amounts of copper, cobalt or aluminium, elements for which thermodynamic data compatible with the Lacher Fowler Guggenheim quasichemical solution model [Fowler and Guggenheim, 1939] used here, are not available. Consequently, those steels are not included in the analysis. Fig. 8.15 confirms that for almost all the steels listed in Table 8.4, W_S temperature is determined by equation 8.20, although for steel-11, which is heavily alloyed with Mn, the W_S temperature is suppressed to a greater extent, when compared with the Ae_3 temperature, as is predicted by the present analysis. It is evident (Fig. 8.15) that there is very good agreement between experiment and theory.

Fig. 8.16 is plot between experimentally determined W_S and Ae_3 temperature, shows that the W_S temperature is much more sensitive to the alloy composition than that of Ae_3 temperature, which lead to the conclusion that in designing new high-strength weld deposits, alloy chemistry plays an important role in determining the extent of the Widmanstätten ferrite reaction.

Table 8.4: *Chemical compositions of the steels used by Aaronson et al. [1986].*

Steel			Chemical Composition (wt.%)							Temperature		
^{o}C												
No.	C	Si	Mn	Cr	Mo	Ni	Al	Co	Cu	$W_{S(e)}$	$W_{S(c)}$	Ae_3
1	0.110	–	–	–	–	–	–	–	–	825	820	857
2	0.096	0.51	–	–	–	–	–	–	–	855	840	897
3	0.120	1.47	–	–	–	–	–	–	–	905	860	957
4	0.089	–	–	–	–	–	–	1.02	–	835	–	872
5	0.140	–	–	–	–	–	–	3.20	–	855	–	872
6	0.098	–	–	–	–	–	0.52	–	–	875	–	932
7	0.270	–	–	–	–	–	1.40	–	–	905	–	957
8	0.096	–	–	–	–	–	–	–	1.02	815	–	842
9	0.120	–	–	–	–	–	–	3.20	2.98	755	–	807
10	0.110	–	1.01	–	–	-	–	—	–	765	780	822
11	0.120	–	3.08	–	–	–	–	–	–	577	680	765
12	0.093	–	–	–	–	1.06	–	–	–	780	780	832
13	0.110	–	–	–	–	3.28	–	–	–	705	700	775
14	0.092	–	–	0.94	–	–	–	–	–	835	820	847
15	0.092	–	–	2.64	–	–	–	–	–	805	800	827
16	0.110	–	–	–	0.90	–	–	–	–	845	840	876
17	0.110	–	–	–	1.95	–	–	–	–	855	860	902

Values of $W_{S(c)}$ are from present work and those of $W_{S(e)}$ are due to Aaronson *et al.* [1986].

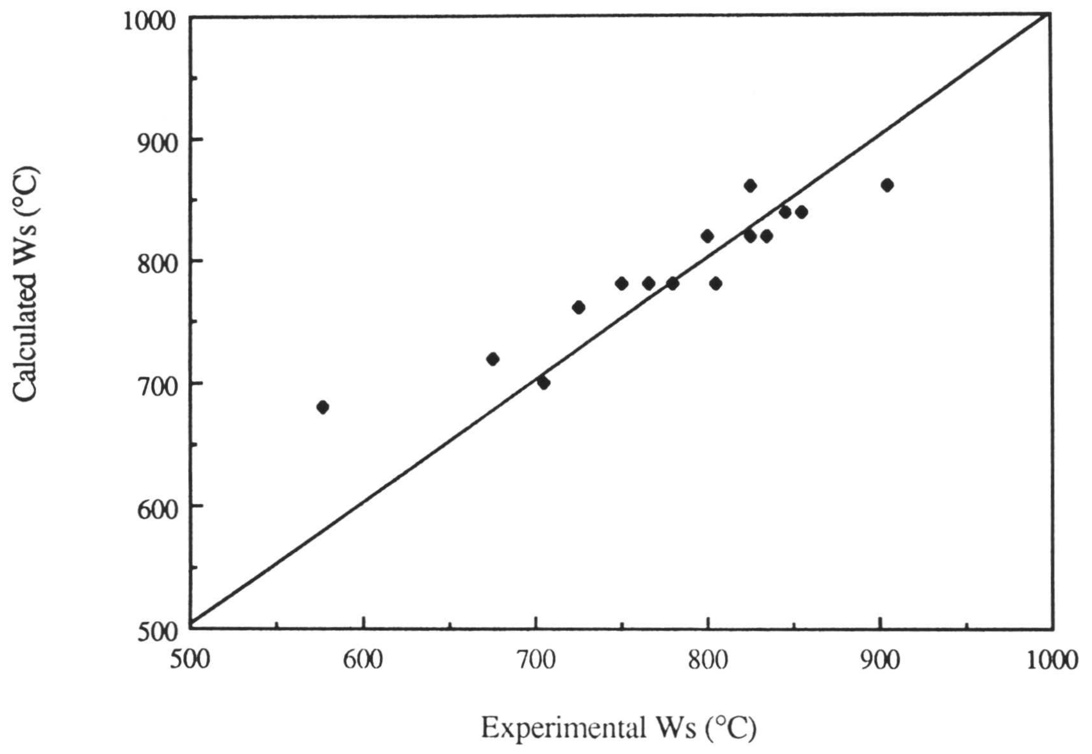

Fig. 8.15: *Comparison of the calculated and experimentally determined [Aaronson et al. 1986] Widmanstätten ferrite-start (W_S) temperatures.*

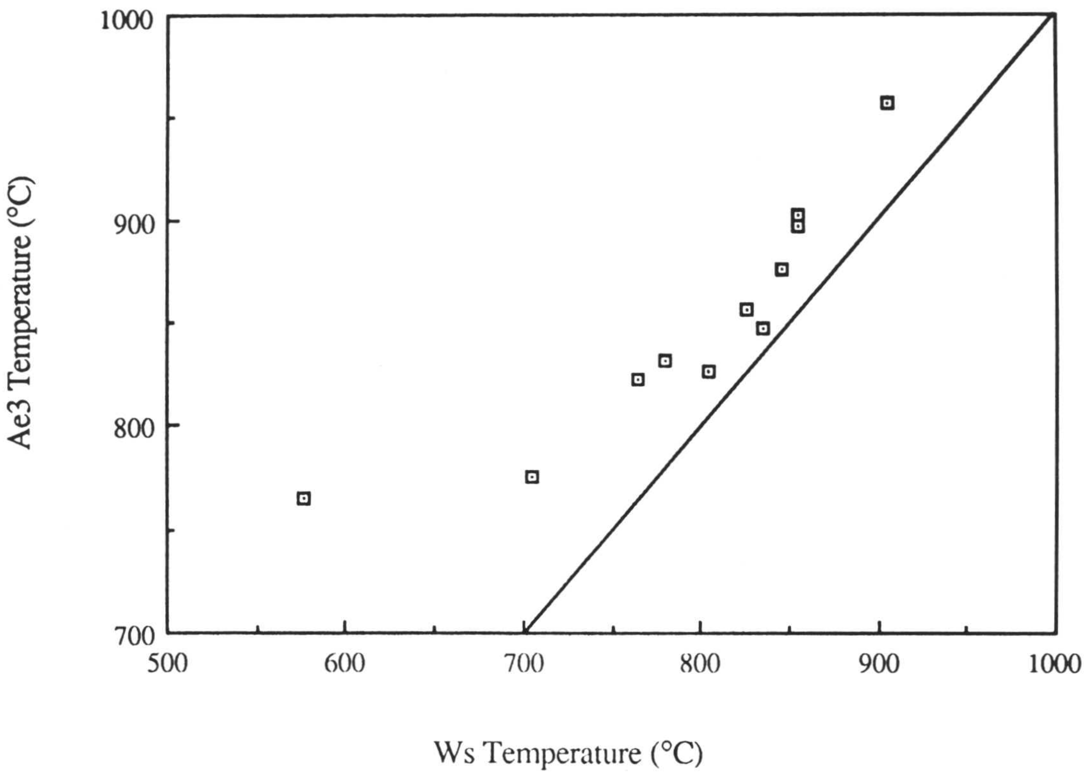

Fig. 8.16: *Plot of experimental (W_S) and Ae_3 temperatures for the steels studied by Aaronson et al. [1986]. The plot shows that the (W_S) temperature is much more sensitive of the alloy chemistry than Ae_3 temperature.*

8.10 Conclusions

the problem of nucleation of Widmanstätten ferrite has studied in detail, both theoretically and experimentally. It is concluded that the nucleation of Widmanstätten ferrite can be best studied if it assumed that it follows the same mechanism as that for isothermal nucleation of martensite of preexisting embryos, but with the diffusion of carbon during nucleation. In this mechanism the free energy change for nucleation is directly proportional to the temperature rather than

$\Delta G^* \propto (\Delta G)^{-2}$ type relation expected by the classical nucleation theory.

The results of thermodynamic analysis have been applied to new experimental data and those data found in the published literature. It was found that the data can be predicted to a fair accuracy.

♣♣♣

Chapter 9

THE GROWTH OF WIDMANSTÄTTEN FERRITE PLATES AND BAINITE SHEAVES

9.1 General Introduction

The final mechanical properties of a weld deposit or a wrought steel depend on a number of variables such as chemical composition, cooling conditions and the process itself, final microstructure. In addition the presence of various transformation products, determines the final microstructure of the weld deposit or the steel, and hence the mechanical properties. For example, it is known that the presence of Widmanstätten ferrite leads to poor toughness [Savage and Aaronson, 1966, Rodrigues and Rogerson, 1977] because of its larger effective grain size and preferred orientation which offers a little resistance to the crack propagation. Bainitic steels, however, show a remarkable combination of toughness and strength [Nakasugi *et al.* 1983] and acicular ferrite is the most desirable phase [Grong and Matlock, 1986] from the toughness point of view. The presence of both Widmanstätten ferrite and bainite directly affect the mechanical properties, and therefore, knowledge about their growth is of commercial as well as academic interest.

9.1.1 *Growth of Widmanstätten Ferrite and Bainite*

A critical assessment of the diffusion-controlled growth of ferrite plates in plain carbon steels indicates that in these steels, plates of Widmanstätten ferrite lengthen at a rate which is approximately consistent with growth controlled by the diffusion of carbon in the austenite ahead of the transformation interface [Bhadeshia, 1985]. The growth of bainite sheaves was on the other hand, found to occur at a rate much faster than expected from carbon diffusion-controlled transformation. These conclusions are consistent with current models for transformations in steels, which assume that Widmanstätten ferrite grows by a displacive para-equilibrium transformation mechanism whereas bainite grows by displacive transformation in the form of sheaves of platelets called subunits. Each subunit inherits the composition of the parent phase and any excess carbon is subsequently partitioned into the residual austenite or precipitated in the form of carbides within the bainitic ferrite [Bhadeshia and Waugh, 1982].

In early work on Fe-Ni-C alloys containing relatively high concentrations of nickel, the experimentally measured lengthening rates of bainite were found to be very much *lower* than expected from carbon diffusion-controlled growth [Goodenow *et al.* 1963; Rao and Winchell, 1967]. Consequently it has been suggested that relatively large concentrations of nickel may, via some kind of an interface/solute interaction, retard growth kinetics [Rao and Winchell, 1967, Purdy and Hillert, 1984]. However, since the original work [Goodenow *et al.* 1963, Rao and Winchell, 1967] was published, there have been many refinements to the theory and other aspects concerning the diffusion-controlled growth of plates [Bhadeshia, 1985]. Consequently, the purpose of this work was to reassess the experimental data on bainite growth kinetics in nickel-rich steels in particular, and any other relevant data on alloy steels in general. The early experiments were all based on measurements carried out using light microscopy, a technique which has limited resolution as far as the structure within sheaves of bainite is concerned. They are consequently assumed to refer to the growth rate of sheaves of bainite, rather than to the subunits within the sheaves.

The following chapter is devoted to an attempt at understanding the growth mechanism and the growth rate of Widmanstätten ferrite and bainite. Initially a brief description of the current mechanisms of understanding the formation of both phases is given, the theory of carbon diffusion-controlled growth is then described, and finally, published experimental data on the lengthening rate of sheaves of bainite in alloy steels are analysed and compared with theory.

9.2 Widmanstätten Ferrite

As already stated, Widmanstätten ferrite is an undesirable constituent of a (weld) microstructure because its presence can sometimes lead to poor toughness in low-alloy steels [Savage and Aaronson, 1966, Nakasugi *et al.* 1983]. Widmanstätten ferrite forms as long plates nucleating from previously formed allotriomorphic ferrite layers and growing inwards within the austenite grain structure. Fig. 9.1 shows a typical Widmanstätten ferrite microstructure observed in a Fe-0.4C-2.0Si wt. % alloy. The main characteristic of Widmanstätten ferrite is its long plate-like morphology and the tendency to form in packets of identically orientated plates, thus offering little resistance to cleavage crack propagation.

The formation of Widmanstätten ferrite is also accompanied by a change in the shape of the transformed region. The shape change due to a single wedge of Widmanstätten ferrite has been found to consist of two adjacent and opposing invariant-plane strain (IPS) deformations [Bhadeshia, 1981].

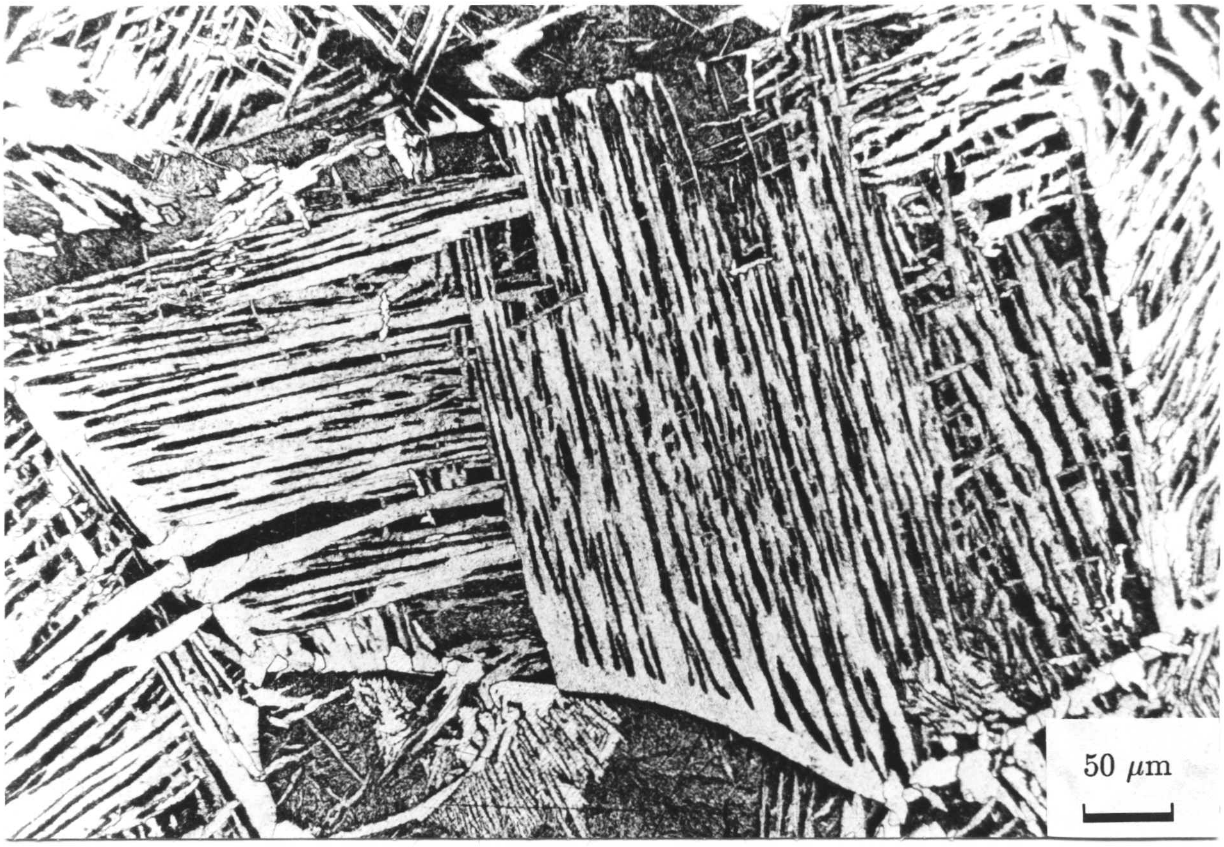

Fig. 9.1: *Optical micrograph showing the Widmanstätten ferrite microstructure in Fe-0.4C-2.0Si wt. % steel, specimen austenitised at 1300 °C for 10* min *and then isothermally transformed at 680 °C for 5* min. *Note the long plates of Widmanstätten ferrite evolved from the grain boundary allotriomorphic ferrite layer, and their parallel formation.*

These IPS deformations each have a large shear component [Watson and McDougall, 1973] and imply the existence of an atomic correspondence between the parent and product phases as far as the iron and substitutional solute atoms are concerned. Interstitial atoms, such as, carbon can diffuse during growth without affecting the shape change or the displacive nature of the transformation. The co-operative growth of a pair of adjacent mutually-accommodating crystallographic variants allows the elastically accommodated strain energy accompanying plate formation to be rather small, of the order of 50 J mol^{-1} [Bhadeshia, 1981]. This is consistent with the temperatures at which Widmanstätten ferrite forms and the wedge morphology which arises because the adjacent variants have slightly different habit planes. The shape change indicates that the $\alpha\ /\gamma$ interface is glissile and the plates can therefore grow at a constant rate controlled by the diffusion of carbon in the austenite ahead of the plate tip. Widmanstätten ferrite cannot be put in the group of diffusional transformation products, because there is no diffusion involved in the actual lattice change; iron and substitutional elements do not diffuse during transformation. There is no reconstructive diffusion [Bhadeshia, 1981] during the formation of Widmanstätten ferrite.

9.3 Bainite

Bainite is a non-lamellar mixture of ferrite and carbides and forms in the temperature range where diffusional transformation gives way to displacive growth. Bainite consists of aggregates of ferrite platelets and residual phases such as martensite, the ferrite being in the form of clusters of thin platelets, commonly called subunits, and the cluster individually being referred to as sheaves of bainite [Aaronson and Wells, 1956].

Sheaves of bainite normally nucleate at austenite grain boundaries (Fig. 9.2) and propagate towards the grain interiors by the "nucleation" and growth of individual subunits [Oblak and Hehemann, 1967]. New subunits nucleate near the tips of previous subunits as shown in Fig. 9.4; the nucleation of subunits in adjacent positions occurs at a much lower rate. This means that the sheaf itself has, on a macroscopic scale, a plate-like morphology in three dimensions. Since coordinated movements of atoms cannot in general be sustained across austenite grain boundaries, and so the growth of a given sheaf is confined strictly to a single austenite grain.

Bainite probably forms by a diffusionless displacive transformation mechanism. The formation of bainite is also accompanied by a change in the transformed region if a polished specimen is allowed to transform to bainite as shown in Fig. 9.4. This shape change is similar to that shown by martensite and Widmanstätten ferrite *i.e.,* an invariant-plane strain (IPS) type.

9.4 Theory of Carbon Diffusion-Controlled Growth

Particle dimensions during diffusion-controlled growth vary parabolically with time when the extent of the diffusion field in the matrix increases with particle size.

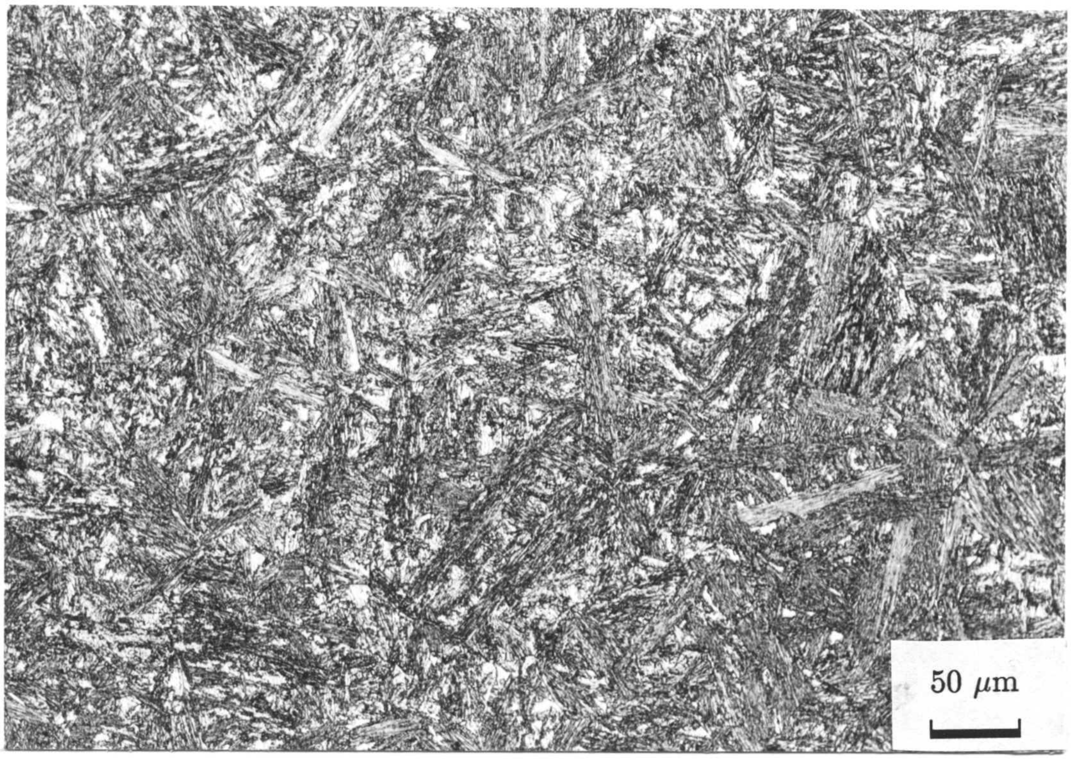

Fig. 9.2: *Optical micrograph showing a bainitic microstructure in a Fe-0.22C-2.05Si-3.07Mn-0.7Mo wt.% alloy. Specimen austenitised at 900 °C for 5* min *and then isothermally transformed for bainite at 400 °C for 1000* s.

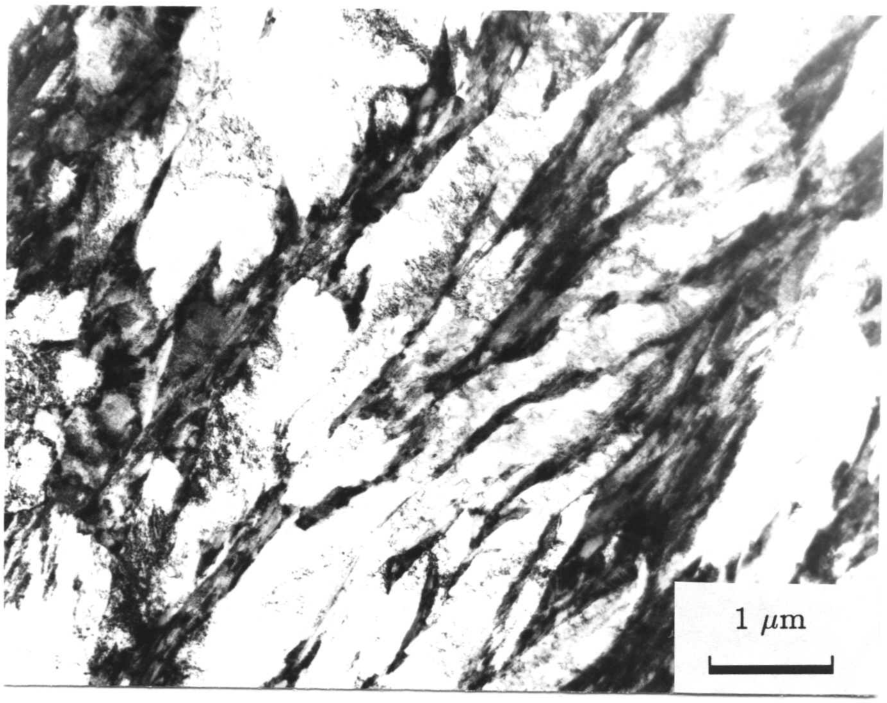

Fig. 9.3: *TEM micrograph showing the sub-unit structure of bainite sheaves in a Fe-0.22C-2.05Si-3.07Mn-0.7Mo wt.% alloy. Specimen austenitised at 900 °C for 5* min *and then isothermally transformed for bainite at 400 °C for 1000* s.

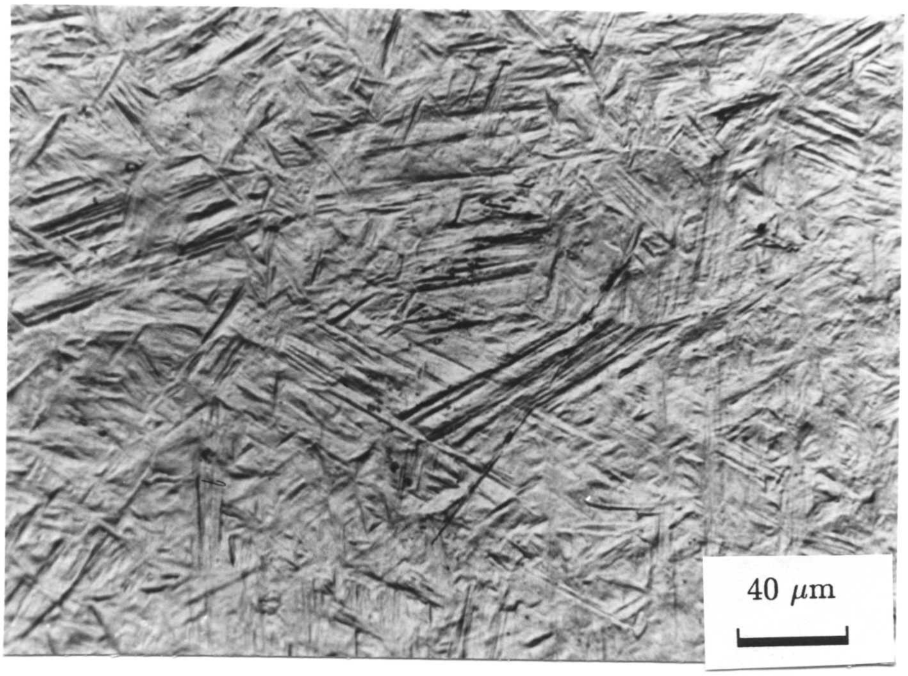

Fig. 9.4: *Surface relief accompanied by the formation of bainite in Fe-0.22C-2.05Si-3.07Mn-0.7Mo wt.% steel. Surface upheavals were imaged by using Nomarski prism. Specimen austenitised at 900* °*C for 10* min *and then isothermally transformed to bainite at 400* °*C for 1000* s.

The growth rate thus decreases with time. On the other hand, Widmanstätten ferrite plates are found experimentally to grow with a constant velocity. It has been demonstrated that Widmanstätten ferrite plates form with equilibrium or paraequilibrium carbon concentration and that the partition of carbon during the growth process is a thermodynamic necessity [Bhadeshia, 1981]. The distribution of carbon during the growth of Widmanstätten ferrite is shown schematically in Fig. 9.5.

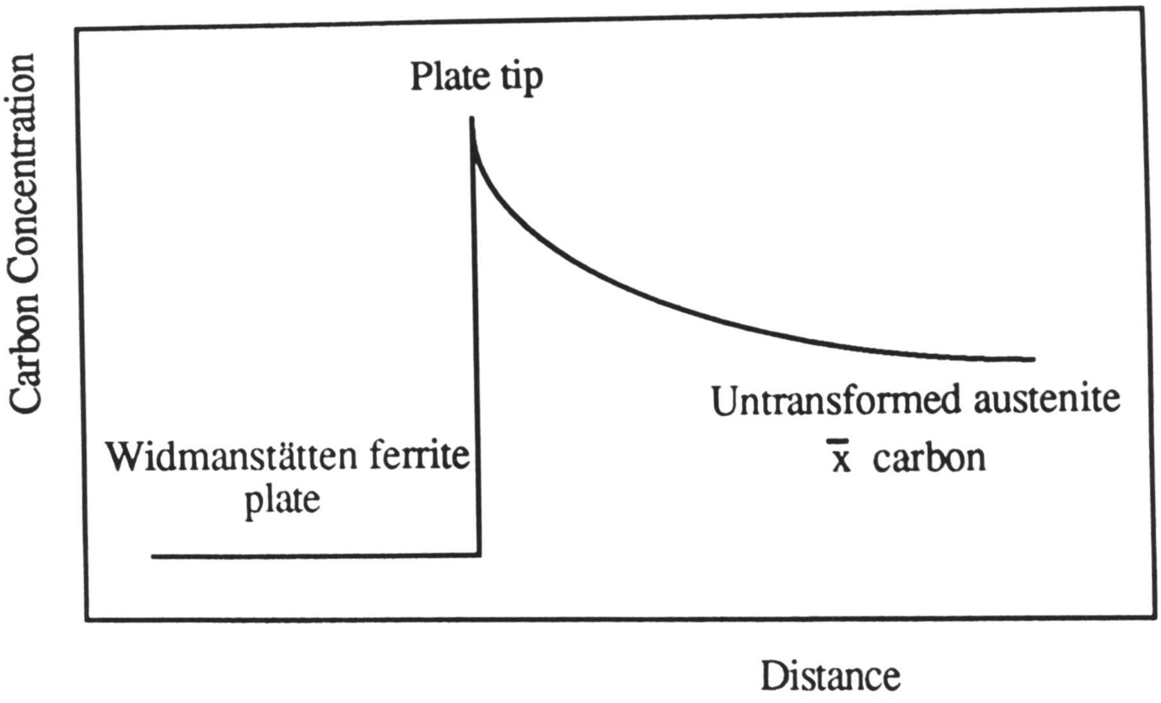

Fig. 9.5: *Schematic representation of the distribution of carbon during the formation of Widmanstätten ferrite plates.*

The diffusion-controlled lengthening of plates or needles can, however occur at a constant rate because solute can be partitioned to the sides of the plates. The shape change accompanying Widmanstätten ferrite growth implies the existence of a glissile α /γ interface and since carbon is partitioned during growth, the rate of growth can be expected to be controlled by the diffusion of carbon in the austenite ahead of the moving interface, even when the reaction occurs at a low homologous temperature. As already stated, iron and substitutional atoms do not diffuse during the growth of Widmanstätten ferrite and bainite and there is no reconstructive diffusion during transformation.

9.5 Theoretical Analysis

Of the various kinetic models available so far, [Zener, 1946; Hillert, 1957; Horvay and Cahn, 1961; Trivedi, 1970] the model proposed by Trivedi [1970] is the most recent one which assesses the relative contributions of diffusion, surface energy and interface kinetic processes during the growth of plate shaped precipitates.

Trivedi [1970] has obtained a solution for the diffusion-controlled growth of parabolic cylinders (an approximation to a plate morphology). The steady state growth velocity v, controlled by the diffusion of carbon in the austenite (γ) ahead of the interface, is obtained by solving the equation:

$$f_1 = (\pi p)^{\frac{1}{2}} exp\{p\} erfc\{p^{\frac{1}{2}}\}[1 + \frac{r_c f_1 S_2\{p\}}{r}] \tag{9.1}$$

where

$$f_1 = \frac{\overline{x} - x^{\gamma\alpha}}{x^{\alpha\gamma} - x^{\gamma\alpha}}$$

In this equation, $\overline{x}$ is the undisturbed carbon concentration in the austenite, well ahead of the plate tip, and can be taken to be equal to the average carbon concentration in the alloy if soft impingement effects are absent. $x^{\gamma\alpha}$ and $x^{\alpha\gamma}$ are the paraequilibrium carbon concentrations in the austenite and ferrite respectively. p is the Péclet number, a dimensionless velocity given by

$$p = \frac{vr}{2\overline{D}} \tag{9.2}$$

where v is the diffusion-controlled growth velocity. The function S_2 has been evaluated numerically by Trivedi [1970]. The diffusion coefficient $D\{x, T\}$ depends on the carbon concentration x, which in turn is a function of the distance ahead of the plate tip, therefore, the diffusivity used in Eq. 9.2 is a weighted average [Trivedi and Pound, 1967]:

$$\overline{D} = \int_{x_r}^{\overline{x}} \frac{D\{x, T\}}{\overline{x} - x_r} dx \tag{9.3}$$

where x_r is the carbon concentration in the austenite at the plate tip, and D is evaluated using the Siller and McLellan model [Bhadeshia, 1982a; Siller and McLellan, 1969; 1970] for the diffusion of carbon in austenite. x_r differs from the paraequilibrium concentration because of the curvature of the interface at the plate tip. It can be calculated using the following equation [Christian, 1975]:

$$x_r = x^{\gamma\alpha}[1 + \frac{\Gamma}{r}] \tag{9.4}$$

where

$$\Gamma = \frac{\sigma V_m (1 - x^{\gamma\alpha})/(x^{\alpha\gamma} - x^{\gamma\alpha})}{RT[1 + \frac{d(ln\{a\})}{d(ln\{x^{\gamma\alpha}\})}]}$$

σ is the interface free energy per unit area, taken to be 0.2 Jm^{-2} [Bhadeshia, 1985], a is the activity coefficient for carbon in austenite, R is the universal gas constant, T is the absolute temperature of transformation and V_m is the molar volume of ferrite [Bhadeshia, 1985]. The paraequilibrium carbon concentration in the austenite (i.e., $x^{\gamma\alpha}$) and the activity coefficient a were calculated using the Lacher-Fowler-Guggenheim quasichemical thermodynamic model [Shiflet *et al.* 1978] and the thermodynamic data given in detail in [Bhadeshia, 1985]. The free energy data for pure iron were obtained from Kaufman *et al.* [1963]. This is believed to make the analysis more reliable for extrapolation to low temperatures [Bhadeshia, 1985]. The paraequilibrium carbon concentration $x^{\alpha\gamma}$ is always so small, that it was estimated using the values for plain carbon steels deduced by Bhadeshia [1982b].

9.5.1 *Extrapolation of the Phase Boundaries*

Both Widmanstätten ferrite and bainite form below the eutectoid temperature and because experimental data for $x^{\alpha\gamma}$ and $x^{\gamma\alpha}$ are not available, therefore α / ($\alpha + \gamma$) and γ / ($\alpha + \gamma$) phase boundaries have to be extrapolated. Finally, because both Widmanstätten ferrite and bainite grow by a displacive transformation mechanism [Bhadeshia and Waugh, 1982], the calculations must take account of the strain energy resulting from the invariant-plane strain shape change accompanying their formation. The stored energy terms for Widmanstätten ferrite and bainite are about 50 and 400 J mol^{-1} respectively [Bhadeshia and Waugh, 1982], and are taken into account according to Bhadeshia [1985]. For illustration purposes, the calculations have been carried out using three different stored energy values of 0, 50 and 400 J mol^{-1}, although only the last set of calculations is strictly relevant for the present work, which deals with bainite.

9.5.2 *Materials*

The chemical compositions of the steels [Hillert, 1960; Goodenow *et al.* 1963; Rao and Winchell, 1967; Oblak and Hehemann, 1967; Speich and Cohen, 1960; Nemoto, 1974; and Simonen et 1973] studied are listed in Table 9.1. The thermodynamic calculations take account of all the elements listed, and an effect on the diffusion coefficient of carbon in austenite is included through their influence on the activity of carbon in austenite [Bhadeshia, 1982a]. Note that some of the steels are not substitutionally alloyed, but were missed in the earlier assessment on Widmanstätten ferrite plates growth [Bhadeshia, 1985] and have been included in the analysis for completeness.

Table 9.1: *Chemical compositions in wt. %.*

Steel	Chemical Composition (wt. %)						Reference
No.	C	Si	Mn	Ni	Mo	Cr	
1	0.25	–	–	1.00	0.0	0.0	Hillert, 1960
2	0.29	0.0	0.0	–	–	–	-ditto-
3	0.36	1.00	–	–	–	–	-ditto-
4	0.46	1.00	–	–	–	–	-ditto-
5	0.49	–	–	–	–	–	-ditto-
6	0.53	–	–	1.00	–	–	-ditto-
7	0.55	1.00	–	–	–	–	-ditto-
8	0.21	0.02	0.26	–	–	–	-ditto-
9	0.35	0.28	0.58	–	–	–	-ditto-
10	0.42	0.08	0.28	—	–	–	-ditto-
11	0.59	0.25	0.56	–	–	–	-ditto-
12	0.81	0.26	0.23	–	–	–	-ditto-
13	0.10	0.18	0.79	8.70	0.07	0.21	Goodenow et al. 1963
14	0.50	0.36	0.68	8.70	–	–	-ditto-
15	0.19	0.29	0.60	8.90	–	–	-ditto-
16	0.29	0.31	0.69	8.80	–	–	-ditto-
17	0.026	–	–	10.6	–	–	Rao and Winchell, 1956
18	0.043	–	–	10.6	–	–	-ditto-
19	0.058	–	–	10.6	–	–	-ditto-
20	0.086	–	–	10.6	–	–	-ditto-
21	0.162	–	–	10.6	–	–	-ditto-
22	0.69	0.70	0.85	1.80	0.81	0.85	Oblak and Hehemann, 1967
23	0.50	0.36	0.68	8.70	–	–	-ditto-
24	0.96	–	–	–	–	–	Speich and Cohen, 1960
25	1.16	–	–	–	–	–	-ditto-
26	1.43	–	–	–	–	–	-ditto-
27	1.14	–	–	–	–	2.70	-ditto-
28	1.12	–	–	5.28	–	–	-ditto-
29	0.51	–	–	9.10	–	–	Nemoto, 1974
30	0.24	0.003	0.002	–	–	–	Simonen et al. 1973
31	0.33	0.002	0.002	–	–	–	-ditto-

9.6 Results and Discussion

The calculated $\gamma/(\alpha+\gamma)$ phase boundaries, representing the variation in $x^{\gamma\alpha}$ as a function of temperature and stored energy, are presented in Fig. 9.6.

9.6.1 *Growth of Widmanstätten Ferrite*

The growth rate of Widmanstätten ferrite plates has been considered in detail by Bhadeshia [1981], and therefore the work presented here is limited to only those data which were missed in the original analysis. The results are presented in Figs. 9.7 and 9.8. Consistent with the original analysis, the measured growth rates are higher (generally an order of magnitude) than those calculated by the carbon-diffusion controlled growth theory, even though the calculations are based on the assumption of the Zener maximum-velocity hypothesis.

9.6.2 *Growth of Bainite Sheaves*

The growth rate calculations of bainite sheaves are presented in Figs. 9.9-9.13, for all the steels listed in Table 9.1, with the exception of steels 24-29. For steels 24-28, the transformation to bainite was carried out under conditions where the diffusivity of carbon in austenite had to be calculated for exceptionally high values of $x^{\gamma\alpha}$. The Siller and McLellan theory for the diffusion coefficient of carbon [Bhadeshia, 1982a; Siller and McLellan, 1969], although known to be highly reliable in both the thermodynamic and kinetic sense, is unable to cope with carbon concentrations in excess of about $\frac{1}{7}$ mole fraction. Consequently, growth calculations could not be carried out for steels 24-28. For steel 29, only one experimental growth rate of 5×10^{-8} m s^{-1} was reported, for a transformation temperature of 380 ^{o}C; the calculated growth rates for stored energy values of 0, 50 and 400 J mol^{-1} are found to be 5.178×10^{-8}, 4.255×10^{-8} and 6.874×10^{-9} m s^{-1} respectively.

For steels 30 and 31, some of the experimental data are found to be slower than calculated. This may be because these are low hardenability steels and therefore some transformation could took place during cooling, which interfere the bainite reaction.